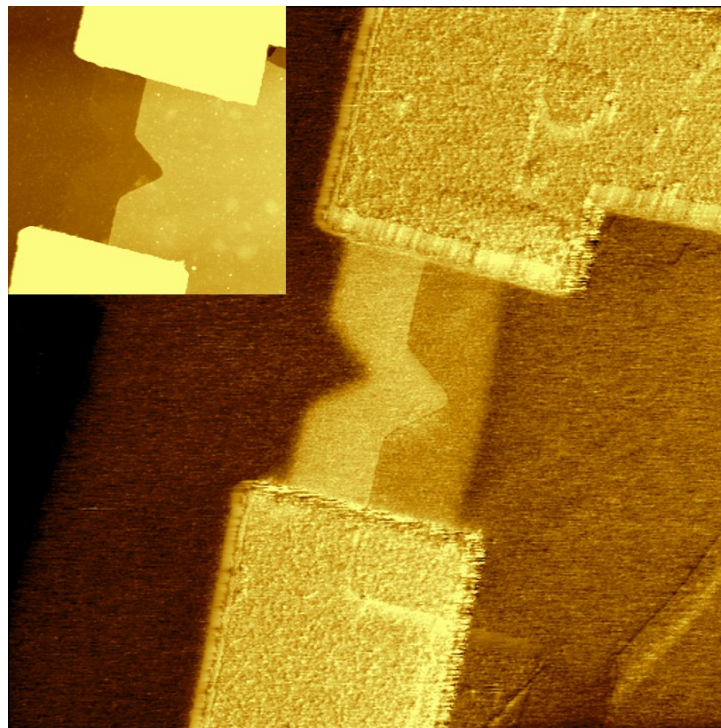

GATE ELECTROSTATICS IN NARROW GRAPHENE DEVICES

Xiaojing Zhao



Supervisor: Professor Peter Bøggild
Co-supervisor: Assistant Professor José Caridad

Department of Micro- and Nanotechnology
Department of Physics
Technical University of Denmark

July 2019

Front page image: The surface potential map of a semi-etched hBN-encapsulated graphene nanoconstriction with the applied external bias, performed by Kelvin Probe Force Microscopy in air ambient. Both the natural and etched graphene edges can be clearly seen. And the electrostatic charge near the edge present to be accumulated. Inset picture is the AFM topography of the device.

Abstract

The discovery of two-dimensional atomic crystals has redefined the nanoelectronics and presents unprecedented potential in the advancement of information technology. Graphene, as the first isolated two-dimensional material, holds enormous potential nanoelectronic applications due to its unique electronic band structure and high carrier velocity. Graphene-based field effect transistors have been widely used to investigate the electron transport in graphene. Due to the 2D geometry of graphene, the distribution of electrostatic charge in narrow graphene devices is not be homogeneous. Moreover, a charge accumulation caused by the electrostatic fringe field effect takes place at the graphene edges. Interplay between the gate, the dielectric environment and the graphene electronic system is complex, and gate electrostatics have turned out to be essential for the performance of graphene devices.

Kelvin Probe Force Microscopy (KPFM) has with its ability to locally probe the potential difference, providing a superior spatial resolution, been an excellent tool for mapping the electrostatics in graphene as well as identification of graphene layers. In this project, KPFM has been used for studying the charge distribution in narrow graphene devices by mapping the electrostatic potential variations with an application of the external gate bias.

The experimental preparation and fabrication of the graphene devices have been demonstrated. Two different graphene devices are fabricated for the study of gate electrostatics. One is the hydrophobic HMDS supported open graphene nanoconstriction, the other is the semi-etched hBN-encapsulated graphene nanoconstriction. Specially, a modified hot Pick-up technique is developed for thin hBN/graphene/hBN heterostructure (total thickness ≤ 25 nm) assembly. With the application of an external gate bias, KPFM measurements in different environments have been performed to display the electrostatic potential distribution of both graphene devices. A pronounced charge accumulation is observed at the graphene edges. Furthermore, such charge accumulation in narrow graphene devices is significantly dependent on the device dimensions, edge disorder as well as the measuring environment.

Moreover, a Raman study with a focus on the graphene-bubbles' location in van der Waals heterostructures has been demonstrated. The local strain and doping of the graphene bubbles have been discussed from the Raman maps. It is noted that doping is dominated when the bubble is trapped below graphene, while, surprisingly, tensile strain is dominated in the graphene when the bubble is located above graphene.

Resumé

Opdagelsen af to-dimensionelle krystaller har omdefineret nanoelektronik og muliggjort en hidtil uset nyudvikling i informationsteknologi. Grafen er det to-dimensionelle materiale som først blev isoleret. Det har et enormt potentiale indenfor nanoelektronik på grund af dens unikke elektroniske båndstruktur og høje ledningsbærerhastigheder. Grafenbaseret felleffektstransistorer er typisk blevet brugt til at studere de elektriske egenskaber af grafen. Siden at grafen er to-dimensionelt, er elektrostatisk ladning i smalle stykker grafen ikke homogent fordelt. Ydermere gør elektrostatiske kantfeltseffekter, at ladning bliver akkumuleret langs kanterne af grafen. Samspillet mellem gaten, det dieletriske miljø og det elektriske system i grafene er komplekst, og det er blevet påvist at gate-elektrostatik er afgørende for grafenkomponenters ydeevne.

Klewin Probe Kraftsmikroskopi (KPKM) har med sin evne til at måle elektrisk potentialforskelle lokalt, med en høj rumlig opløsning, vist sig at være et fremragende værktøj til at kortlægge elektrostatik i grafen, samt at identificere antal lag af grafen. I dette projekt er KPKM blevet brugt til at undersøge ladningsfordelingen i smalle grafenkomponenter ved at kortlægge elektrostatiske potentialforskelle.

Først er to forskellige grafenkomponenter blevet fabrikeret: en hydrofobisk HMDS-støttet åben nanokonstriktion, samt en hBN indkapsuleret nanokonstriktion. En modificeret "varm pick-up" teknik er udviklet for at samle tynde hBN/grafen/hBN heterostrukturer med en total tykkelse på mindre end 25 nm. KPKM-målinger foretaget i forskellige miljøer med en ekstern gate-bias, er udført for at kortlægge fordelingen af det elektrostatiske potentiale i begge typer grafenkomponenter. En tydelig ladningsbærer akkumulering blev observeret ved grafenkanten af disse komponenter. Denne ladningsbærer akkumulering er ydermere meget afhængig af komponentgeometrien, kantuorden samt miljøet målingen er foretaget i. Desuden er et Raman-studie med fokus på luftboblers placering i van der Waals heterostrukturer præsenteret. Den lokale tøjning og dotering af grafen ved bobler bliver diskuteret med udgangspunkt i Ramanmålingerne. Det bemærkes at doteringen dominerer når boblen er fanget under grafenen, mens at tensil tøjning dominerer når boblen er over grafenen.

Preface

The dissertation has been carried out at the Department of Micro- and Nanotechnology and Department of Physics at the Technical University of Denmark in the period from April 2016 to April 2019. The project received funding from the Independent Research Fund Denmark. The device fabrication was contributed to the accessible facilities of cleanroom at DTU Danchip.

This project was supervised by Professor Peter Bøggild and was co-supervised by Assistant Professor José Caridad. An external stay of November of 2018 and January of 2019 was conducted at the National Physical Laboratory in London, and generously sponsored by the Horizon 2020 Graphene Flagship CORE 2 project.

Acknowledgements

First of all, I would like to offer up my most genuine and massive thanks to my supervisor, Peter Bøggild, who has always been patiently tutoring and supporting me during the Ph.D project. Without your guidance and help, I would not accomplish this job. It is also you make me become more and more confident about myself. Sincerely thank you for the trust and faith in me.

I would like to give a huge thanks to my co-supervisor José Caridad. Thank you for all your kind help. I want to give tons of thanks to my dear group colleagues: Tim Booth, thanks for the professional advices and lovely help on KPFM. Lene Gammelgaard, without you, I would not have made such glorious devices, and also without you, I would not be such good both at work and personally. Bjarke Jessen, thank you for always being nice and patient when I every time ask for help about the science. Aske Nørskov Gejl and Joachim Dahl Thomsen, thank you for being such kind officemates, without you both, life would be much less enjoyable. And my first co-authored paper was attributed to Patrick Rebsdorf Whelan, it was a delightful collaboration. Thanks David Mackenzie, Abhay Shivayogimath, Xin Chen, and Sarah Wernblad Anker for being such nice during my Ph.D. It is the best group I could have ever asked for, working with you all has been the most beautiful moment in my life. You all are much more than colleagues to me. Thanks to Jie Ji and Sanshui Xiao for the kind help on simulation work performed in this thesis using COMSOL. And a specially and greatly thanks to Peter, Joachim, Abhay, Patrick and Shuangyue Yang for help proofreading this thesis.

I also would like to thank a few staffs at DTU Danchip including Lean Gottlieb Pedersen, Conny Hjort and Peixiong Shi. Thank you all for being so nice whenever I ask for help in the cleanroom.

I want to give a big thanks to Professor Olga Kazakova, thank you for giving me the chance to be one member of your group. It was such a pleasure to work with you and others. Specially, I would express my appreciation to Christos Melios, Eli Castañón García-rovés, Héctor Corte León and Tom Vincent. I am very grateful for your help and time on performing the KPFM measurements of my devices, without you, I would not have the achievements presented in the thesis.

I would like to mention my friends and family-like roommates. My lovely bartender crews: Nastasia, Tanja, Lukas and Chen. My Friends: Johanna, Daena, Astrid, Susanne, Anne, Gaetano, Nicolas, Andrea.... wish I could write all my friends' name down here... thank you all have made the PhD enjoyable. I also want to thank my friends from the dormitory: Helene, Joachim, Kristian, Jesper, Tobias, Laura, Andreas, Victor and Daniel, thank you all for loving and caring me like a family since I moved in, thank you for all the beautiful memories in køkken23.

Last but not the least, my beloved parents, brothers, sister-in-law and my adorable nephew, I surely would not have made any of the achievements without your support. Especially my parents, have been showing so much love and great concerns to me since my very first day in Denmark! Thank you for bringing me to the world and always telling me: Have courage and Be kind.

Xiaojing Zhao

Technical University of Denmark, B:345B, R:256.

July 2019

Acronyms

0D	zero-dimensional
1D	one-dimensional
2D	two-dimensional
AFM	atomic force microscopy
AM	amplitude modulation
Ar	argon
Au	gold
C-AFM	conductive atomic force microscopy
Cr	chromium
DTU	Technical University of Denmark
DOS	density of states
EBL	electron beam lithography
FM	frequency modulation
FWHM	full width at half maximum
hBN	hexagonal Boron Nitride
HMDS	hexamethyldisilazane
IPA	isopropyl alcohol
KPFM	Kelvin probe force microscopy
AM-KPFM	Amplitude modulation Kelvin probe force microscopy
FM-KPFM	Frequency modulation Kelvin probe force microscopy
l_{mfp}	mean free path
OM	optical microscopy
-OH	hydroxyl groups
PA	plasma asher
PDMS	polydimethylsiloxane
PMMA	polymethylmethacrylate
PPC	polypropylenecarbonate

PSPD	position-sensitive photo diode
Si	silicon
SiOH	silanol groups
SiO₂	silicon dioxide
Ti	titanium
vdW	van der Waals

Contents

Abstract	ii
Resumé	iv
Preface	vi
Acknowledgements	vi
Acronyms	viii
Contents	x
1 Introduction	1
1.1 Background and Motivation	1
1.2 Thesis Outline	3
2 Graphene: Physics and Devices	5
2.1 What is Graphene?	5
2.2 The Structure of Graphene	6
2.3 Gate Electrostatics in Graphene-based Devices	9
2.3.1 Analytical Calculation of the Planar Charge Density	9
2.4 Bubbles in the Van der Waals heterostructure	14
3 Characterization Techniques	15
3.1 Optical Microscopy	15
3.2 Raman Spectroscopy	17
3.2.1 Raman Spectrum of Graphene	18
3.2.2 Confocal Raman Microscopy	20
3.3 Atomic Force Microscopy (AFM)	20
3.4 Kelvin Probe Force Microscopy (KPFM)	23
3.4.1 Working Principle of Kelvin probe force microscopy (KPFM)	23
3.4.2 Amplitude Modulation Kelvin probe force microscopy (AM-KPFM)	24
3.4.3 Frequency Modulation Kelvin probe force microscopy (FM-KPFM)	26
4 Sample Preparation and Fabrication	29
4.1 Substrate Preparation	29
4.2 Isolation and Identification of Graphene and hBN	31
4.2.1 Exfoliations and Transfer on Different Substrates	31
4.2.2 Identification of Graphene and hBN	33
4.3 Van der Waals (vdW) Heterostructure Assembly	34
4.3.1 Preparation Work Before the Assembly	34
4.3.2 Standard Hot Pick-up Technique for hBN/graphene/hBN Stack	36
4.3.3 Modified Hot Pick-up Technique for Thin hBN/graphene/hBN Stacks	40
4.4 Device Fabrication	42
4.4.1 Electron Beam Lithography	42

4.4.2	Device Fabrication Process Flow	42
5	Gate Electrostatics in Graphene Nanoconstrictions.....	49
5.1	Electrostatic Potential Measurements in Gated Graphene Devices.....	49
5.2	Gate Electrostatics in HMDS-supported Open Graphene Nanoconstrictions.....	51
5.2.1	Experimental setup.....	51
5.2.2	Results and Discussion.....	52
5.2.3	Concluding Remarks	60
5.3	Charge Distribution in Semi-etched Encapsulated Graphene Nanoconstrictions	61
5.3.1	Sample Preparation and Experimental Setups.....	61
5.3.2	KPFM Results and Discussion	63
5.3.3	Concluding Remarks	78
5.4	Summary.....	78
6	Raman Characterisation of Bubbles in Van der Waals (VdW) Heterostructure.....	81
6.1	Bubble Configuration in The VdW Heterostructure Assembly	81
6.2	The Fitting Model Used for Raman Measurements.....	83
6.3	Results and Discussion.....	85
6.4	Concluding Remarks	93
7	Thesis summary	95
7.1	Conclusions.....	95
7.2	Outlook.....	96
	Appendix A.....	97
	Appendix B.....	99
	Appendix C	101
	Bibliography	103

1 Introduction

1	Introduction	1
1.1	Background and Motivation	1
1.2	Thesis Outline	3

1.1 Background and Motivation

Two-dimensional (2D) materials are a rising family of nanomaterials that are comprised of one or more atomically thin layers. These materials have the potential to revolutionize the future of the electronics industry due to their unusual and sometimes exceptional properties. For this reason, the research of 2D materials has been accelerated rapidly over the last decade. The first isolated 2D material was graphene in 2004[1], hundreds of different layered materials have been studied experimentally and theoretically since graphene's discovery.

Graphene consists of one layer of carbon atoms arranged in a honeycomb lattice with sp^2 bonds. The in-plane σ -bonds give rise to graphene's outstanding mechanical and structural properties, such as high rigidity combined with high flexibility[2], high temperature stability[3], the remarkable chemical inertness[4]. The out-of-plane π -bonds are responsible for graphene's outstanding electronic properties, such as its predicted giant intrinsic carrier mobility of $200,000 \text{ cm}^2\text{V}^{-1}\text{s}^{-1}$ [5]. Therefore, graphene is both a platform for studying solid state physics and materials science and has considerable commercial potential.

Field effect devices based on graphene are important because they allow for the tuning and studying of the electronic properties of graphene and are used in many types of commercial electronics. Of particular interest are graphene nanoscale devices, especially in the context of the extreme demands for miniaturization, since dimensional scaling is approaching the limits for conventional silicon-based electronics. The atomic thickness and the compelling electronic features of graphene make it a promising candidate for post-silicon electronics[6], [7]. The development of graphene transistors has seen considerable progress since the first top-gated graphene FETs were reported in 2007[8]. Yet, the gate electrostatics in gated graphene devices is complicated and have not been fully explicated[9]–[12]. Since graphene situated on a dielectric can act as a capacitor, a quantum mechanical effect arising from the low density of the states (DOS), which originates from the Pauli Exclusion Principle has to be taken into account. This is distinct from the classic regime where the planar distribution of externally injected charges is determined by the dimensions and employed dielectric medium of the devices. With the application of external electric field, the atomic thin plane is not able to accommodate the

gate-induced extra carriers for such a low dimensional system, but the edges provide possibilities. With a given hard-wall confinement at the graphene edges, a remarkable charge accumulation attributed to the electrostatic fringe field effects takes place under gating[9]–[13]. The electronic band structure of graphene is moderately modified because of its inhomogeneous charge distribution; it is necessary to study the gate electrostatics since this will be significant for a deeper understanding of the electronic transport in graphene-based field effect devices as well as other 2D materials.

Fernández-Rossier et al.[9] studied the modified electronic structure of gated graphene nanoribbons and proposed that the “contribution” was induced from the quantum mechanical effects in the gate electrostatics. In particular, they computed the quantum contribution using the Hartree approximation, which demonstrated that both the charge density distribution and electrostatic potential at the graphene nanoribbon surface were position-dependent. Shylau et al.[11] further showed self-consistent numerical calculations for the quantum contribution in graphene strip capacitors. In their study, they found that their exact calculations were qualitatively in agreement with the analytical theory and implied that the quantitative discrepancies were associated with the Coulomb interactions of the injected carriers. Using the semiclassical approach, Silvestrov and Efetov[10] investigated microscopic charge accumulation along the boundaries of graphene strip. They provided a numerical description of the in-plane charge density profile, which develops with a $1/\sqrt{x}$ edge singularity in graphene devices. A dependence on strip size was also discussed in the study. It should be noted that the striking charge accumulation at the edges of graphene strips plays a key role in transport in quantum Hall regime, since it creates an effective contribution to the enhanced conductance[12]–[17]. Wang et al. [18] numerically calculated the charge distribution on a conducting rectangular graphene sheet by treating each carbon atom as a polarized sphere with a net charge and an induced dipole. Based on their results, it appears that the charge enhancement at the corner of a graphene sheet can be up to 14 times higher than the charge density at the center.

The role of charge accumulation has also been mentioned and briefly discussed in some electron transport studies[12], [15], [16], [19] with respect to the realistic graphene devices; however, this has not been explicitly investigated and specifically addressed in experiments. The straightforward reason is that it is difficult to find an operational way of capturing the position-dependent charge density across the graphene channel meanwhile applying gate bias on the device. It is noteworthy that neither the classical electric interaction nor the quantum contribution is directly accessible in experiments. Therefore, a relation between the two parts must be addressed so that the quantum contribution is available to be extracted from the total electrostatics. On the other hand, such a relation is usually solved based on idealized analytical models and other effects, such as edge disorders, impurities or the interplay between substrates and graphene, are often neglected. Apart from a dependence on the in-plane position, the charge density profile at a graphene surface is also sensitive to the channel width, device geometry, edge morphology, applied dielectrics and the external electric field[9]–[11], [13], [20]–[22]. It is impossible to avoid inducing edge disorders as well as the surficial impurities during the device fabrication process. In order to provide physical insight into the gate electrostatics

of graphene-based field effect devices, it is important to intuitively illustrate the charge accumulation in realistic graphene samples, which we explore through experimentation. To this end, rather than inspecting the charge density directly, the local potential profile is investigated as a departure for an improved understanding of the gate electrostatics of graphene-based field effect devices.

Graphene bubbles in van der Waals heterostructures are commonly seen during the assembly process. We accidentally observed that the surface potential of the graphene bubbles in hBN/graphene/hBN heterostructure presents inhomogeneous, and such surface potential distribution of the bubble area slightly changed when a gate voltage was applied. A Raman check on the graphene bubbles implies a possible relation of the bubbles' location. It is therefore a Raman study on the graphene bubbles with respect to its location has been carried out in this thesis. It is known that graphene bubbles have attracted an intense attention since the bubble-induced strains can be used to tune the electronic, optical and magnetic properties of graphene simply from the strain engineering[23]–[28]. The presence of graphene bubbles also demonstrates potential applications such as gas/ion storage[24], [29], [30], observable confined cavity for chemical reaction[31], [32] and liquid cells for revealing the nanocrystal growth[33], [34]. However, there are few studies related to the investigation on the location.

Based on the results from the two studies, two paper works are in preparation. A published work which I am co-authored can be found from literature[35].

1.2 Thesis Outline

Based on the motivation presented in the introduction, the current study of gate electrostatics in narrow graphene devices is organized and developed as follows:

Chapter 2

In this chapter, the basic electronic structure of graphene is presented. The analytical calculation with respect to the in-plane charge density distribution and the local potential across the gated graphene strip is demonstrated. The role of graphene bubble in the van der Waals heterostructures is been briefly discussed.

Chapter 3

A few standard characterization techniques used in this work are introduced in this chapter: optical microscopy (OM), Raman spectroscopy, atomic force microscopy (AFM), conductive atomic force microscopy (C-AFM), and Kelvin probe force microscopy (KPFM).

Chapter 4

In this chapter, the sample preparation and device fabrication methods are presented in detail. All the involved 2D materials are achieved from the mechanical cleavage technique. Therefore, the details of the mechanical isolation procedure are demonstrated. The preparation of the HMDS-rendered SiO₂/Si substrate is described, and the standard “hot pick-up” technique for assembling the hBN and graphene is also presented. In particular,

a special “hot pick-up” technique is described for thin hBN/graphene/hBN heterostructures of a total thickness below 25 nm. Finally, the device fabrication process flow of two different devices, including the employed machines and parameters, is presented.

Chapter 5

This chapter contains the results and discussions of the study of electrostatic charge distribution in two different types of graphene nanoconstriction devices. The KPFM measurements of the HMDS supported open graphene nanoconstrictions are first presented and discussed. The gate electrostatics of the hBN-encapsulated graphene nanoconstriction device are discussed in detail.

Chapter 6

Graphene bubbles can be created both below and above graphene in the graphene heterostructures. Hence, a Raman study addressing the strain distribution and doping of graphene bubbles with respect to the bubble’s location is presented in this chapter.

Chapter 7

Thesis summary and an outlook are given in the last chapter.

2 Graphene: Physics and Devices

2.1 What is Graphene?.....	5
2.2 The Structure of Graphene.....	6
2.3 Gate Electrostatics in Graphene-based Devices.....	9
2.3.1 Analytical Calculation of the Planar Charge Density.....	9
2.4 Bubbles in the Van der Waals heterostructure.....	14

The revolution of engineering materials has played an important role in the advancement of human society, as implied by the stone age, bronze age, iron age, steel age (industrial revolution), and the current silicon age[36]. The importance of silicon-based electronics in the development of information technology over the last half-century cannot be overstated, but the era may soon come to an end since the feature size of semiconducting silicon chips is approaching their physical limit[37], [38]. Therefore, 2D materials, such as graphene, are possible candidates for supporting beyond-Moore electronics and devices. Graphene was first isolated by A. K. Geim and K. Novoselov[1], who received the Nobel Prize in physics in 2010. The extraordinary properties of graphene have triggered intense research in fundamental properties as well as applications within areas, such as energy, electronics, photonics, sensors, materials, and many more. Graphene[39] catalyze the beginning of a new era where 2D materials play a key role.

2.1 What is Graphene?

Graphene was theorized for over 60 years [39], [40] before it was experimentally isolated and studied in a laboratory[41]. Simply put, graphene is a sheet of pure carbon atoms peeled from graphite. Imaging of the bulk graphite with scanning electron microscopy reveals that graphite consists of thin layers, see **Figure 2.1**. These layers can be further cleaved by peeling them apart simply using scotch tape. After this process is repeated a few times, the single-atom-thick layer of graphene can be isolated. Graphene consists of covalently bonded carbon atoms arranged in a hexagonal lattice representing a stable free-standing state. Graphene can be considered one of the basic building blocks of all graphitic materials of other dimensionalities, such as 0D fullerenes, 1D nanotubes, and 3D graphite.

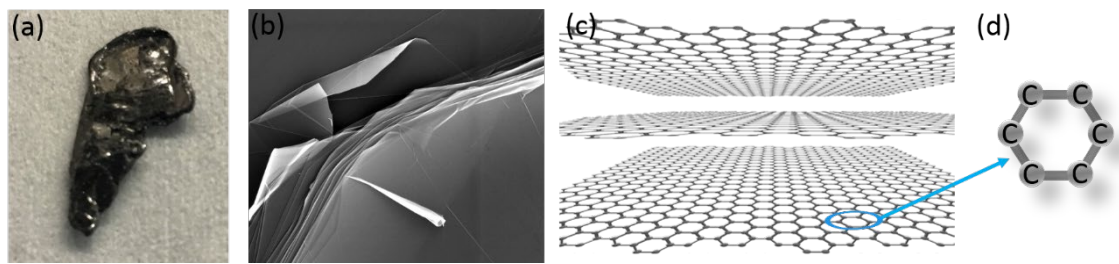


Figure 2.1 A schematic representation of creating graphene from graphite. (a) Bulk graphite; (b) SEM images of graphite with a layering feature, adapted from <http://sem.elte.hu/generic/img/galleries/bemutato/15-HOPG.jpg>; (c) a visual depiction of the layered structure, adapted from <https://www.gratispng.com/png-fnmx0d/>; (d) the honeycomb lattice in graphene.

Even though graphene is a mere one atom thick, its in-plane Young's modulus is about 1 TPa, and its fracture strength is approximately 130 GPa[42], giving graphene relatively high rigidity and mechanical strength. It is, however, its the electronic properties that have attracted most attention. In a semiconductor, an energy bandgap separates the valence and conduction bands, both of which have a parabolic relationship between energy, E , and wavenumber, k . Graphene is different, in that its carriers are described by the Dirac equation, which leads to linear energy bands that meet in six discrete Dirac points, causing graphene to be a zero-gap semiconductor. Graphene's unique electronic properties, such as its giant intrinsic carrier mobility[5], [43] and ballistic electron conductance[44], [45] are consequences of its particular band structure, making graphene an extremely attractive electronic material.

2.2 The Structure of Graphene

Each carbon atom has four valence electrons, distributed in the 2s and 2p orbitals. In graphene, structural stability is provided to the tightly bonded carbon atoms via in-plane σ -bonds, formed from the sp^2 hybridization of p_x , p_y and s orbitals. The remaining electron orbitals, p_z , merge into a large molecular orbital, forming π -bonds between the atoms (**Figure 2.2 (a)** and **(b)**); if one imagines the graphene as a planar atomic-scale chicken wire, the π -bonds located above and below in each cycle form a delocalised orbital cloud, see **Figure 2.2 (a)**. This allows the electrons in the π -bonds to jump from atom to atom, and thereby carry an electric current. These π -bonds are responsible for most of the peculiar low-energy electronic properties of graphene[46], [47].

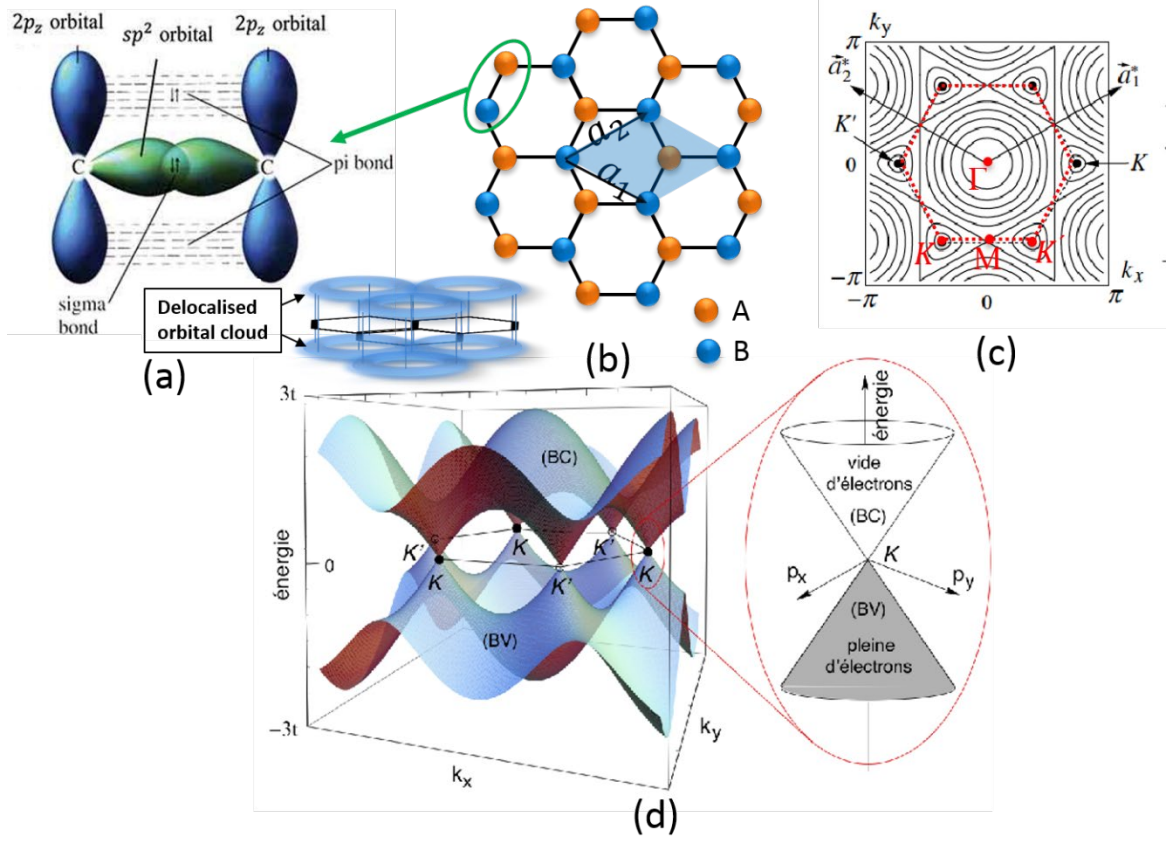


Figure 2.2 (a) In-plane σ bonds and out-of-plane π -bonds formed by sp^2 hybridization, adapted from [48]. (b) The crystal lattice of graphene, \mathbf{a}_1 and \mathbf{a}_2 are vectors with the blue region showing the unit cell. (c) The band structure with displayed equal energy contours. The reciprocal Bravais lattice is also triangular and the first Brillouin zone (BZ) is hexagonal, as illustrated by the red dashed line. K and K' are the inequivalent corners of BZ, corresponding to the energy spectrum in (d), adapted from [49]; (d) Tight-binding band structure of graphene, adapted from [50], where the zoomed region displays a linear dispersion relation at the Dirac point.

Graphene consists of one layer of carbon atoms arranged in a planar 2D honeycomb lattice structure, as illustrated in **Figure 2.2 (b)**. The structure can be regarded as two intermingling triangular Bravais lattices with a basis of two atoms, A and B, in the unit cell (the blue region). The lattice vectors can be described as:

Eq (2.1)

$$\mathbf{a}_1 = \frac{a}{2}(3, \sqrt{3}), \quad \mathbf{a}_2 = \frac{a}{2}(3, -\sqrt{3}),$$

where $a = 1.42 \text{ \AA}$ and denotes the carbon-carbon bond length. The reciprocal lattice vectors, as illustrated in Figure 2.2 (c), are given as:

Eq (2.2)

$$\mathbf{a}_1^* = \frac{2\pi}{3a}(1, \sqrt{3}), \quad \mathbf{a}_2^* = \frac{2\pi}{3a}(1, -\sqrt{3}),$$

which define the corresponding Brillouin zones (BZs). The six vertices of the first BZ, as displayed in Figure 2.2 (c), are of particular interest when considering the physics of graphene. These are known as the Dirac points and are comprised of three pairs of inequivalent points, K and K' . In momentum space, their positions are given by:

Eq (2.3)

$$\mathbf{K} = \left(\frac{2\pi}{3a}, \frac{2\pi}{3\sqrt{3}a} \right), \quad \mathbf{K}' = \left(\frac{2\pi}{3a}, -\frac{2\pi}{3\sqrt{3}a} \right),$$

Using the simple tight-binding approximation, the electronic band structure of graphene can be calculated. Considering only the nearest-neighbor hopping energy for electrons, the tight-binding Hamiltonian equation for graphene is:

Eq (2.4)

$$\hat{H} = \hbar v_F \hat{\sigma} \cdot \mathbf{q}$$

Here, \hbar is the reduced Plank constant, $v_F \approx 10^6$ m/s is the Fermi velocity, and $\hat{\sigma}$ are the usual Pauli matrices[51]. Explicitly, **Eq (2.4)** is a 2D Dirac Hamiltonian[52], exactly that of a massless particle of spin 1/2[53], [54], with an effective “speed of light” given by the Fermi velocity.

The energy bands derived from the Hamiltonian are obtained as follows:

Eq (2.5)

$$E(k_x, k_y) = \pm t \left(1 + 4 \cos \frac{3k_x a}{2} \cos \sqrt{3} \frac{k_y a}{2} + 4 \cos^2 \frac{\sqrt{3}}{2} k_y a \right)^{1/2}$$

Where $t \approx 2.8$ eV [46] is the nearest neighbor hopping energy, and the signs denote the upper (conduction) and lower (valence) bands, with the lattice constant $a=2.46$ Å. The two bands touch at the Dirac points, creating a gapless band spectrum, as shown in **Figure 2.2 (d)**.

The low-energy band structure in the vicinity of Dirac points (K and K') fulfils:

Eq (2.6)

$$E(k) = \pm \hbar v_F \sqrt{k_x^2 + k_y^2}$$

Where $\sqrt{k_x^2 + k_y^2}$ is the magnitude of the wavevector k , and the + /- signs denote the conduction and valence bands respectively, see **Figure 2.2 (d)**.

As a consequence, the density of states (DOS) for graphene is linear in energy:

Eq (2.7)

$$N(E) = \frac{2|E|}{\pi(\hbar v_F)^2}$$

Explicitly, the DOS vanishes at the Dirac point where the energy is zero. Due to the low DOS, the carrier concentrations in graphene can easily be controlled electrostatically, by inducing a non-zero charge distribution nearby (in the substrate or above)[55]–[60], applying an electric field[1], [6], [10], [18], [46], [51], [61]–[65], or introducing disorders in the lattice[46], [66]–[68]. Thus graphene can be used for different applications by tailoring its electronic properties[40], [47], [69], [70].

2.3 Gate Electrostatics in Graphene-based Devices

2.3.1 Analytical Calculation of the Planar Charge Density

In 1990, Nishiyama et al.[71], studied the surface density charge distribution of a long rectangular plate capacitor. Their study demonstrated the relation between the charge density and the strip capacitance via the boundary element method. It turns out that the fringe field effects cannot be neglected unless the aspect ratio (b/a) of the gap, b , and the capacitor width, a , is very small ($\frac{b}{a} < 0.01$), and a tremendous charge accumulation occurs near the edges of the strip capacitor with the induced charges. Description of the electron transport in graphene is strikingly different from those of conventional semiconductor-based two-dimensional electronic systems[9], [72], [73]. In the case of graphene-based field effect devices, where usually a graphene sheet separated from a metallic gate (i.e. a highly doped Si) by a relatively thick dielectric (i.e. SiO₂ of a typical width of 300 nm), It has recently shown that a pronounced charge accumulation takes place at the edges of the finite-size graphene channel due to the electrostatic fringe field effects[10]. More specifically, due to the small DOS in graphene, the in-plane charge density as well as the electrostatic potential is not monotonic but varies as a function of the position. For this reason, the gate electrostatics in graphene devices can be complicated considering a concurrence of classical electrostatic interaction and quantum mechanical effects. Although the quantum contribution has been addressed in different analytical models and the electrostatically-induced charge density has been numerically calculated in the case of 2D graphene strips, there are few studies of realistic graphene samples in literature with respect to these aspects. Visualisation of the distribution of the electrostatically-induced charges is necessary to compare the spatial charge distribution with theoretical models, and ultimately understand electronic transport in gated graphene devices.

To this end, in this section, we first consider the operability of realistic graphene samples by exploring the relation between the inhomogeneous charge density and the local potential across the graphene channel.

The Thomas-Fermi (TF) approximation is often used to address the charge response to the externally applied electric field. This is because this semiclassical model provides an explicit and simple functional form between the electronic energy and the local charge density, $n(r)$. Given a system at a finite temperature, the total energy is as follows:

Eq (2.8)

$$E[n(r)] = \int T[n(r)]dr + \int n(r)V(r) dr$$

Where the first term is the kinetic energy and the second term is the classical electrostatic potential. A case of a pristine graphene strip with a finite width of a situated on an insulating barrier of SiO_2 with a depth of b is considered. As introduced in [Section 2.2](#), the dispersion relation of electron near the Dirac point is given by $E = \pm \hbar v_F k_F$, where the Fermi wave vector, k_F , depends on the carrier density: $k_F = \sqrt{\frac{4\pi n}{g_s g_v}}$ [73]. Letting $\sqrt{g_s g_v} = 2$ for the case of monolayer graphene one can obtain the TF kinetic energy functional equation for the case of Dirac fermions:

Eq (2.9)

$$T[n(r)] = \hbar v_F \frac{2\sqrt{\pi}}{3} |n(r)|^{3/2} \text{sgn}[n(r)]$$

In a semiclassical approximation, the relation between the electrostatic potential, $V(r)$ and the local density, $n(r)$, can be obtained by solving the minimization of the total energy, $E[n(r)]$, by taking the functional derivative with respect to the density $n(r)$. Thus, a Lagrange multiplier, μ , is introduced, identified as the equilibrium chemical potential of the system (or equivalently, the Fermi energy, E_F). Substituting **Eq (2.9)** into **Eq (2.8)**, using the condition $\frac{\delta E}{\delta n} = 0$ yields the local density functional form:

Eq (2.10)

$$n(r) = \frac{1}{\hbar^2 v_F^2 \pi} (\mu - V(r))^2 \text{sgn}(\mu - V(r))$$

Which relates the electron density, $n(r)$, to the self-consistent potential, $V(r)$. Since the TF approximation is a cruelly simplified model, the case of relevance in the analytical model requires that the local potential varies weakly on the scale of the Fermi wavelength: $\frac{|\Delta V(r)|}{|V(r)k_F(r)|} \ll 1$, so that the approximation is permissible. In the **Eq (2.10)**, $V(r)$ is a sum of the external potential and the Hartree term, which can be approximately obtained from the TF approximation by solving the Poisson's equation using a finite element solver. It can also be numerically calculated in Hartree approximation based on tight-binding Hamiltonian[11], [74], [75]. Here it is worth mentioning that the TF approximation has been proved to correspond well with the quantum mechanical models with respect to the calculation of the injected charge distribution and the electrostatic potential in graphene systems[74]. Moreover, the graphene strip in the system is assumed to be intrinsic with one electron per carbon atom; the system is ideally charge neutral throughout the graphene when the Fermi level is exactly at the Dirac point.

With the above restrictive conditions, we proceed to address the relation between the local carrier density and potential with the TF approximation, which can be written as: $n[V(r)] = -\frac{1}{\pi} \left(\frac{V(r)}{\hbar v_F}\right)^2$. Generalizing the formalism to a graphene-based field effect device

(see the inset of **Figure 2.3(b)**), the total potential as a function of the local charge density will be as follows:

Eq (2.11)

$$U(x) = -\hbar v_F \sqrt{\pi n_{el}(x)}$$

Where $U(x)$ is the electrostatic potential associated with the applied electric field, $n_{el}(x)$ is the effectively-injected charges which is position-dependent, and x is the planar position across the graphene channel.

At this point, it is possible to capture the distribution of electrostatically-induced charges by featuring the local potential across the graphene strip, which can be done experimentally using the Kelvin Probe Force Microscopy (KPFM). The scanning measurements technique is capable of localizing the charge-robust graphene edges as well as tracking the potential variations over the graphene channel with an applied external bias, with a resolution down to nanometer. The probed surface potential is considered to be a reproduction of the static charges in the system.

As previously mentioned, the self-consistent electrostatic potential can be obtained by solving the Poisson's equation. In the case of graphene (see the inset of **Figure 2.3(b)**), the graphene strip with finite width, a , lies on the SiO_2 surface with a depth, b , from the metallic gate. We reserve the coordinates x and z to be of interest with respect to the gate electrostatics of graphene devices. Therefore, the surface charge density is a function of x and z : $\rho(x)\delta(z)$, with $\rho(x) = en_{el}(x)$ in which n_{el} diverges as $1/\sqrt{x}$ towards the graphene edges[9]–[14], [75]. The response of graphene electrons to the external electric field can be estimated as follows:

Eq (2.12)

$$-\nabla^2 \phi(x, z) = \frac{en_{el}(x)}{\epsilon_{eff}} \delta(z)$$

The electrostatic potential $\phi(x, z)$ can be obtained using suitable boundary conditions from the solution to a two-dimensional Laplace equation[10], [71], and the image method is used to solve the gate electrostatic problem in graphene[10]. Here, rather than using the boundary element method for the calculation, we solve the spatial charge distribution in the classical parallel-plate capacitor model by solving the Poisson equation in a finite-element method solver. We consider a simple capacitor with an infinite size in which the charge density is homogeneous relative to the applied external electric field, as follows:

Eq (2.13)

$$n = \frac{\epsilon_{ox}}{e} \cdot \frac{V_g}{b} = \frac{C_{ox}}{e} V_g$$

Where ϵ_{ox} is the permittivity of the oxide dielectric, C_{ox} is the gate oxide capacitance, and b is the distance between the two "plates". The spatial charge distribution in a graphene strip capacitor can be approximately calculated from the classical capacitance profile $n_{el}(x) = \alpha(x) V_g$ and using $\alpha(x) = \alpha_\infty \frac{E_z(x)}{\min[E_z(x)]}$ [12], where α_∞ is obtained from

the infinite plane capacitor model which gives a homogeneous carrier concentration n_∞ . $\frac{E_z(x)}{\min[E_z(x)]}$ is introduced as a distribution function according to the relation: $n_{el}(x) = \frac{\varepsilon}{e} \cdot E_z(x)$. As $n_{el}(x) \sim \text{const} \cdot E_z(x)$, $\frac{E_z(x)}{\min[E_z(x)]}$ is therefore identified as the distribution (referred to as $\bar{n}(x)$) of the injected charges from the applied electric field, which is solved by normalizing the unscreened perpendicular field distribution, $E_z(x)$, to the minimum value $\min[E_z(x)]$ (which takes place at the center). α_∞ is obtained, as $7.19 \times 10^{14} \text{ m}^{-2} \text{ V}^{-1}$, when consider the parameters used in the experiments: $b = 300 \text{ nm}$ and $\varepsilon = 3.9\varepsilon_0$ for the insulator SiO_2 . The value of n_∞ approximately equals the carrier density at the center of the graphene strip and can be found using a finite-element solver, as shown in **Figure 2.3 (a)**. **Figure 2.3 (b)** shows the distribution of the stray filed lines under an applied gate voltage $V_g = 10 \text{ V}$; in this case, n_∞ approximately equals $7.19 \times 10^{15} \text{ m}^{-2}$ in the relation $n_\infty = \alpha_\infty V_g$. As graphene is treated as a perfect metal and grounded, the electric response to the applied electric field is extracted at a distance $z = +0.5 \text{ nm}$ (the graphene plane is set at $z = 0$).

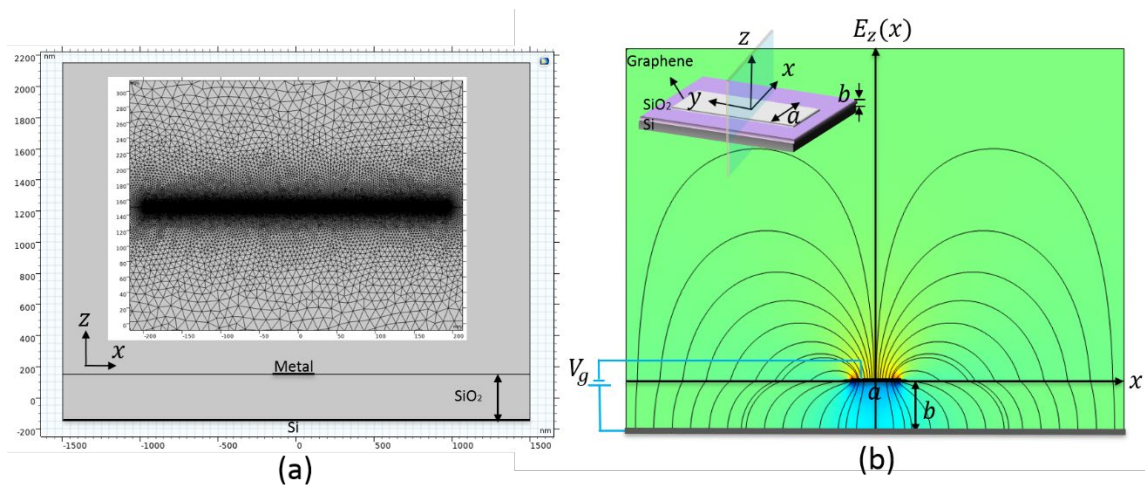


Figure 2.3 (a) The constituted 2D model in COMSOL. A graphene strip of width $a=100 \text{ nm}$, which is treated as a perfect metal, and the other metallic conductor Si are separated by an SiO_2 layer of 300 nm . The inset is the generated mesh near the graphene strip. (b) Schematic of the focused electric field and spatial distribution of the graphene strip. The inset in panel (b) shows a 3D view of the simulated graphene strip capacitor.

At this point, $n_{el}(x)$ is solved from $n_{el}(x) = n_\infty \cdot \bar{n}(x)$ combining with the computed results in the finite element solver; the in-plane charge density profiles of a graphene strip with a width of 100 nm for various gate voltages is demonstrated in **Figure 2.4 (a)**. The planar electrostatic potential can be obtained by using **Eq (2.11)**. **Figure 2.4 (b)** illustrates the potential profile of the graphene strip for $V_g = +10 \text{ V}$. Due to the really low one-dimensional density of states in the atomically thin graphene sheet, the electrostatic potential profile develops into an inverted “U” shape with downturned brims at graphene edges. The quantum-mechanical contribution is considered as the “graphene-specific”

potential with respect to modifications of the band structure [10]. It represents the position of the Dirac crossing point with respect to the Fermi energy, which is no longer stationary across the gated graphene strip. This is qualitatively different from any metallic strip with a rather flat constant potential (0 if it is grounded) in plane. The local potential profiles of a metallic strip as well as a graphene strip are shown in **Figure 2.4 (c)**; the gate voltage is $V_g = +10$ V.

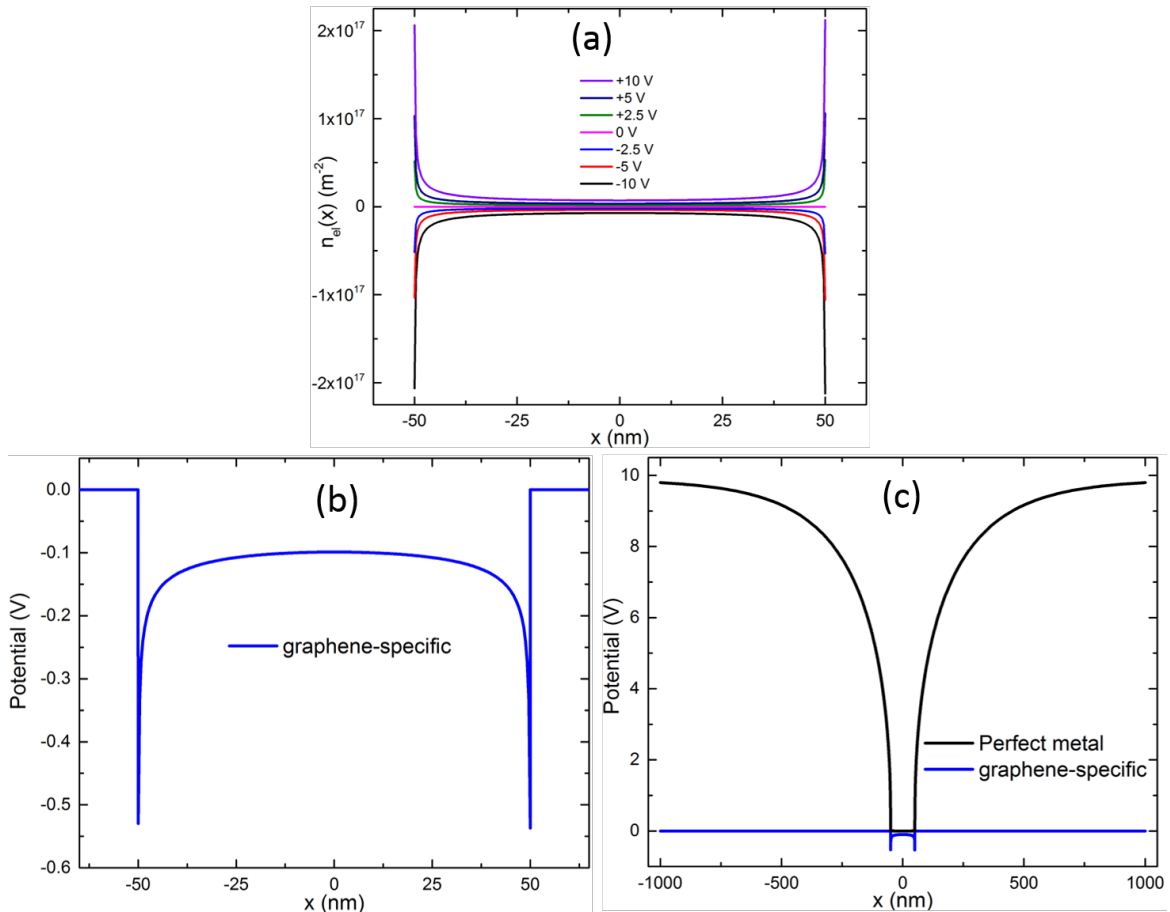


Figure 2.4 (a) The charge density profile across the graphene strip of width $a = 100$ nm with different gate voltages which is computed from the finite element solver. A striking charge accumulation at the graphene edges is expected. (b) A nontrivial graphene-specific potential across the 100 nm-wide graphene strip originating from the quantum effects, the applied gate voltage is $V_g = +10$ V. (c) We compute the in-plane electrostatic potential of a metallic strip with the same width of graphene strip to compare with that of graphene strip capacitor.

It is expected that our analytical model provides an adequate description of the gate electrostatics of graphene-based field devices as well as a qualitative inspection enabling visualization of the charge accumulation in realistic graphene samples through operational tools in the lab. The experimental details, such as imaging the local potential via KPFM, will be introduced in [Chapter 5](#).

2.4 Bubbles in the Van der Waals heterostructure

It is common to observe bubbles trapped beneath graphene layers during or after a transfer of graphene membranes because of the impermeability, mechanical flexibility, and mechanical strength of graphene. It has been reported that the presence of bubbles plays a crucial role in some properties of graphene. For example, its elastic and adhesive properties[76], [77] can be modified as a result of bubble-induced strain; its electronic properties can be modified by trapped charged impurities inside the bubbles, or by the deformed lattice structure around the rims of bubbles[27]; also highly strained nanobubbles have been found to induce pseudo-magnetic fields of up to 300 Tesla[23], [78].

graphene bubbles are also acclaimed in numerous applications. Georgiou *et al.* [79] demonstrated a possible graphene-based adaptive focus lens could be obtained by controlling the bubble curvature with an application of external bias. Gas storage technologies[24], [29], [30], [80] have also considered the mechanical robustness of graphene. Recently, strained bubbles were demonstrated as local emitters of photoluminescence[28]. Graphene bubbles have been extensively investigated both theoretically[78], [80], [81] and experimentally[24], [25], [27], [77], [79], [82], [83]: studies of bubble dimensions (their shapes, curvatures, pressures as well as radius and heights); the interplay between graphene and different substrates; trapped substances (such as hydrocarbons, air or water) inside bubbles; strain configurations and doping of bubbles from Raman spectroscopy; dynamic electrical transport in graphene, and electrostatic potential changes in bubbles.

Van der Waals (vdW) heterostructures, in which different atomically thin (2D) materials are physically assembled layer by layer, adhering mainly through weak vdW interactions, have become an active area of research with numerous applications[84]. Regarding the chemical bond-free integration, the interfaces are in principle contamination-free and atomically sharp[77], [83], [85]. However, during the assembly, hydrocarbons, water and air can be easily trapped at the interface, leading to either empty, air-containing or filled bubbles[86]. In a hBN-graphene-hBN heterostructure, bubbles could be presented either between top hBN and graphene or between graphene and bottom hBN. As of today, the interplay between bubbles, electronic properties and in particular charge distribution is not well understood.

3 Characterization Techniques

3	Characterization Techniques	15
3.1	Optical Microscopy.....	15
3.2	Raman Spectroscopy.....	17
3.2.1	Raman Spectrum of Graphene	18
3.2.2	Confocal Raman Microscopy	20
3.3	Atomic Force Microscopy (AFM)	20
3.4	Kelvin Probe Force Microscopy (KPFM)	23
3.4.1	Working Principle of Kelvin probe force microscopy (KPFM)	23
3.4.2	Amplitude Modulation Kelvin probe force microscopy (AM-KPFM).....	24
3.4.3	Frequency Modulation Kelvin probe force microscopy (FM-KPFM).....	26

3.1 Optical Microscopy

Optical microscopy (OM) is a rapid and non-invasive characterization technique, and has been widely used in the characterization of 2D materials. An optical microscope creates/displays magnified images of small objects via a system of objective lenses using visible light. The working principle is shown in **Figure 3.1 (a)**. First, a virtual image of the object is created by the objective lens, and then the eyepiece lens magnifies the virtual image of the object. The magnification can be adjusted by changing the objective or eyepiece lens. **Figure 3.1 (b)** shows the Nikon Eclipse L200N Series microscope, which is employed in this thesis.

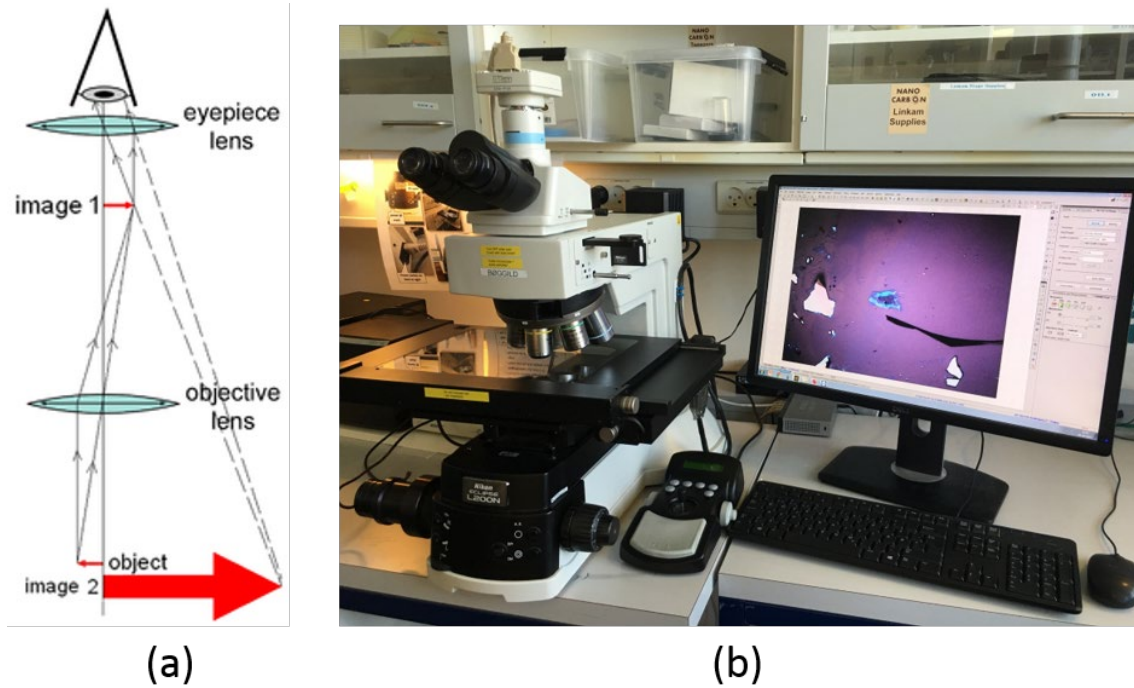


Figure 3.1 (a) Diagram of the working principles of optical microscopy, adapted from[87]. (b) The Nikon Eclipse L200N Series compound microscope employed in this thesis, which provides images with higher contrast and enables a better resolution for images of the object. When it is equipped with the digital camera, captured features can be displayed and saved on the attached computer.

Despite the fact that graphene is atomic thick, the microscope is still capable of discerning graphene sheets because of the difference in the optical contrast with respect to the supported substrates. For the case of graphene situated on SiO_2 layer, the contrast of graphene is related to the interference changes originating from the two reflection paths of the air-to- SiO_2 and SiO_2 -to-Si interfaces, which shows a dependence of the contrast on SiO_2 layer's thickness and the wavelength of light wavelength, λ [88]:

Eq (3.1)

$$C = \frac{I_{\text{SiO}_2}(\lambda) - I_G(\lambda)}{I_{\text{SiO}_2}(\lambda)}$$

Where C is the contrast of graphene, $I_{\text{SiO}_2}(\lambda)$ is identified as the intensity of the incident light with a wavelength λ reflected from the bare SiO_2 substrates, $I_G(\lambda)$ is correspondingly the intensity of light from the inspected graphene on the substrate.

Figure 3.2 (a) demonstrates the expected color plot of graphene as a function of SiO_2 substrate thickness and the incident light wavelength. Mechanically exfoliated graphene sheets on SiO_2 substrates of different thickness are inspected via OM here, as shown in **Figure 3.2 (b) and (c)**. Additional information can be discerned about the graphene layers from the OM images by using Raman microscopy. Here it is worth noting that the optical setup, light sources, and materials can create discrepancies in the value of $I_G(\lambda)$.

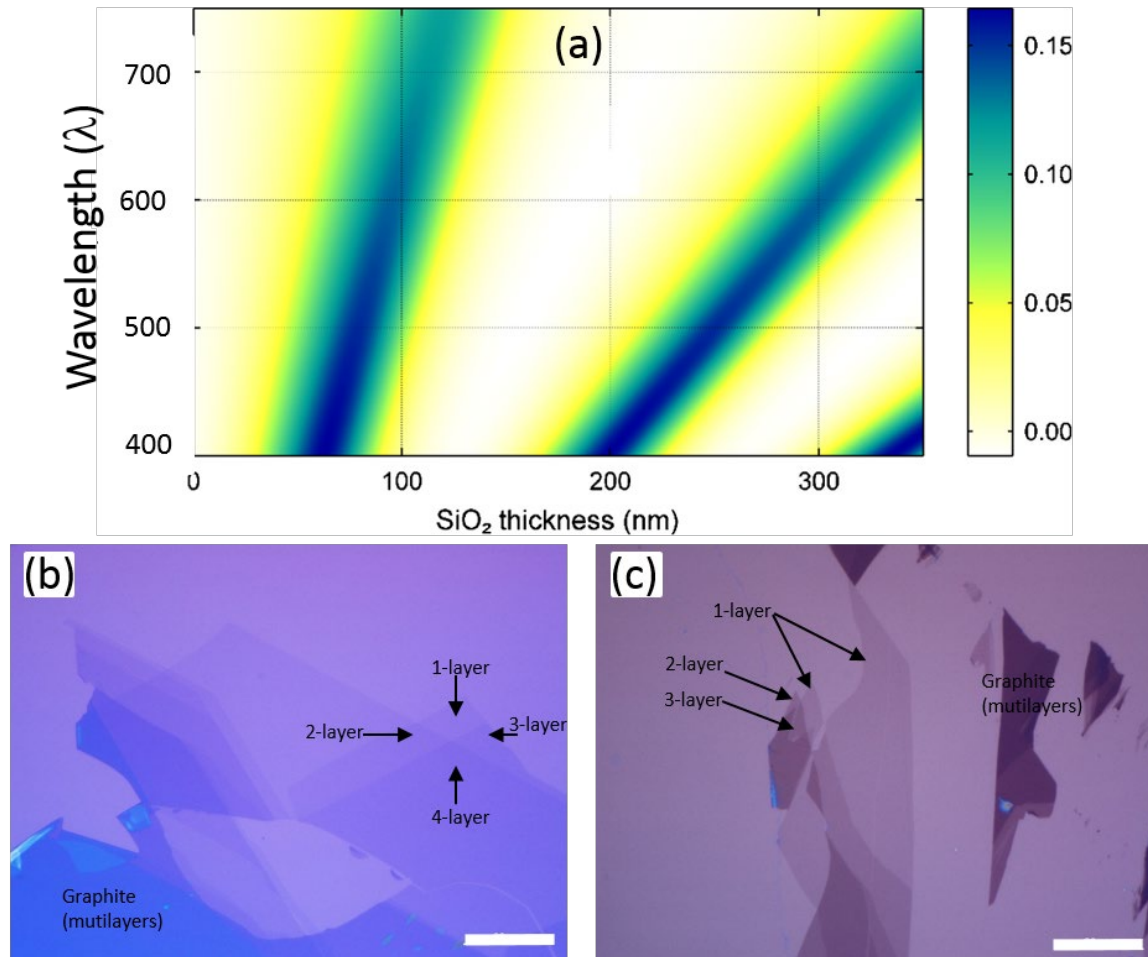


Figure 3.2 (a) Graphene contrast as a function of SiO_2 substrate thickness and wavelength of the incident light, adapted from [88]; (b)(c) Optical images of graphene flakes on SiO_2/Si , as obtained from the Nikon Eclipse L200N Series compound microscope. Combining with Raman microscopy, the information about the layers can be identified. As such, layer number of graphene can be empirically discerned from the contrast discrepancies of different graphene layers by fixing the optical setup. The scale bar is $20 \mu\text{m}$.

Additionally, **dark field imaging** in OM is also commonly used in the device fabrication process. Darkfield illumination can be described as the opposite of the bright field illumination; it eliminates scattered light from the sample image. Rather than illuminating the sample with the direct light, the scattered light enters the object lens and highlights the contours of the target sample. It is a simple but very effective technique to check characteristics of 2D material devices, such as the quality of exposure after electron-beam lithography.

3.2 Raman Spectroscopy

Raman spectroscopy is another versatile technique used for identifying and characterizing 2D materials. The Raman technique has been extensively used to check the effects, i.e. doping, strain, and disorder of graphene. It has historically played an important role in the structural characterization of graphitic materials.

3.2.1 Raman Spectrum of Graphene

A Raman spectrum is typically a unique (vibrational) fingerprint for a given material that features a number of peaks. Essentially, inelastic light scattering is mediated by the electronic polarizability of the medium. In the specific case of graphene, the in-plane σ -bonds-stabilized carbon atoms system provides a platform for forming an extended network of highly polarizable π bonds which results in an extremely intense Raman signal. An excellent review of Raman characterizing graphene can be found in [89]. The Raman spectrum has advanced the understanding of graphene in numerous ways: identifying the number of graphene layers, edges, disorders, and doping, strain [25], [90]–[95]. **Figure 3.5** shows the Raman spectrum of graphene placed on different substrates: SiO_2/Si , HMDS-rendered SiO_2 , and hBN-encapsulated graphene. The Raman measurements were accomplished using a DXR Raman Microscope with a 532 nm excitation laser. Typical parameters include a power of 1 mW and multiple exposures of 20 s to 30 s.

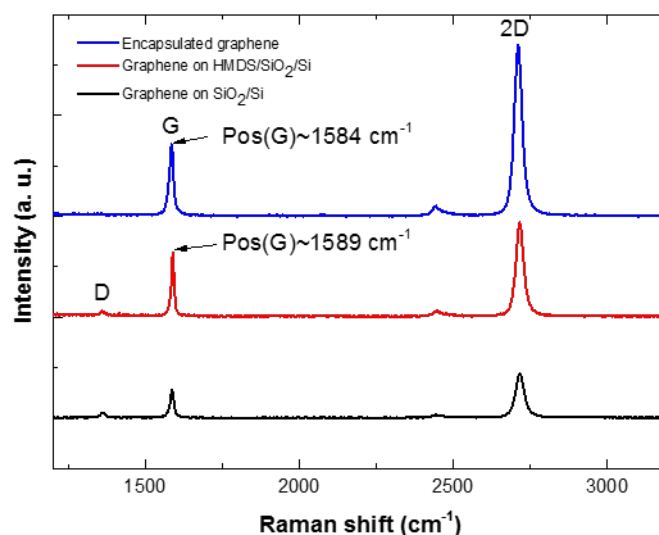


Figure 3.3 Raman spectrum of graphene on different substrates: the blue solid line is the case of graphene encapsulated in hBN layers, the red solid line is graphene deposited on HMDS-rendered SiO_2 (300 nm), and the black solid line is graphene exfoliated on 300nm SiO_2 .

Two prominent peaks are observed for pure single layers of graphene: the strongest 2D peak appears at about 2700 cm^{-1} , and the G peak typically appears at around 1580 cm^{-1} . In addition, an observable D peak near 1350 cm^{-1} only appears in the presence of disorders in graphene. The G peak corresponds to the in-plane sp^2 C-C bond stretching mode seen for all sp^2 carbon systems; both the 2D peak and D peak correspond to the in-plane

breathing-like modes of the six-carbon-atom rings[89], [91], but only the 2D peak is active for defect-free graphene.

A few items need to be introduced prior to further analysis of the graphene Raman spectrum. The peak position (ω_G , ω_{2D} and ω_D) can be affected by doping, which usually causes an upshift in ω_G and ω_{2D} . Mechanical strain in graphene also shifts the peak position. Peak intensity (**I**) with respect to other peaks, including I_D/I_G , indicates the degree of disorder in the graphene sample. The ratio I_{2D}/I_G is related to the number of layers; and combining with the full width at half maximum (**FWHM**), the quality of graphene can be identified[90], [95].

It is noted that both the strain (ϵ) and doping (n) contribute to the variations of the Raman frequencies of the G (ω_G) and 2D (ω_{2D}) modes. Lee *et al.* [96] were the first to separate the effects using both with a correlation analysis of ω_G and ω_{2D} , and a decomposition of ω_G and ω_{2D} into two vector components v_ϵ and v_n , as depicted in **Figure 3.4**. Mueller *et al.*[97] further introduced an approach enabling an evaluation of arbitrary strain configurations and simultaneous doping using Raman spectroscopy. In this method, the arbitrary strain is separated into a hydrostatic strain and shear strain, which can be evaluated from the peak shifts and peak splitting. Furthermore, hydrostatic strain can be separated from the doping using Lee's vector-based approach. More recently, Vincent *et al.* [82] concluded that explicit prerequisites were necessary for a more accurate analysis using this method: p-doped graphene with a low defect density is necessary because peak shifts originating from n-type doping does not change linearly, and the presence of defects also contributes to the variations of ω_G and ω_{2D} [96], as shown in **Figure 3.4**. Additionally, it has been demonstrated that the dielectric screening by the substrate will also cause a constant offset to the positions of ω_G and ω_{2D} as well [57], [98].

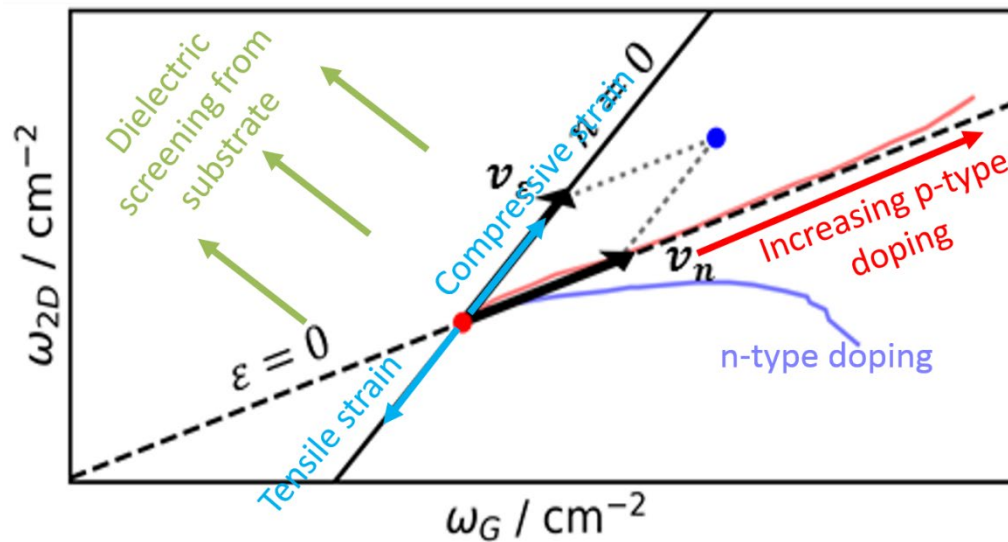


Figure 3.4 Schematic representation for showing the correlation between ω_G and ω_{2D} and the influences from strain, p- and n-doping as well as dielectric screening from the substrate on the position of the G-peak and 2D-peak. Hole doping induces linear shifts of ω_G and ω_{2D} while n-doping results in a non-linear decrease of ω_{2D} . The charge neutral point of zero strain ($\epsilon = 0$) and zero doping ($n = 0$) is marked by the red dot, adapted from[57].

3.2.2 Confocal Raman Microscopy

In confocal Raman spectroscopy, the laser source is focused to a small spot of $\sim 1 \mu\text{m}$ diameter using conventional microscopy objectives and pinhole apertures[99].

The confocal optical design can be used to reduce the sampling volume so that the spatial resolution improves, which helps to highlight the possible spectral differences between two adjacent points on the sample. With the aid of the confocal Raman microscope, we are capable of capturing more meaningful information about the interlayered defects in the graphene heterostructure and reveal the influence of the disorders in graphene-based devices (this will be further discussed in [Chapter 6](#)).

3.3 Atomic Force Microscopy (AFM)

Atomic force microscopy (AFM) is a scanning probe microscopy technique that has been widely used in the research field of 2D materials due to its high (sub-angstrom) spatial resolution. It constructs images by using a deflectable cantilever/sharp tip assembly, which is referred to as a microscopic probe to scan back and forth over the sample surface[100]. **Figure 3.5 (a)** gives a clear depiction of the working principle of AFM. When

the probe is brought into the proximity with the sample surface, the AFM tip, which is held at the end of the flexible cantilever, starts “touching” or “feeling” the raised and lowered features on the sample’s surface according to Hooke’s law: $F = -k \Delta z$. The extent of interactions between the tip and sample surface is then detected in terms of cantilever displacements. An incident laser beam attached to the back of the cantilever is used to inspect the cantilever displacements. The slight motions of the reflected beam with respect to the cantilever deflection are further monitored and captured by a position sensitive photo-detector (PSPD), as shown in **Figure 3.5 (b)**. The photo-detector consists of a four-segment photo-detector. Therefore, the topography of the sample is obtained through a raster scanning motion.

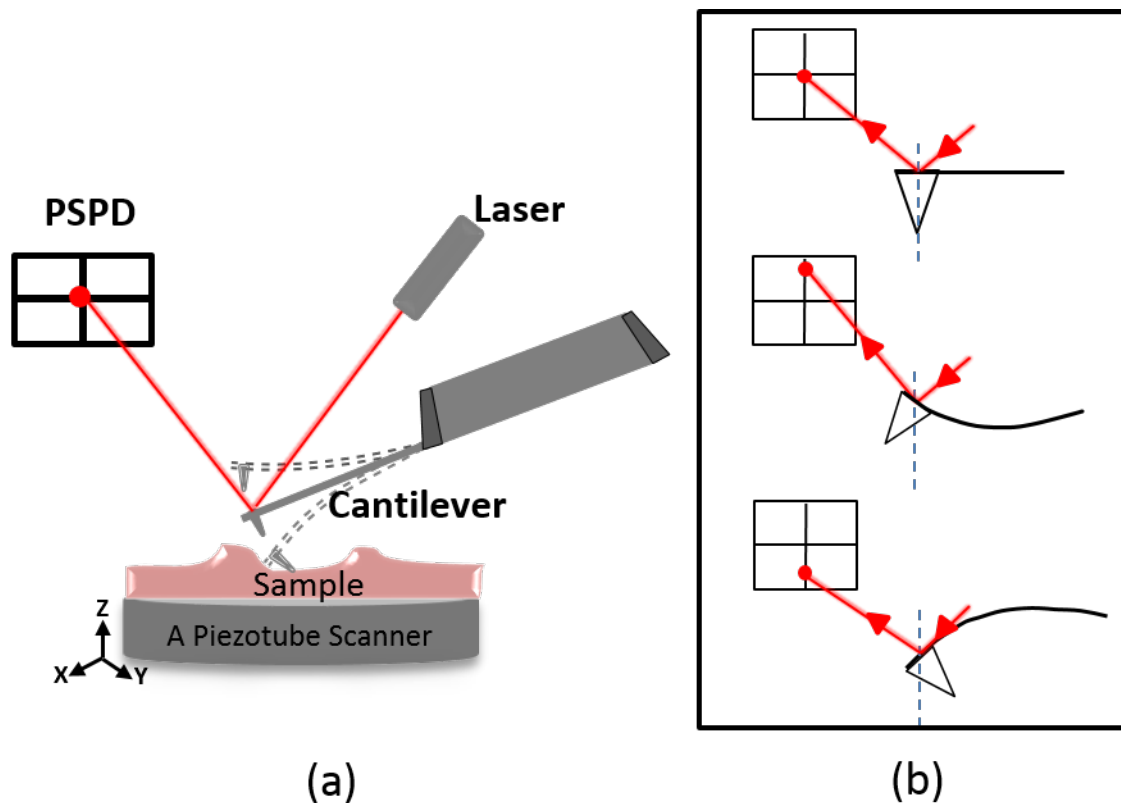


Figure 3.5 (a) An illustration of the working mode of AFM, adapted from [101]; (b) a schematic exhibits the detection configuration during the probe interacting with the sample with AFM.

There are two most commonly used operation modes for AFM: contact mode and tapping mode. In the contact mode operation, the tip gently physically “touches” the sample surface. During imaging, a piezoelectric positioning element is used to drive the probe sense the contour and simultaneously adjusts the movement through a feedback loop based on the raised and lowered features. The feedback loop either maintains a constant cantilever deflection corresponding to a pre-set load force or keeps the cantilever working

at a constant height¹. Meanwhile, the feedback response continuously outputs the height profiles of the scanning through to a PC. Since the tip here is in hard contact with the surface, the compression and shear force are generated between the tip and the surface damages the sample. However, this can be used to one's advantage. The forces occurring on the tip of the sample are usually at the nanonewton scale, which is equivalent to or less than the effective spring constant of the cantilever, which is on the order of 1~10 nN/nm. Most contact mode levers have a spring constant less than 1 nN/nm. Contact mode AFM can hence be used for a mechanical cleaning on 2D materials surface by scraping away the attached polymeric contamination[102], [103].

In the tapping mode, rather than "touching" the sample surface, to the device "feels" the interaction between the tip and the surface using a piezoelectric crystal. The cantilever assembly is thus driven to be oscillating at or near the cantilever's resonant frequency. When the probe is approaching the sample, the amplitude of the cantilever decreases, while it increases when there is more room for the cantilever to oscillate. A feedback loop is employed to maintain a constant cantilever oscillation amplitude by adjusting the motion of the probe. During scanning, the oscillating tip alternately contacts the surface and lifts off, which is why it is referred to as the "tapping" mode. As such, it is the variations of the cantilever amplitude that are detected and used to construct the topography map of the sample from raster scans. In this regard, the tapping mode is a key advance in AFM compared with the previous contact mode, since it avoids compromising the health of the sample surface, while also allowing for a detailed evaluation of the sample's surficial features.

AFM is an exceptional technique for characterizing 2D materials; it has been widely used to check the morphology, uniformity, roughness of graphene, and the underlying substrate[104], [105]. It is also useful for identifying the thickness of the hBN flakes with respect to the application in vdW heterostructure devices. In this study, AFM scans were performed using an NTEGRA scanning probe microscope from NT-MDT.

The AFM can be transformed into a more advanced scanning probe technique with locally minor modifications. For example, using a preamplifier, a voltage source, and a conductive probe a current image of the sample can be simultaneously obtained with the topography, which is referred to as the conductive atomic force microscopy (C-AFM).

It is an often-used technique for the characterization of electrical properties of a sample by imaging the conductivity or current[106]. In C-AFM, a current flows between the conductive tip and the sample due to the applied bias between them, and a preamplifier is used to convert the current signal into potential signals; at the same time, the topography is captured from a standard contact mode AFM. The resolution of local conductivity information can be down to the nanoscale, so C-AFM is very useful for characterizing the conductivity variations of resistive materials as well thin membranes,

¹ When the tip scans with a constant height above the sample in contact mode, which is actually equivalent to a slow or disabled feedback, it typically requires a relatively flat sample so that the feedback loop maintains the control over the probe during scanning. The constant height imaging method in contact mode is often used for atomic resolution AFM in high frequency scans.

such as graphene[107]. It is extremely reliable for the domain identification of epitaxial graphene[108]. The C-AFM was employed to assure the presence of graphene in the case of encapsulated by hBN in the work.

3.4 Kelvin Probe Force Microscopy (KPFM)

Kelvin Probe Force Microscopy (KPFM), which was first introduced by Nonnenmacher et.al. in 1991[109], like C-AFM, is another AFM-transformed technique. It is commonly known as a surface potential microscopy used for measuring the work function (as a function of potential difference) between the tip and sample in regard of the work function difference of both. Given the atomic resolution, KPFM is increasingly emerging as a key technique in a wide range of applications with respect to the measurement of local electrostatic properties, particularly for 2D materials, such as graphene[110], MoS₂ [111] or heterogeneous systems [64], [112], [113] that are structured on the nanoscale. The featured contact potential difference (CPD) can be used for work function measurements[62] as well as for visualizing the surface potential distribution[35], [110], [114]. With regard to this work, KPFM is employed to determine the local potential changes of graphene from the channel center to the edges to prove the charge accumulation at the graphene boundaries in realistic samples. The working principles of KPFM and two major detection techniques are introduced here.

3.4.1 Working Principle of Kelvin probe force microscopy (KPFM)

KPFM works by combining the Kelvin method with basic AFM principles. In 1898, Sir William Thomson (later known as Lord Kelvin) found that using an external wire to connect two separated metals with different work functions created a charge on the surface of the metal, forming a “contact potential”. Such a potential difference attributed to the work function difference can be nullified by applying a proper external bias. To clarify the working principles, a schematic is shown depicting the application of the Kelvin method in KPFM, in which a conducting tip with work function ϕ_{tip} and the sample with work function ϕ_{sample} act as the two metals (see **Figure 3.6**).

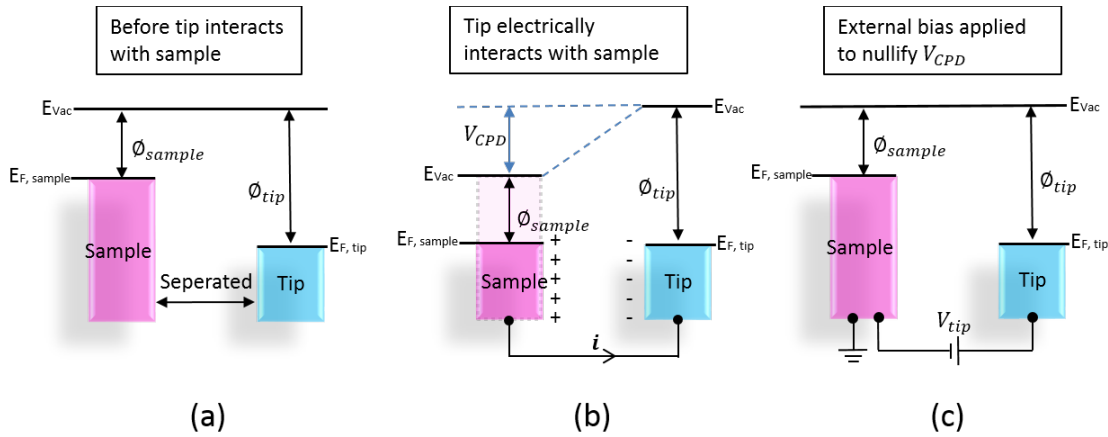


Figure 3.6 An energy levels diagram depicting the Kelvin probe force principle: (a) in an open circuit, the tip and sample are separated, with an aligned vacuum energy level (E_{vac}); $E_{F, sample}$ and $E_{F, tip}$ are respectively the Fermi levels of the sample and tip; (b) in a close circuit, a flow of current transfers charges to equalize the Fermi levels, V_{CPD} is the quantitative transferred charges. (c) Applying an external bias (V_{tip}) can compensate for the charges V_{CPD} and nullify the polarization, adapted from[113].

Figure 3.6 (a) depicts the energy level diagram in an open circuit where the Fermi levels of the tip ($E_{F, tip}$) and the sample ($E_{F, sample}$) are at different positions by aligning the vacuum levels E_{vac} . Subsequently, with the electrical contact shown in **Figure 3.6 (b)**, electrons from the sample (with a higher Fermi energy) will flow from the sample (with a lower work function) to the tip (with a higher work function) so that the $E_{F, tip}$ and $E_{F, sample}$ line up to a steady state approaching an equilibrium. As a consequence, an electrical potential V_{CPD} which equalizes the work function variation $V_{CPD} = \frac{\phi_{tip} - \phi_{sample}}{-e}$, is generated due to the new equilibrium position of the Fermi levels in the close circuit. The electric field created by V_{CPD} (the contact potential difference between the tip and the sample) induces equal and opposite charges on the surfaces of the tip and sample, simultaneously giving rise to an electrostatic force F_{el} . The external bias (V_{tip}) between the tip and sample is regulated to compensate for the charge difference, F_{el} , can be nullified if V_{tip} has the same magnitude as V_{CPD} but different polarity as illustrated in **Figure 3.6 (c)**. Therefore, ϕ_{sample} can be calculated with a known ϕ_{tip} .

KPFM and AFM utilize similar hardware; however, in KPFM an external bias is applied in the feedback loop, which is used to modulate the conductive probe based on the interaction between the tip and sample surface. There are two major detection techniques: amplitude modulation KPFM (AM-KPFM) and frequency modulation KPFM (FM-KPFM), which work based on the electric force and the electric force respectively.

3.4.2 Amplitude Modulation Kelvin probe force microscopy (AM-KPFM)

AM-KPFM is operated based on monitoring the probe's deflection caused by the electric force, F_{el} , between the tip and sample. Here F_{el} reads

Eq (3.2)

$$F_{el} = -\frac{1}{2} \frac{\partial C}{\partial z} (\Delta V)^2$$

Where $\frac{\partial C}{\partial z}$ represents the potential gradient of the tip-sample surface capacitor and ΔV is the surface potential difference, given as:

Eq (3.3)

$$\Delta V = V_{DC} - V_{CPD} + V_{AC} \sin(\omega t)$$

Where the voltage $V_{tip} = V_{DC} + V_{AC} \sin(\omega t)$ is the applied external bias on the tip including a DC voltage and an AC voltage, $\omega = 2\pi f_0$. By substituting **Eq (3.3)** into **Eq (3.2)** and separating the spectral components, the electrostatic force can be written as: $F_{el} = F_{DC} + F_{\omega} + F_{2\omega}$, where:

Eq (3.4)

$$F_{DC} = -\frac{\partial C}{\partial z} \left(\frac{1}{2} (V_{DC} - V_{CPD})^2 + \frac{1}{4} V_{AC}^2 \right)$$

Eq (3.5)

$$F_{\omega} = -\frac{\partial C}{\partial z} (V_{DC} - V_{CPD}) V_{AC} \sin(\omega t)$$

Eq (3.6)

$$F_{2\omega} = \frac{\partial C}{\partial z} \frac{1}{4} V_{AC}^2 \cos 2\omega t$$

The DC component, F_{DC} , is the tip's response to the topography of the sample. F_{ω} , $F_{2\omega}$ are the tip's oscillation at the first and second harmonic frequency components, respectively. As shown **Figure 3.7 (a)**, the amplitude of the cantilever is detected using the conventional AFM "optical leverage" and a lock-in amplifier tuned to the frequency, f , of the AC-bias V_{AC} . By adjusting the V_{DC} based on the initial amplitude until it equals V_{CPD} , the oscillation amplitude $F_{\omega}(f)$ will drop to zero. The frequency of the AC-bias is typically selected to be the resonant frequency, f_0 , of the cantilever for an enhanced sensitivity. AM-KPFM can be executed either in a single pass[113], where topography and surface potential are obtained at the same time, or in a lift mode (also known as a dual-pass scan), which is exclusively used in the experiments discussed here, see **Figure 3.7 (b) and (c)**.

In the dual pass scan, the cantilever is mechanically vibrated at (or near) its resonant frequency using a standard tapping mode in the first pass. In the second pass, the mechanical excitation of the cantilever is deactivated, the tip is raised to at a set lift height

(~ 5 nm) and the sample surface potential is detected with the applied V_{AC} . The V_{AC} -induced oscillatory force is minimized when V_{CPD} is nullified by the V_{DC} . Mapping $V_{DC}(x)$ allows us to obtain the surface potential distribution of the sample surface.

In the AM-KPFM mode, changes in the oscillation of the amplitude provides the feedback signals of the surface potential. It provides a good potential sensitivity while since it collects the feedback signal at a lifting height above the sample, the lateral resolution is hence decreased.

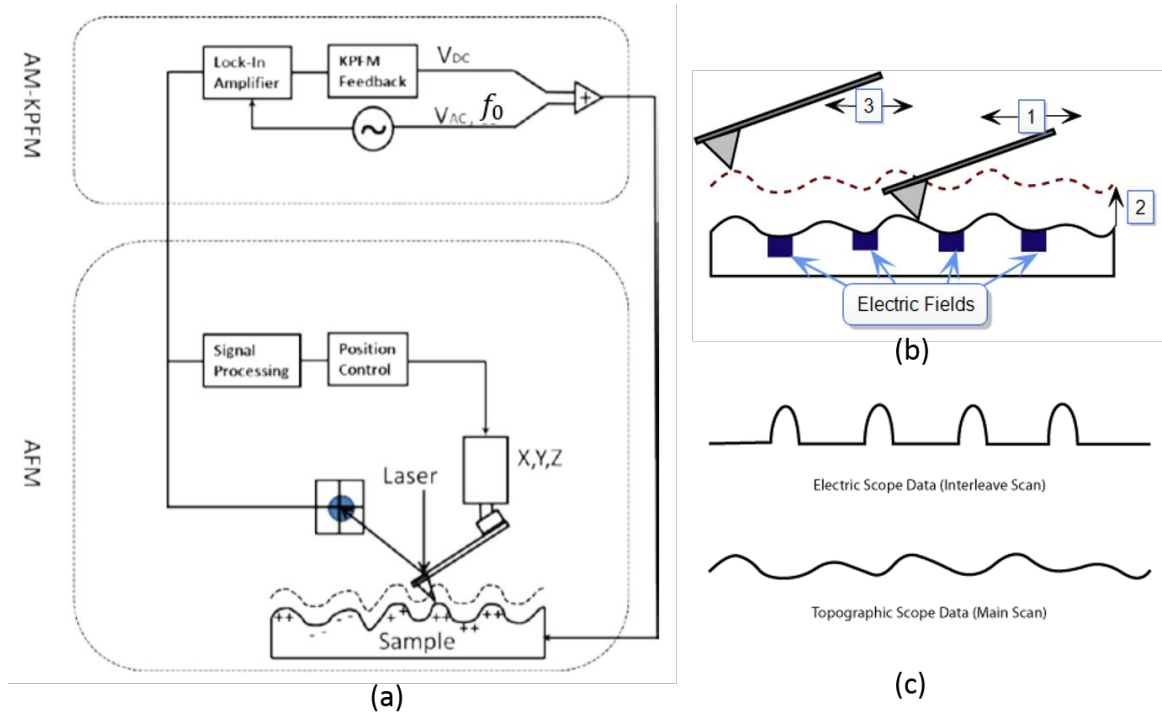


Figure 3.7 Schematic diagram of a lift-mode AM-KPFM (adapted From [115]): (a) The AM-KPFM configuration; (b) ① depicts topography measurements in the first pass which corresponds to the lower part of (c), ② ③ illustrates the working motions of the tip in the second pass, which indicate the surface potential as shown in the upper portion in (c).

3.4.3 Frequency Modulation Kelvin probe force microscopy (FM-KPFM)

In contrast to AM-KPFM, FM-KPFM detects the electric force gradient F'_{el} , which is associated with the electric force $F_{el} = \frac{\partial F_{el}}{\partial z}$, to capture the contact potential difference, V_{CPD} , between the tip and the sample. This is done through monitoring the cantilever resonant frequency shifts (Δf) caused by modulating F'_{el} via V_{AC} . FM-KPFM can also be executed in a single pass or a dual pass.

In single-pass FM-KPFM, the cantilever oscillates at its resonant frequency (f_0), and simultaneously apply an AC bias, V_{AC} , at a modulated frequency, f_m , (usually around 1~5

kHz^2) which introduces a frequency shift ($f_0 \pm f_m$). The modulation of the resonant frequency (f_0) generates two side bands at ($f_0 \pm f_m$). It is the amplitude of the side bands measured through a cascaded lock-in amplifiers that is used as the feedback signal when a DC voltage matches the V_{CPD} , see **Figure 3.8**. The surface potential of the sample can be constructed by measuring the compensated DC voltage.

FM-KPFM is sensitive to the electric force gradient working at a short-range, which is more likely confined to the dimensions of the applied tip. Hence, a higher spatial resolution of < 20 nm can be achieved.

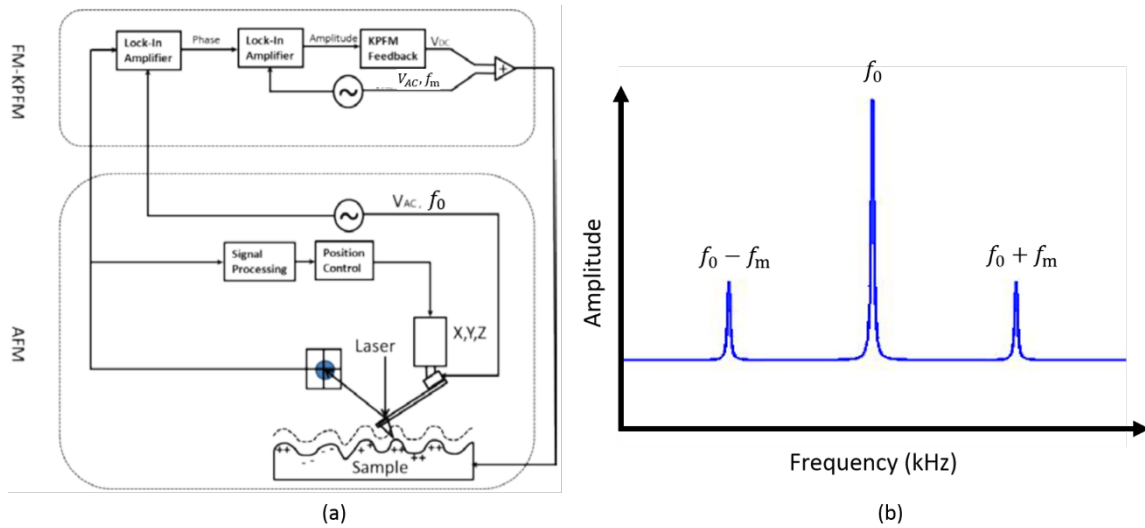


Figure 3.8 (a) A schematic of the frequency spectrum of the cantilever oscillation in FM-KPFM, adapted from [115]; (b) A diagram for showing the generated side bands at the frequency spectrum of the cantilever with the application of the AC bias.

Both AM mode KPFM and FM mode KPFM have played a prominent role in characterizing 2D materials [64], [110], [111], [116], [117] [64], [110], [111], [116], [117]. In this thesis, KPFM has been employed to explore the gate electrostatics of narrow gated graphene devices in terms of the local potential distribution over the channel as a function of the external gate bias as well as the edge disorders. This will be introduced in [Chapter 5](#).

² Since the probe employed in this work is PFQNE-AI from Bruker, a silicon probe with a nitride cantilever, $f_0=300\text{kHz}$, a $f_m \approx 5$ kHz and the modulated AC bias is around 3~5 V have been used for the single-pass FM-KPFM.

4 Sample Preparation and Fabrication

4.1	Substrate Preparation	29
4.2	Isolation and Identification of Graphene and hBN.....	31
4.2.1	Exfoliations and Transfer on Different Substrates	31
4.2.2	Identification of Graphene and hBN.....	33
4.3	Van der Waals (vdW) Heterostructure Assembly	34
4.3.1	Preparation Work Before the Assembly.....	34
4.3.2	Standard Hot Pick-up Technique for hBN/graphene/hBN Stack.....	36
4.3.3	Modified Hot Pick-up Technique for Thin hBN/graphene/hBN stack.....	40
4.4	Device Fabrication	42
4.4.1	Electron Beam Lithography	42
4.4.2	Device Fabrication Process Flow	42

4.1 Substrate Preparation

Graphene can be strongly influenced by the underlying substrate since the unavoidable morphological roughness, charge impurities, and contamination that contribute to the electron scattering[118], will, in turn, significantly affect the performance of the device . Therefore, it is essential to clean the substrate before the transfer of mechanically exfoliated graphene flakes.

The following substrate cleaning procedure was used in this work:

- i. A N₂ gun was used to remove the surficial solid particles such as particles, dusts etc.
- ii. A chip holder was utilized to support and isolate the chips so that they could be soaked in warm acetone(80°C, 10 minutes).
- iii. Later the chips were rinsed in methanol and blow-dried.
- iv. The chips were soaked in acetone and placed in an ultrasonic bath for 15 minutes.
- v. Isopropanol (IPA) was used for rinsing, and N₂ was used for blow-drying.

In conjunction with the ultrasonic bath, this cleaning procedure is capable of eliminating oils and organic residues. Various adsorbates from the ambient air can easily attach themselves to SiO₂ during the transfer process. For instance, the silanol groups (SiOH) can be formed from the coupling between hydroxy groups and the dangling Si bonds. Dipolar molecules, like water, can easily attach to SiOH to be the sources of electron scattering. The often observed p-doping in graphene is believed to originate from the adsorbed water molecules. Apart from being undesirable obstacles, such inevitable impurities will eventually degrade the intrinsic notable electronic performance in graphene devices[46], [68], [119]–[121]. It should also be noted that surface roughness likely plays a crucial role

in graphene's final morphology. Local strain and curvature can undermine the structural symmetry, which can modify the electronic properties of graphene (for example lowering the mobility) [122]. It has been demonstrated that feasible modifications of SiO_2 will moderately ameliorate such detrimental effects. Examples of modifications include suspending graphene samples [45], hydrophobically rendered SiO_2/Si substrates [56], isolated graphene from SiO_2 by assembling the van der Waals heterostructures [44].

A hexamethyldisilazane (HMDS)-modified SiO_2 substrate and van der Waals heterostructures are both employed in this thesis to achieve better performances of graphene devices. Following sections will introduce the details of each technique.

Preparation of Hydrophobically-rendered SiO_2/Si Substrates via HMDS

As discussed earlier, the silicon oxide surface will always initially be saturated with hydroxyl groups ($-\text{OH}$) in the presence of air, building up a layer of SiOH that has proved to be responsible for the intrinsic doping and hysteresis of electronic transport in graphene. HMDS priming has become a well-known process to make the substrate hydrophobic. The synthesis pathway for the HMDS-modified silicon oxide is shown schematically in **Figure 4.1**.

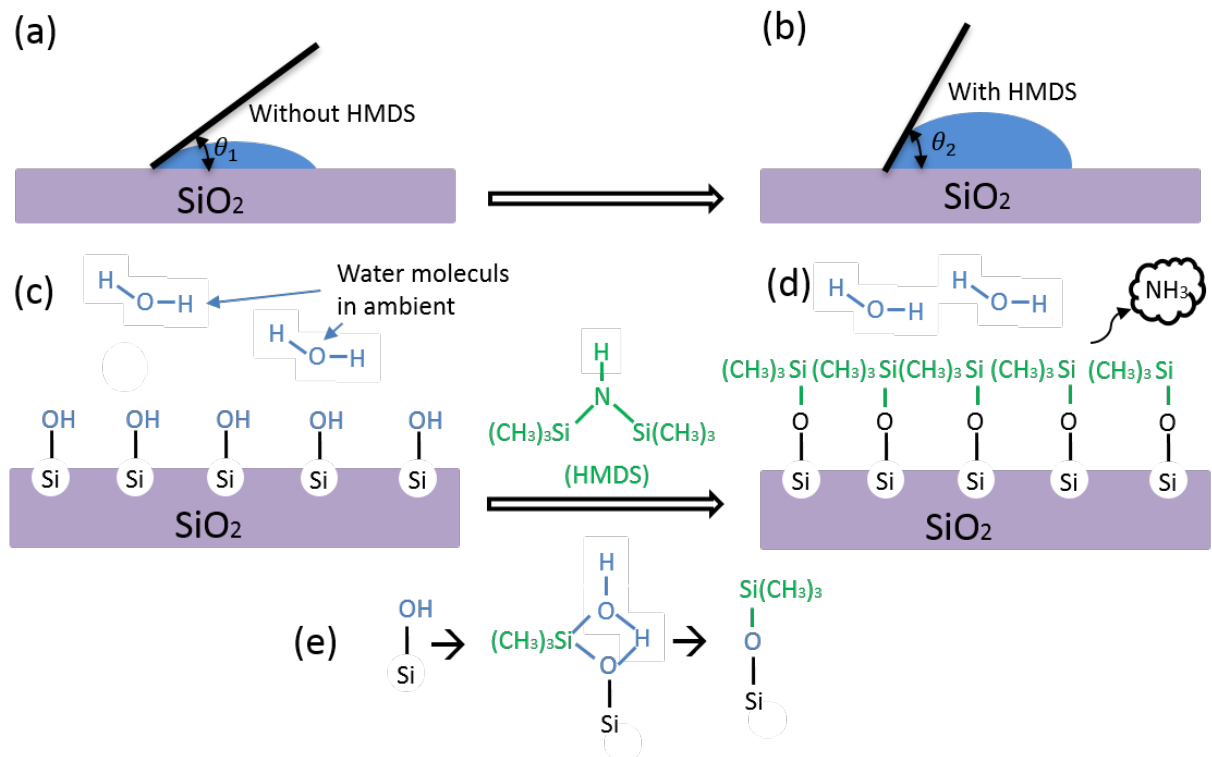


Figure 4.1 The HMDS-modified SiO_2 process with taking water molecules on behalf of the dipolar adsorbates, adapted from [123]. (a)(b) A schematic diagram of the contact angles of a water droplet with the substrate surface before and after the hydrophobic priming process; (c) Surface states of silicon oxide when exposed to ambient air; (d) The surface states of the silicon oxide during/after dipping in HMDS solution (e) A streamlined illustration of the chemical reactions of the process.

The contact angle calculations were performed here by applying a spherical approximation model of the drop. The contact angle, θ_2 , can reach between 65° and 80° after HMDS treatment, but θ_2 can vary with a strong dependence on parameters, such as synthesis temperature, time and chemical density. In the case of water, HMDS functions like an alkoxy silane, replacing -OH groups with hydrophobic methyl groups. The HMDS then binds to the surface via its “Si-atom to the oxygen-atom” of oxidised substrates and ammonia (NH₃) is released, as shown in **Figure 4.1 (c)-(e)**. A substrate decorated with more hydrophobic methyl groups has a lower surface energy, and hence a higher water contact angle.

The configuration of HMDS priming process is outlined as below:

- i. The HMDS solution was prepared. The hexamethyldisilazane solution consisted of acetone with a volume ratio of 1:1; the solution was dispensed into a petri dish.
- ii. The SiO₂/Si chips were ultrasonically re-cleaned in acetone and IPA; the chips were subsequently dipped chips in IPA 3~5 s. The chips were dipped in the solution after drying the chips with an N₂ gun.
- iii. The petri dish was covered with another petri dish of a suitable size, and the two were sealed with laboratory parafilm. The dish was kept still in the fume hood for 14-16 h under seal.
- iv. Samples were rinsed in acetone and dried with N₂.

Graphene was then transferred onto the HMDS modified substrate by mechanical cleavage with scotch tape. The assembly of the Van der Waals heterostructures will now be introduced, followed by the cleavage process.

4.2 Isolation and Identification of Graphene and hBN

4.2.1 Exfoliations and Transfer on Different Substrates

Graphene-like layers-laminated 2D materials can be mechanically exfoliated from the bulk crystals by simply using scotch tape [85], [124]. The cleavage process of graphene and hBN will be discussed here. Graphite “Flaggy flakes” from NGS Trading & Consulting GmbH and hBN bulk crystals from HQ Graphene were used for the exfoliation. Two types of tape were employed here to accomplish the different exfoliations of graphene and hBN: 3M Scotch® 810 Magic™ tape for graphene exfoliation (scotch tape), and blue semiconductor wafer tape SWT20+ from Nitto Denko (blue tape) for hBN cleavage.

To create the graphene “master” tape, the bulk graphite was first cleaved until the surface became shiny. The shiny side was then adhered to the tape at many locations until the tape was fully covered in graphite, and this is referred to as the graphene “master” tape. Another new piece of tape (the “copy” tape) was used to fully cover the “master” tape.

The “copy” tape was used on the chips. A hBN “master” and “copy” tape was obtained by the same method using the blue tape, see **Figure 4.2 (a)**.

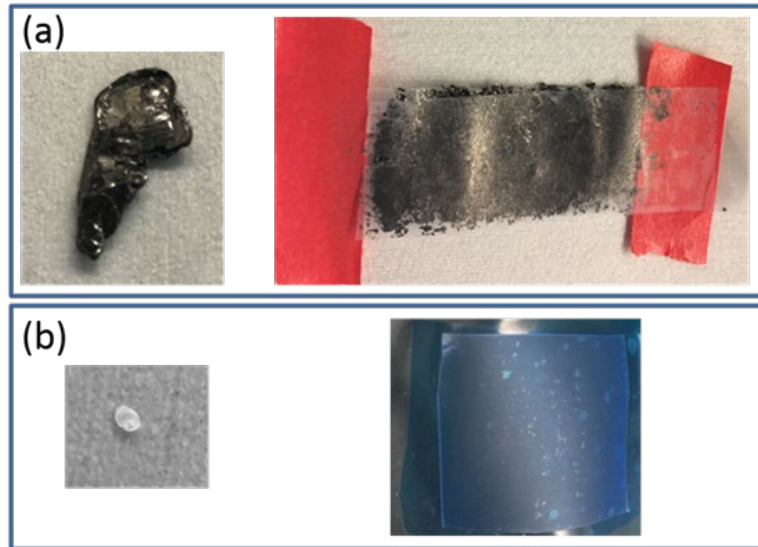


Figure 4.2 (a) bulk graphite and the configuration of the graphene “copy” on scotch tape; (b) hBN crystal, and the configuration of the hBN “copy” on the blue tape.

Graphene exfoliation/transfer on SiO₂/Si

Large area graphene flakes can be obtained from oxygen plasma treated SiO₂/Si substrates[60]. Hence, the following procedure was used to obtain larger graphene flakes at a higher yield. A LASMA ETCH Plasma Asher was employed for the treatment.

- i. The SiO₂/Si chips were treated for 8 minutes with oxygen plasma, RF power 40%, vacuum pressure 400 mTorr;
- ii. The copy tape was used immediately after taking the chip out from the chamber;
- iii. It was ensured that the tape had adhered properly by rubbing with either a rounded pen tip or a finger;
- iv. The tape was lifted laterally at a low angle;
- v. The position of the graphene flakes and the layer thickness was identified with OM or Raman microscopy.

Graphene exfoliation/transfer on HMDS-rendered SiO₂/Si

Note that the actual exfoliation of the monolayer graphene samples or graphene samples with few layers is a competition between (1) the attractive force of the layers of graphite (vdW force), (2) the force from tape and (3) the outermost layer which adhered to the substrate. A smaller yield is obtained when exfoliating graphene on HMDS treated SiO₂ because the adhesion between the layered crystals and the substrate becomes much weaker when the substrate is hydrophobic. In addition, oxygen plasma was not used, which resulted in a much smaller yield both in terms of the size and numbers of graphene

flake on the modified SiO₂/Si substrates. Hence, an annealing process is introduced before peeling off the tape from the substrate. The optimized annealing temperature and time are 70°C and 10 minutes, which would result in the largest yield and the least amount of glue residuals from the tape.

hBN exfoliation/transfer on SiO₂/Si

Due to the lower adhesion of the blue tape used for the hBN exfoliation, rather than the straightforward peeling-off of the tape during graphene exfoliation on SiO₂/Si, a gentle annealing was applied when releasing the hBN substrate from the tape. The chip was baked at 80°C for around 1 minute and was gently removed from the hot plate, since the baking decreased the adhesive force from the blue tape, yielding more hBN flakes on the substrate.

4.2.2 Identification of Graphene and hBN

Thickness determination and the identification of the flake positions are crucial steps in fabrication with graphene and hBN. Apart from using the gold alignment marks on the wafer (see **Figure 4.3 (a)**), as introduced in [Chapter 3](#), optical microscopy (OM) and Raman spectroscopy were employed to identify and locate flakes, as shown in **Figure 4.3**.

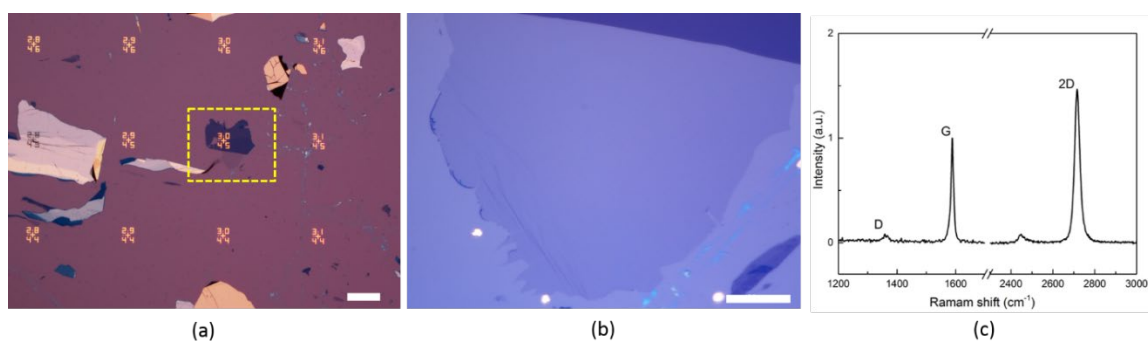


Figure 4.3 Identification of graphene flakes. (a) An overview of an exfoliated graphene on a SiO₂/Si chip with gold alignment marks on; a yellow dashed rectangle outlines the region of interest, the OM image is captured with x10 magnification with a scale bar of 200 μm; (b) A zoomed-in OM image of the highlighted area with x100 magnification, a monolayer graphene is clearly seen, the scale bar is 20 μm; (c) A Raman spectrum of the graphene.

OM is also suitable for distinguishing hBN flakes. **Figure 4.4** shows the optical images of hBN with different thicknesses. The thickness was first determined by AFM, which was performed using the NTEGRA Aura SPM Platform from NT-MDT. The color of the hBN was then correlated with different thicknesses, allowing the thickness of the hBN sample to be directly evaluated from OM.

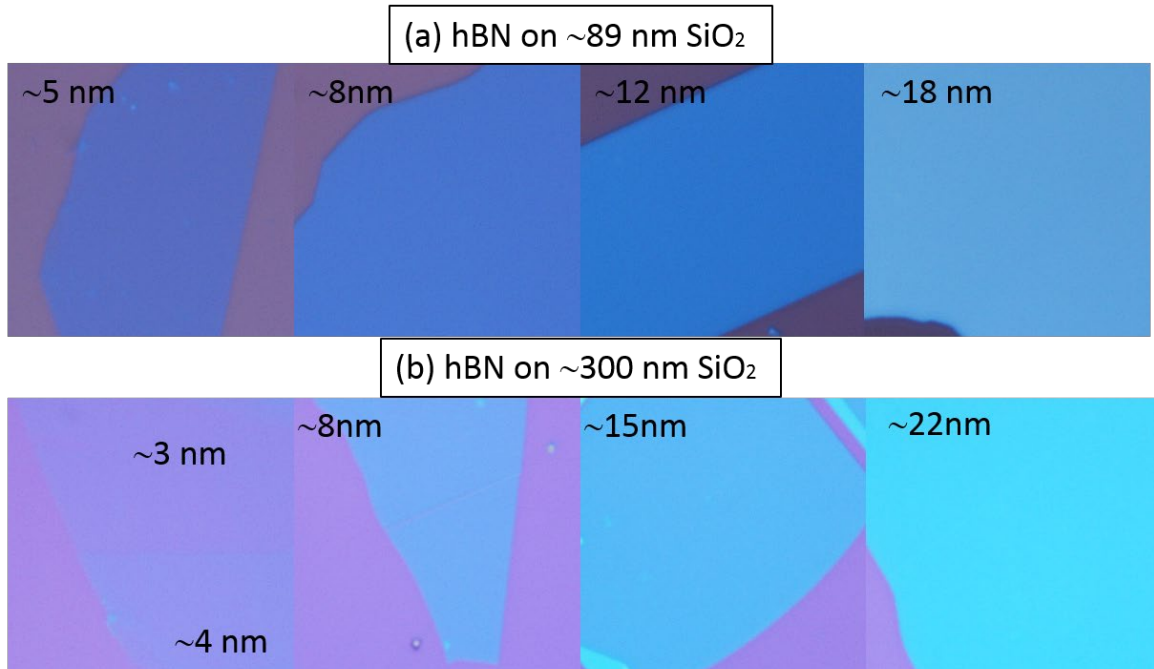


Figure 4.4 (a)(b) OM images of varying contrasts for hBN supported by different thickness of SiO₂ substrates; thickness identified by AFM.

4.3 Van der Waals (vdW) Heterostructure Assembly

The van der Waals (vdW) integration, in which several building blocks are manually assembled together through weak vdW interactions, provides an effective strategy for studying the 2D materials. A recently improved vdW pick-up technique developed by Pizzocchero, F et al. [86] in our lab has been recognized for producing high-quality encapsulated graphene devices, and hence is fairly employed and referenced in this thesis for hBN/graphene/hBN integration.

4.3.1 Preparation Work Before the Assembly

As illustrated in **Figure 4.5**, crystals cleavage, flake location, and stamp preparation need to be performed prior to the assembly process. The exfoliation, flake selection, and location were conducted as described in [Section 4.2](#). The preparation of the PDMS/PPC stamp will be briefly introduced here.

A two-part silicon elastomer product called SYLGARD™184 Silicone Elastomer was used for PDMS preparation. The product includes a polydimethylsiloxane elastomer and curing agent which are supplied as liquid components. The polydimethylsiloxane elastomer and the curing agent were manually mixed with a ratio of 10:1. A dose of ~120 mg/cm² was dispensed directly into a clean petri dish, where a PDMS with a thickness of ~1 mm was

obtained. A de-airing process was performed by standing the dish in a desiccator for approximately 2 h to eliminate the air entrapment. An overnight heating process at 70°C was applied for a faster cure. A PPC (molecular weight 50K) solution of 5wt% was prepared on the PDMS block after a 10-min plasma-cleaning. The PDMS/PPC block was baked at 60°C for about half an hour, and the block was manually cubed into an appropriate size (~4mm²). The individual mini PDMS/PPC cubes were glued on the glass slide in preparation for the stacking. A prototype of the glass-based PDMS/PPC stamp is shown in **Figure 4.5 (c)**. The PPC priming was applied to increase the adhesion for picking up the flakes.

The employed experimental setup (referred to as a “stacker”) is shown in **Figure 4.5 (a)**. It includes an optical system and a micro-positioning system. With the optical system, one can locate the target flake. A metaldisc heater with vacuum clamping can heat up the sample while simultaneously fixing it. The glass-based PDMS/PPC stamp is mounted on the micromanipulator and can be locked by the steel plates with one pair of screws, as indicated in **Figure 4.5 (b)**. A xyz-micromanipulator and a tilt controller execute the stacking process. The xyz-micromanipulator allows for precise alignment by full cooperation with the optical transport hub, and the tilt controller can obtain a good alignment between the stamp and chip as well as ensuring that the stamp approaches the target flake at a proper angle.

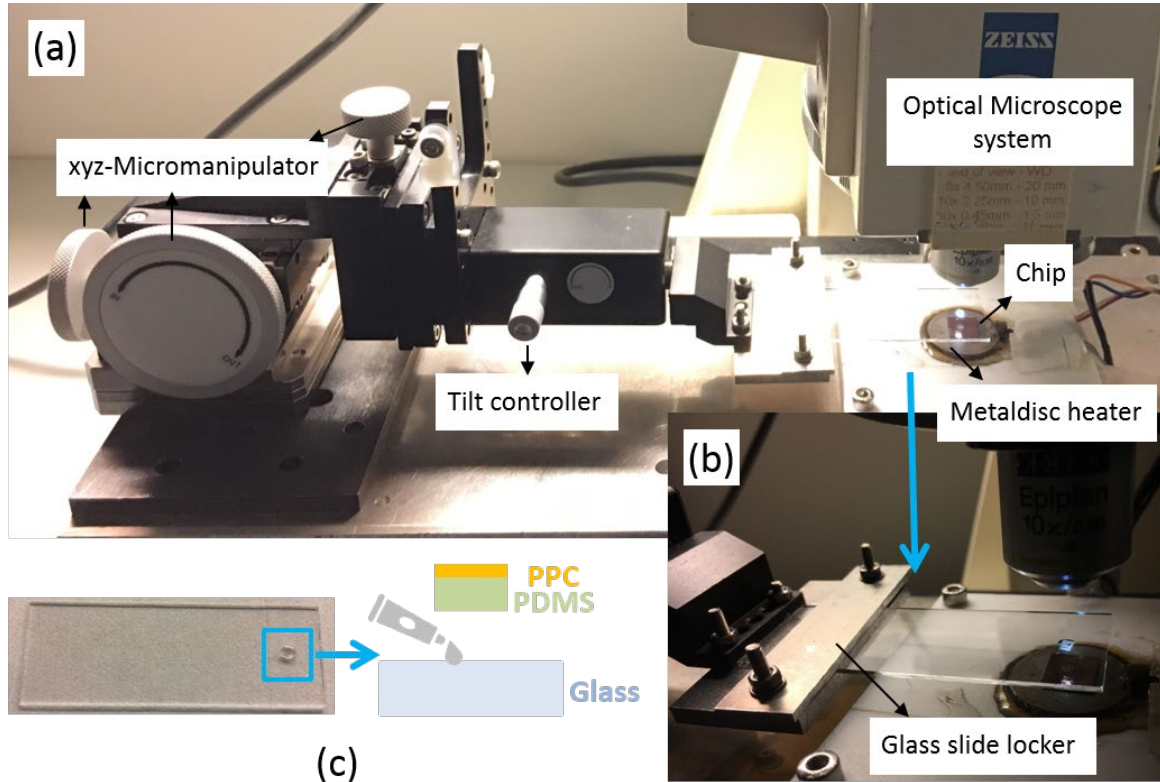


Figure 4.5 The experimental setup for stacking at a full-ready working mode. (a) Composition annotation of the employed apparatus for the hot pick-up stacking (stacker); (b) A detailed view of the mounted glass-based PDMS/PPC stamp; (c) A glass-based PDMS/PPC stamp with an anatomy of the stamp.

4.3.2 Standard Hot Pick-up Technique for hBN/graphene/hBN Stack

An explicit diagram of the assembling process is illustrated in **Figure 4.6**, showing the hot pick-up technique. The temperature variant plays a critical role. This is because the viscosity of PDMS/PPC[125], the adhesion between graphene and hBN, and the attaching force between the flake and substrate are all, to a certain extent, dependent on the temperature. A temperature above 100 °C increases the vdW interaction between hBN and graphene. When the stamp picks up the hBN flake from the chip, heating the system up to 110 °C can help to separate the graphene flake from the plasma-treated SiO₂. Moreover, appropriate heating can help de-wrinkle a half stack (top hBN+graphene) or a full stack (hBN/graphene/hBN)[86]. Therefore, the operating temperature is critical for a high quality hBN/graphene/hBN stack.

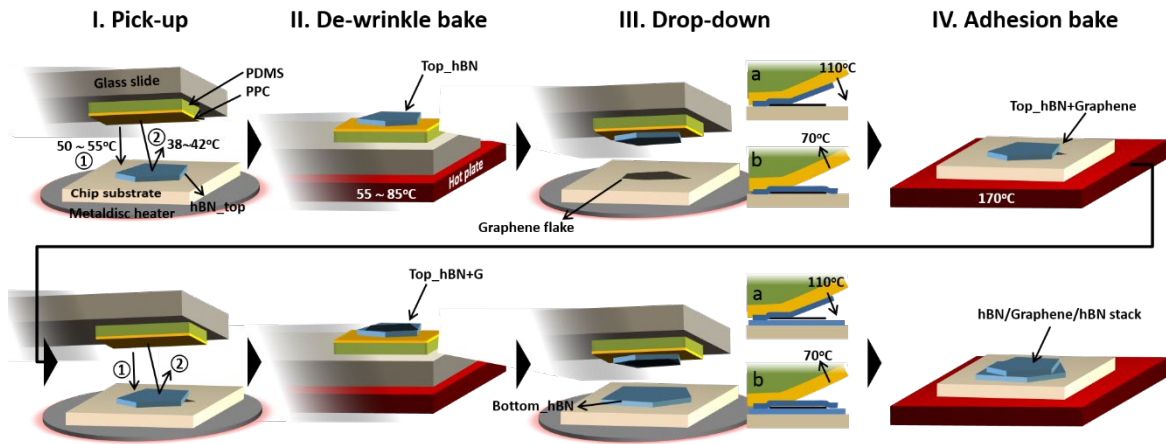


Figure 4.6 A diagram for showing the process flow of the standard hot pick-up technique referenced for an integration of hBN/graphene/hBN stack, including: I. Pick-up, II. De-wrinkle bake, III. Drop-down and IV. Adhesion bake. Figure produced by courtesy of Lene Gammelgaard.

- I. Pick-up. To pick up the hBN flake from the chip, the temperature must be set at approximately 50~55 °C which is above the glass transition temperature (T_g , approximately 40 °C) of PPC. Since the heat energy causes the PPC molecules to move around, the original rigid, glassy state of PPC will transform into a pliable, rubbery state. When the temperature reaches 50~55 °C, PPC is compliant enough to cast to the hBN flake. The manipulator must then be carefully screwed down while the angle of the PPC/PDMS stamp is adjusted. It must be ensured that the PPC can properly approach the target flake and continue until the whole flake is covered. This position must be held for a few minutes for a better moulding process. The target flake can be then locked out and then moulded into the polymer by cooling down the system until around T_g (38–42 °C). Last, a quick upward movement is needed to help the stamp rip off the hBN flake from the substrate.

Notes to I Pick-up:

- a. Try to avoid using the central area of the PPC/PDMS stamp, since it may make the subsequent alignment (when dropping down the hBN flake onto graphene) become more difficult;
 - b. When the stamp starts approaching the hBN flake, a tilted approaching is recommended rather than a directly vertical approaching;
 - c. Sometimes a failed flake pick-up occurs. Possible reasons include: (i) the hBN flake top surface is heavily contaminated (this can be addressed by rising in a warm acetone); (ii) the PPC surface may also be contaminated or corrugated during the preparation; (iii) incomplete contact between the PPC and the flake, which can be improved by slowing down the approaching speed.
- II. De-wrinkle bake. During the cooling down, PPC cures back into a rigid and glassy state; the uneven deactivating process of the polymer groups in PPC might give

rise to wrinkles on the attached hBN flake. Additionally, the pick-up step may also generate wrinkles. Luckily, most of these wrinkles can be remedied or removed to create an even flake by an appropriately soft de-wrinkle baking. The de-wrinkle baking temperature is in a wide range from 50–85 °C, which is dependent on the flake thickness. A microscope system is recommended to help monitor the de-wrinkle process and is combined with gently elevating the baking temperature.

Notes to II De-wrinkle bake:

- a. Attention should be given to the de-wrinkling process as the temperature is increased. Once it is over the ideal temperature point, the flake will instead fold together, and this is unlikely to be remedied;
- b. Extra attention is needed on the corner or edge of the flake during the de-wrinkling bake. Baking is essentially used to transform the PPC from being rigid to being pliable, which makes the flake fit better into the stamp. Since the PPC molecule grouped in different regions gain different amounts of heat energy, the energy discrepancy may easily induce new wrinkles or folds, especially at the corner or edge of the flake.

- III. Drop-down. The hBN flake, which is used as the top layer of the stack, is attached on the PPC. Before detaching the flake on graphene, the system should be heated up to 110 °C to ensure: (1) evaporation of the volatile contaminants on the surface of the flake, i.e. water or hydrocarbons; (2) transformation of the PPC into a fluidic state so that it is ready for the hBN flake releasing. The top hBN must be aligned with the target graphene flake before elevating the temperature, and the stamp must be kept close but should not contact the chip. Since the PPC becomes fluidic at such a high temperature, it is necessary to continually and carefully align the position while moving the stamp downward. Before the hBN starts approaching the graphene, the stamp must be gently tilted so that the hBN can approach the graphene from one side or corner. Slowly move until the hBN fully rests on the graphene. Keep the approaching layer still for a few minutes, then decrease the temperature to 70 °C, which detaches the hBN flake from the PPC. The glass slide can then be gently lifted away from the hBN-graphene half stack.

Notes to III Drop-down:

- a. Slightly tilt (usually at an angle of $\sim 5^\circ$) the glass slide so that the stamp bevel approaches the graphene (as illustrated in **Figure 4.6** in the drop-down step). In this way, the absorbed or attached contamination on the surface is released at the elevated temperature during the drop down, as shown in **Figure 4.7 (a)** and **(b)**. **Figure 4.7 (a)** is a bright-field OM image where the accumulated contamination at the edge of graphene can be clearly seen, as indicated with a white arrow. **Figure 4.7 (b)** is a dark-field OM image of the half stack with a better highlight;
- b. A slow and careful approach between the PPC-hBN and the graphene is highly suggested for a bubble-free integration. The area indicated by a green arrow in **Figure 4.7 (a)** and **(b)** is clear and free of bubbles, and **(c)** shows an OM image of a half stack assembled with a hasty drop-down, where many bubbles are present.

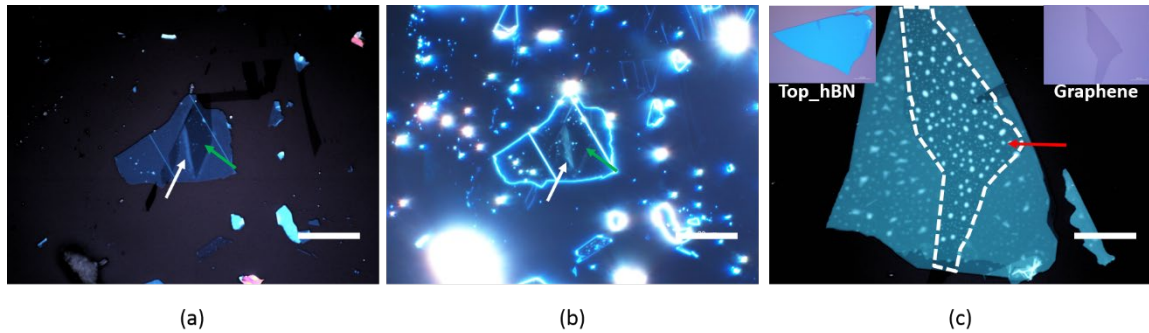


Figure 4.7 OM images of the hBN/graphene/hBN stack assembly. (a) is a contrast of the OM image and (b) is the dark-field OM image for demonstrating a slowly hBN drop-down which successfully released the contamination (indicated by the white arrow) as well as a bubble-free integration (indicated by the green arrow); (c) By adjusting the contrast among the presented materials, bubbles can be observed, it is noted that bubbles always accompany with a hasty drop-down. Scale bars are 20 μm .

- IV. Adhesion bake. The hBN provides a better vdW interaction than SiO_2 with graphene [58], [86], [126], but since graphene is conformally adhered on a plasma-treated corrugated SiO_2/Si substrate, the flat hBN flake could not contact the graphene perfectly. Additionally, plasma treatment causes an increased adhesion between graphene and the substrate[60]; the adhesion bake here is applied to achieve a better contact between hBN and graphene. However, it is can also be employed to remove the interlayer (hBN-graphene) trapped bubbles /adsorbates[86], [127]. A temperature of 170 $^\circ\text{C}$ is used during baking for approximately half an hour; this is followed by an acetone cleaning procedure to remove the polymer residuals.

Repeating the above steps results in the complete integration of the remaining layers for a full hBN/graphene/hBN stack, as shown in **Figure 4.8**. Increasing the contrast in an OM image is an efficient way of checking the final stack; see **Figure 4.8 (d)**; a distinct contrast difference between top hBN and graphene is clearly seen.

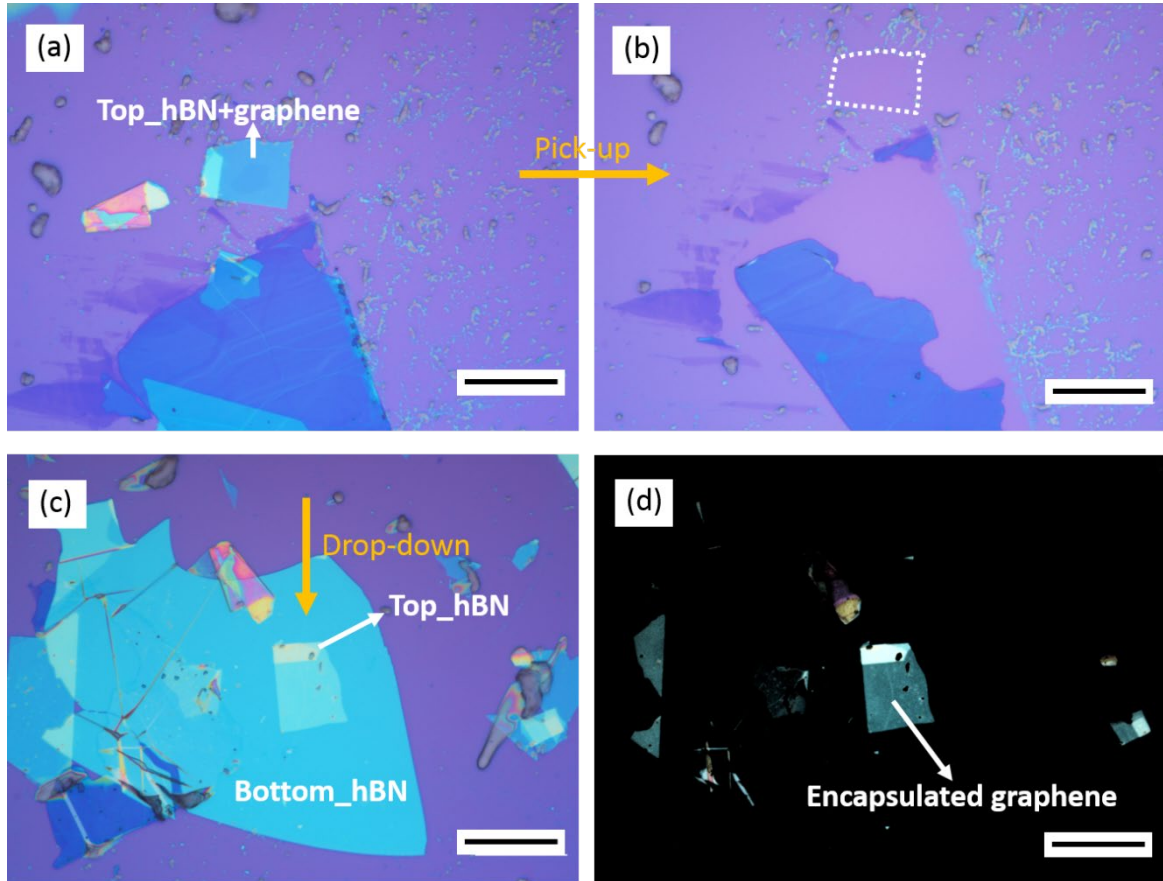


Figure 4.8 OM images representing the integration between the hBN/graphene and bottom_hBN layers. (a) An OM image of the hBN/graphene layer after the adhesion bake; (b) substrate after a successful pick-up of the half stack; the initial position of the half stack is outlined with a white dashed line; (c)(d) are OM images of the final hBN/graphene/hBN stack. Scale bars are 20 μm .

4.3.3 Modified Hot Pick-up Technique for Thin hBN/graphene/hBN Stacks

Thin hBN/graphene/hBN stacks³ are necessary considering KPFM as a surface characterization technique. However, the standard stack assembly is no longer suitable for this. As discussed in the standard stacking process, temperature plays a key role in the hot pick-up technique; it is used to control the viscosity of the PPC as well as the adhesion between the hBN and graphene. A modified hot pick-up assembly procedure specially for thin hBN/graphene/hBN stacks has been developed after many attempts, and is introduced in the following:

³ In this thesis, thin hBN/graphene/hBN stacks are referring a stack with a thin top hBN layer which is with a thickness of ≤ 15 nm.

- I. Pick-up: Instead of the usual 55 °C, a higher temperature 65 °C is applied here to make the PPC a bit more fluidic, so that a better moulding is achieved for thin hBN flakes. The ideal temperature for picking up layers is between 40~42 °C. If the pick-up is performed below that temperature, for instance 38 °C, the adhesion between the PPC and the thin hBN flake decreases dramatically. Further checks on the status (winkles, folds or breakages) of the attached flake are imperative due to a higher incidence of these imperfections in a very thin flake.
- II. Low temperature de-wrinkle bake: Since the hBN layer is thin (≤ 15 nm), folds and/or wrinkles are more likely to occur, as shown in **Figure 4.9 (a)**. Generally, for a thick hBN flake, a temperature of 110 °C is recommended, but for a thin hBN layer, this should be no more than 70 °C. Based on my experience with stacking thin hBN flakes (< 15 nm) in this work, 55-60 °C works well for flattening the wrinkles in these flakes, as shown in **Figure 4.9 (b) and (c)**. The wrinkles and folds start appearing when temperatures exceed 70°C.

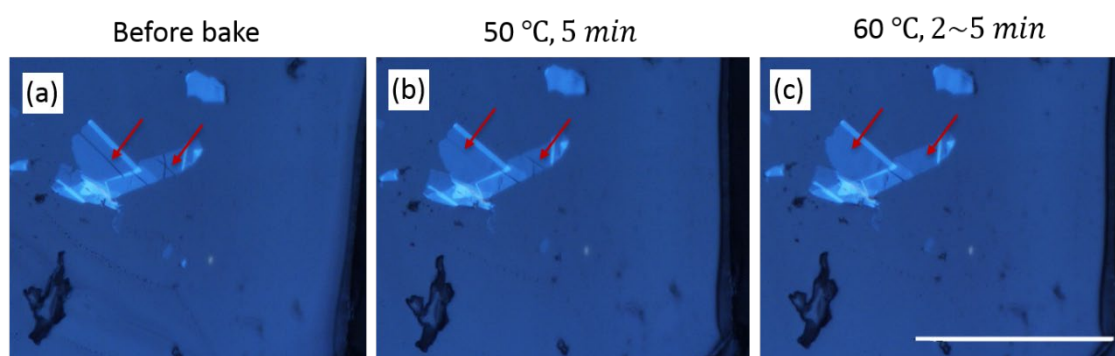


Figure 4.9 De-wrinkle baking for the thin stacking process, wrinkles are gradually flattened during the properly baking. The scale bar here is 100 μ m.

- I. Drop-down: After aligning the hBN with the target graphene flake, a temperature of 60~65°C is used for heating rather than 110 °C in the standard assembly (65°C is the most often used temperature for this step in this work). When the hBN layer is fully contacted with graphene, a temperature of 90 °C is elevated to detach the hBN flake from the stamp. The glass slide must be lifted slowly and carefully, especially when the separation comes in the proximity of the hBN/graphene half stack. Finally, the glass slide must be laterally withdrawn once the PPC completely leaves the chip.
- II. Adhesion bake: The same as the standard procedure.

When the assembly process is finished, an acetone cleaning is usually performed to remove the assembly-induced contaminations on the top hBN, such as polymer or tape residuals. The chip should be rinsed in warm (~ 50 °C) acetone and the cleaning should be

verified with OM. Now the assembled hBN/graphene/hBN stacks should be ready for further device fabrication.

4.4 Device Fabrication

4.4.1 Electron Beam Lithography

Electron beam lithography (EBL) has been widely used for nanostructure device creation because (1) by properly choosing the e-beam resist, an exposed spot of a size below 10 nm is possible, and (2) the pattern from a suitable layout software can be directly written rather than using a physical mask. In this work, two different EBL systems from the DTU Danchip cleanroom were employed: a 100 kV JEOL JBX-9500FS and a Raith Elphy system based on a Leo 1550 scanning electron microscope (SEM) with an acceleration voltage of 20 kV⁴. The commonly-used positive tone resist polymethyl methacrylate (PMMA) was chosen for all the e-beam exposures in this thesis. Two different solutions of 996K PMMA dissolved in a casting solvent, Anisole, are employed for the two different types of devices: a 6 wt% solution for HMDS rendered SiO₂/Si substrate considering the hydrophobicity, and a 4 wt% for the initial SiO₂/Si substrate. The PMMA resist is spun onto the chip at a speed of 2000 rpm with an acceleration of 500 rpm in 1 min; the eventual thickness is between 180 nm – 240 nm. A typically weak developer for PMMA, such as a mixture of IPA and MIBK, or IPA and H₂O, or ethanol and H₂O with a ratio of 3:1[128] was used here.

4.4.2 Device Fabrication Process Flow

A standard EBL process flow for graphene-based electrical device fabrication usually includes: sample preparation, spin-coating of the resist, e-beam exposure, development, etching of the graphene, resist stripping, resist re-spin-coating, e-beam exposure, metallization, and metal lift-off.

Since the adhesion between graphene and HMDS is not strong enough, the patterned graphene flake is likely to be flushed away in the “resist strip” with acetone if it is first patterned with e-beam lithography. Hence, the metal contacts are made on the graphene to ensure that the graphene constriction can be completely reserved. The process flow is depicted in **Figure 4.10**. **Figure 4.11** illustrates the standard process flow for the device fabrication of an hBN/graphene/hBN stack. Details of each step will be introduced and discussed in the following.

⁴ In this work, Raith-Leo EBL is mainly used for the device fabrication of graphene deposited on HMDS rendered SiO₂/Si substrate, while JEOL JBX-9500FS is employed for hBN/graphene/hBN stack device fabrication.

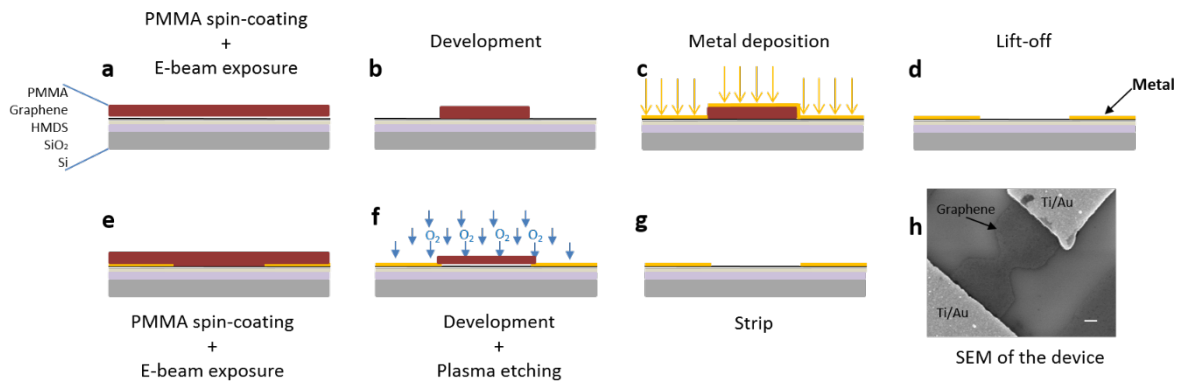


Figure 4.10 A schematic of the EBL process flow (a-g) of graphene supported with HMDS-rendered SiO₂/Si substrate; (h) A scanning electron microscopy image of the final HMDS-supported graphene device; the scale bar is 200 nm.

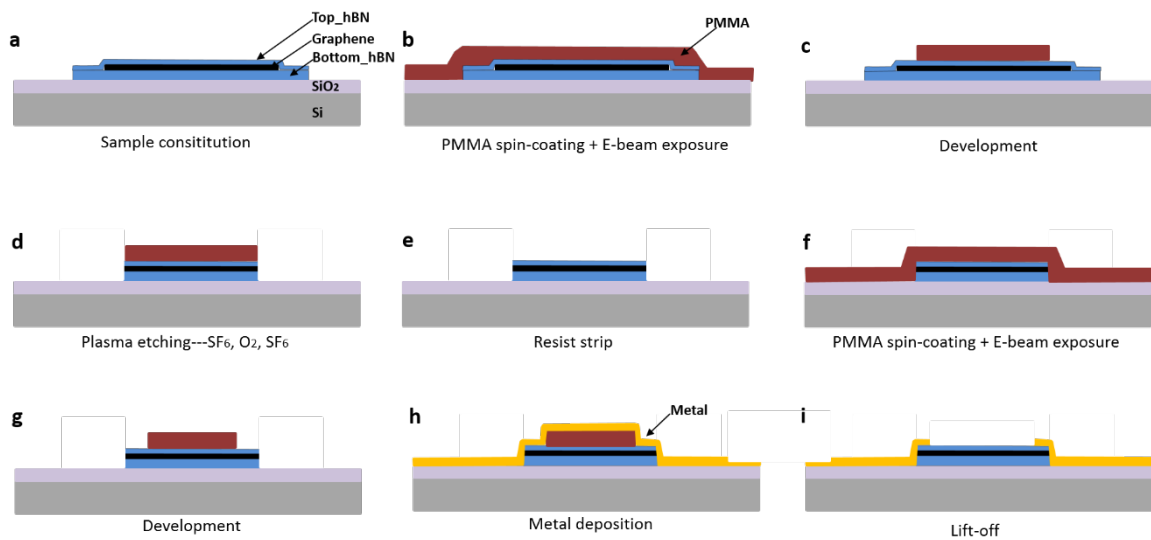


Figure 4.11 A schematic of the EBL process flow with respect to the device fabrication of the hBN encapsulated graphene. Figure produced by courtesy of Lene Gammelgaard.

Sample Exfoliation

Specific experimental details have been declared in preceding sections ([Section 4.1](#), [4.2](#) and [4.3](#)).

E-beam Resist Spin-coated

The parameters and details with respect to the EBL process flows of both the HMDS-supported graphene and encapsulated graphene are described in **Table 4.1**. Since the samples are around moist ambient air, a thin layer of water molecules will be attached to the chip surface. Given the hydrophobicity of PMMA, a pre-bake should be applied before

the PMMA is spun onto the chip. OM imaging is suggested for checking the evenness of the film after the spin-coating.

Development

Since the metal deposition is shifted ahead in the case of device fabrication on HMDS-supported graphene, the considerable thickness difference between graphene and metal might induce an uneven exposure for patterning the constriction structure, as shown in the dark-field OM images of the constriction structure in **Figure 4.12 (c-d)**. The contrast difference (that can be clearly seen in **(e)**) implies that the PMMA accumulated around the metal tip. A decent exposure of the constriction structure should be as shown in **(a)** and **(b)** in **Figure 4.14**.

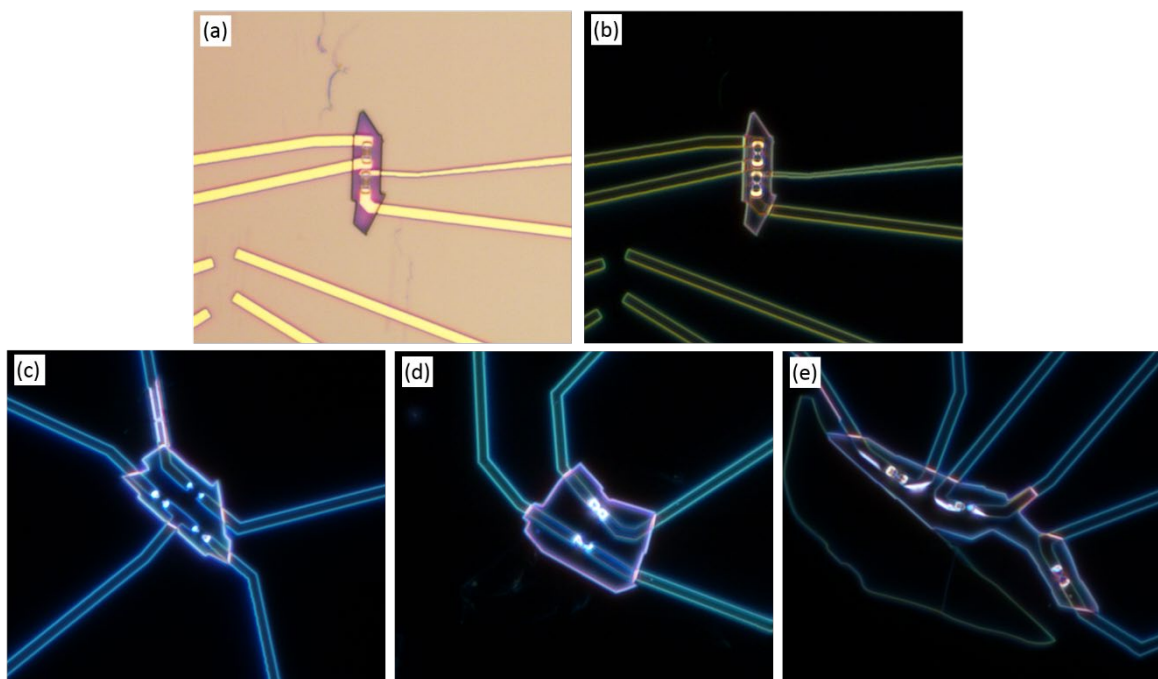


Figure 4.12 Bright-field and dark-field OM images for checking the constriction exposure of HMDS-supported graphene samples.

Etching

The etching of lithographically patterned graphene plays a key role in the performance of graphene electronics[93], [129]. The experimental etching process will unavoidably implant disorder at the edge of the graphene. A Plasma etching technique has been widely used for lithographically patterned graphene. It can be performed using either a Plasma Asher (PA) or a reactive ion etching (RIE) chamber. Oxygen is used in both systems, but a physical and direct etching process occurs in plasma RIE etching, while a less controllable and more invasive chemical etching process occurs in PA etching[129]. PA etching outputs highly-disordered graphene boundaries. Referring to the previous work[16], an edge roughness of ≤ 1 nm is expected from plasma RIE etching, and a

rougher edge from PA etching (based on the AFM measurements, the edge roughness is about 30~50 nm). In this work, RIE etching was performed on a PRO ICP etcher from SPTS at DTU Danchip, and PA etching was performed on a LASMA ETCH Plasma Asher. Working parameters are shown in **Table 4.1**. **Figure 4.13 (a)** and **(d)** display the AFM topographic images of the RIE-etched and PA-etched graphene nanoconstrictions. And the height line profiles (**Figure 4.13 (b)** and **(e)**) of the channel. Moreover, from the height line profile of the cross section at the edge, the RIE etching induces a roughness spanning a range of about 30 nm at the edge. However, it is much larger in the PA-etched edge which spans around 200 nm ((see **Figure 4.15 (c)** and **(f)**).

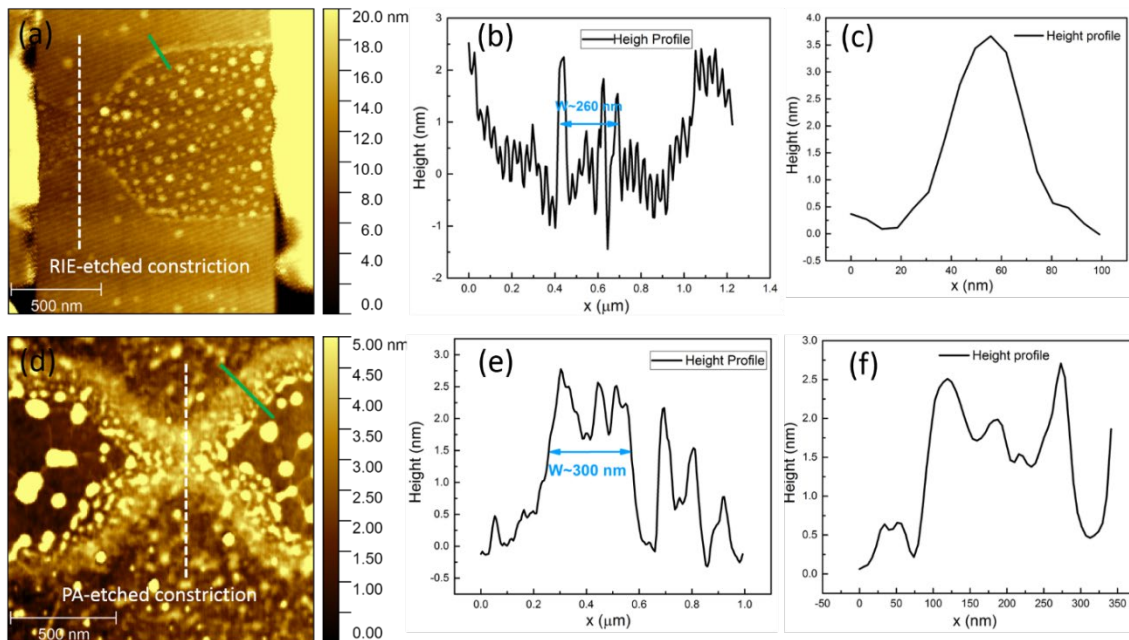


Figure 4.13 Comparison between the RIE-etched graphene constriction and the PA-etched constriction: (a) and (d) AFM topographic images of the individual etched constrictions; (b) and (e) height profiles of the dashed white lines and the width of the channel are obtained; (c) and (f) are the height profiles of the solid green lines across the edge.

Apart from its use in the etching of graphene in HMDS-supported graphene device fabrication, hBN is also needed for etching in the hBN/graphene/hBN stack, which is performed with SF_6 . A schematic of the stack etching process has been demonstrated in **Figure 4.14**. By adjusting the running power and pressure of the plasma RIE, the etching rate of the hBN layer can be controlled. **Table 4.1** displays the experimental parameters for etching a normal hBN/graphene/hBN stack. Considering the substrate effects from SiO_2 , only the top hBN and graphene layers were etched in the thin stacks employed for KPFM measurements; the bottom hBN layer was therefore kept to minimize the substrate effects.

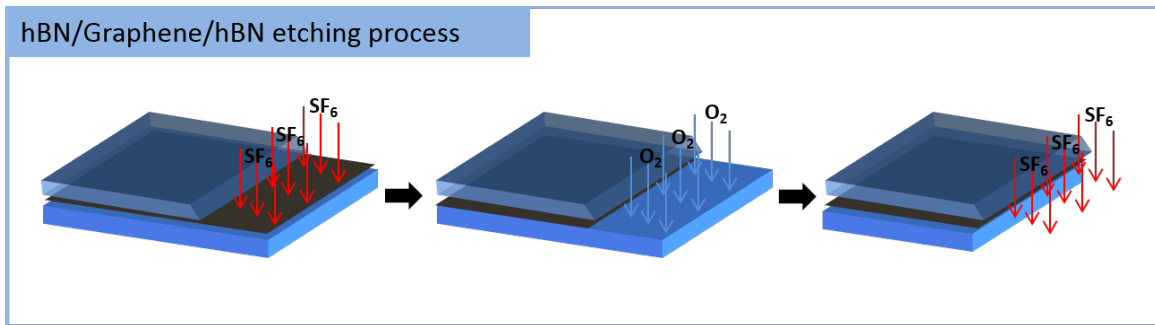


Figure 4.14 A schematic depicting the etching process flow for a hBN/graphene/hBN vdW device.

Metallisation

Metal deposition comprising 15 nm Ti and 15 nm Au is performed in a Physimeca SES250 electron-beam evaporation system at DTU Danchip. The deposition was processed at a low pressure below 2×10^{-7} mbar, and the individual depositing rates for Ti and Au were 1 Å/s and 3 Å/s. Such a metal composition is typical of HMDS-supported graphene devices.

Another metal composition of Cr and Au, which is used for hBN encapsulated graphene devices, was performed using the E-beam Evaporator Temescal from DTU Danchip. The base pressure of the chamber can be as low as 1E-8 Torr after overnight pumping, which is helpful for achieving a denser metal contact and higher quality. The operating parameters are listed in **Table 4.1**.

Lift-off

Metal lift-off is achieved by soaking the chip in acetone and is performed in the fume hood. **Figure 4.17** provides a final look of the device.

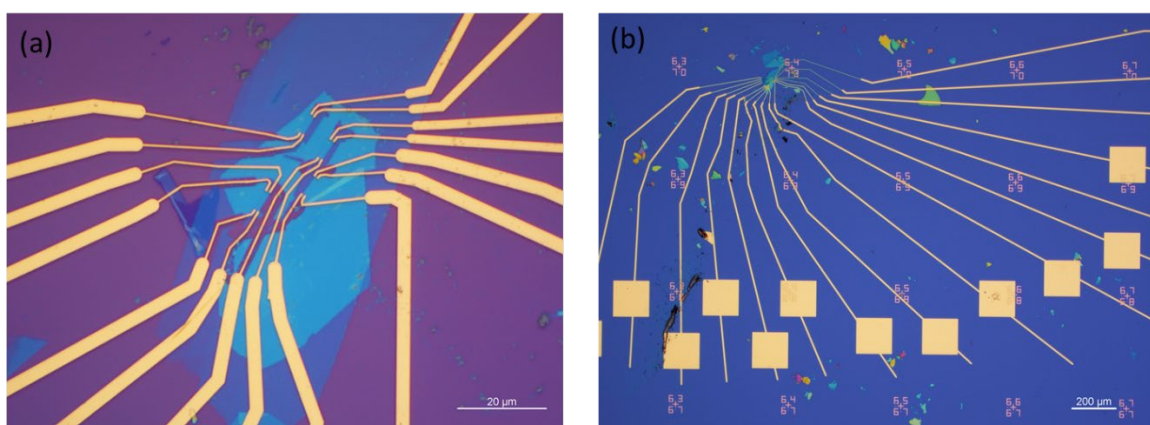
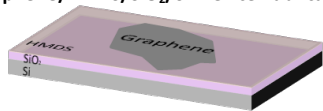
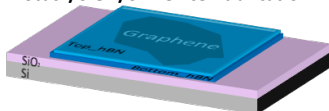


Figure 4.17 OM images of an accomplished hBN/graphene/hBN device using (a) a 100x objective, and (b) a 5x objective.

Sample Preparation and Fabrication

Graphene/HMDS/SiO ₂ /Si Device Fabrication		Stack/SiO ₂ /Si Device Fabrication	
			
Step	Detail and Parameters	Step	Detail and Parameters
Sample constitution	A thin and uniform HMDS priming applied on SiO ₂ /Si: HMDS:Acetone = 1:1, dip chips inside and keep still for 14-16h; Graphene mechanically exfoliated on the HMDS rendered substrate: 70°C, 10 min heating before remove the tape;	Sample constitution	Mechanically exfoliated both hBN and graphene from bulk crystal; Follow the given hBN/Graphene/hBN stack assembly procedures; Use acetone to remove the polymer residuals before the forward device E-beam involved fabrication;
Spin-coating	Pre-bake @ 180°C for 5-10 min; 6 wt% PMMA in Anisole spin-coated in a speed of 2000 rpm, 1 min, with an acceleration of 500 rpm. Pos-bake @ 180°C for 2min; OM check:	Spin-coating	Pre-bake @ 180°C for 5-10 min; 4 wt% PMMA in Anisole spin-coated in a speed of 2000 rpm, 1 min, with an acceleration of 500 rpm. Pos-bake @ 180°C for 2min; OM check:
E-beam exposure	EBL system: Raith Elphy-Leo Acceleration voltage: 20 kV Aperture: 60 μm for the metal leads/pads; Current: 18 ~22 pA; Dose: 260~280 $\mu\text{C}/\text{cm}^2$;	E-beam exposure	EBL system: JEOL JBX-9500FS Current: 6 nA Dose: 800-1000 $\mu\text{C}/\text{cm}^2$;
Development	Prepare the developer: IPA: H ₂ O=3:1; Dip the chip inside and slightly swing for 1min; Re-rinse in IPA 15s; N ₂ gun blow it dry;	Development	Prepare the developer: IPA: H ₂ O=3:1; Dip the chip inside and slightly swing for 1min; Re-rinse in IPA 15s; N ₂ gun blow it dry;
Metal Deposition	15 nm Ti/15 nm Au Rate of Ti deposition: 1 \AA /s Rate of Au deposition: 3 \AA /s (Physimeca in Danchip)	Plasma Etching	20 min O ₂ chamber cleaning; PMMA Descum with O ₂ /Ar for 5 s; Top_hBN: 5 s of SF ₆ for thin hBN flake, 15~20 s SF ₆ for standard hBN flake. Graphene: 10 s of O ₂ , 15~20 s for standard stack etching; Bottom_hBN: skipped for thin stack (partly etching), 15~20 s SF ₆ for standard hBN flake.
Lift-off	Use the tweezer tip carefully scratch a square along the chip edges, then soak the chip in Acetone or warm (50°C) Acetone until the surface become corrugated, then use a pipette gently spray the acetone at the wrinkle metal to speed up the lift-off process.	Resist strip	Rinse the chip in Acetone until the resist completely dissolved, then IPA rinsing, subsequently N ₂ blow dry.
Re-Spin-coating	Pre-bake @ 180°C for 5-10 min; 6 wt% PMMA in anisole spin-coated in a speed of 2000 rpm, 1 min, with an acceleration of 500 rpm. Pos-bake @ 180°C for 2min; OM check:	Re-Spin-coating	Pre-bake @ 180°C for 5-10 min; 6 wt% PMMA in anisole spin-coated in a speed of 2000 rpm, 1 min, with an acceleration of 500 rpm. Pos-bake @ 180°C for 2min; OM check:
E-beam exposure	EBL system: Raith Elphy-Leo Acceleration voltage: 20 kV Aperture: 10 μm for the channel; Current: 18 ~22 pA; Dose: 260~280 $\mu\text{C}/\text{cm}^2$;	E-beam exposure	EBL system: JEOL JBX-9500FS Condition file: 6 nA_ap6; Dose: 800-1000 $\mu\text{C}/\text{cm}^2$;
Development	Prepare the developer: IPA: H ₂ O=3:1; Dip the chip inside and slightly swing for 1min; Re-rinse in IPA 15s; N ₂ gun blow it dry;	Development	Prepare the developer: IPA: H ₂ O=3:1; Dip the chip inside and slightly swing for 1min; Re-rinse in IPA 15s; N ₂ gun blow it dry;
Plasma Etching	III-V ICP etching:	Metal deposition	5nm Cr/45 nm Au Rate of Cr deposition: 1 \AA /s

	coil/platten power 20 W, Ar 15 sccm, O ₂ 5 sccm, etching time 12 s; PA etching: RF power 40%, vacuum pressure 400 mTorr, etching time: 5s.		Rate of Au deposition: 3Å/s (Temescal in Danchip)
Resist strip	Rinse the chip in Acetone until the resist completely dissolved, then IPA rinsing, subsequently N ₂ blow dry.	Lift-off	Use the tweezer tip carefully scratch a square along the chip edges, then soak the chip in Acetone or warm (50°C) Acetone until the surface become corrugated, then use a pipette gently spray the acetone at the wrinkle metal to speed up the lift-off process.
* All the parameters settings related to the machines employed at DTU			

Table 4.1 Details and parameters with respect to each step of EBL process flow of two different sample in this work: HMDS-supported graphene device and encapsulated graphene device.

5 Gate Electrostatics in Graphene Nanoconstrictions

Key words: Edge disorder in narrow graphene device; Gate electrostatics, KPFM; Charge accumulation;

5.1	Electrostatic Potential Measurements in Gated Graphene Devices.....	49
5.2	Gate Electrostatics in HMDS-supported Open Graphene Nanoconstrictions.....	51
5.2.1	Experimental setup.....	51
5.2.2	Results and Discussion.....	52
5.2.3	Concluding Remarks	60
5.3	Charge Distribution in Semi-etched Encapsulated Graphene Nanoconstrictions	61
5.3.1	Sample Preparation and Experimental Setups.....	61
5.3.2	KPFM Results and Discussion	63
5.3.3	Concluding Remarks	78
5.4	Summary.....	78

5.1 Electrostatic Potential Measurements in Gated Graphene Devices

As we discussed in [Chapter 2](#) and [Chapter 3](#), given the exceptional spatial resolution, KPFM is capable of characterizing the surface potential distribution of the narrow graphene electronic devices. Ideally, the contact potential difference between the tip and the sample should equal to the applied bias. However, due to the long-range nature of the electrostatic force, F_{el} , a capacitive coupling effect generated between the conducting cantilever assembly and the sample (including the metal electrodes) needs to be taken into account[130]–[138]. E. J. Fuller et al.[134] demonstrated that the KPFM-imaged surface potential, Φ_{KP} , is a weighted sum of all potentials V_i on the scanned surface (see **Figure 5.1 (a)**). Similarly, the Φ_{KP} of the gated graphene devices can be approximately given as $\Phi_{KP} \approx \alpha_{gate}V_g + \alpha_{graphene} \frac{U(x)}{e}$, as indicated in **Figure 5.1 (b)**. In ideal cases, the coupling effects of the measuring probe is insensitive to the tip oscillation during the scanning, so that the coupling coefficient of the metallic gate, α_{gate} , equals 1 for the area outside the device and it equals 0 on the graphene device. Consistently, the coupling coefficient of the graphene, $\alpha_{graphene}=1$, satisfies over all the graphene device while it is 0 for the area beyond the graphene plane (see **Figure 5.2**). The local potential distributions over all the sample with respect to the graphene, the perfect metal and the KPFM are shown in **Figure 5.2**.

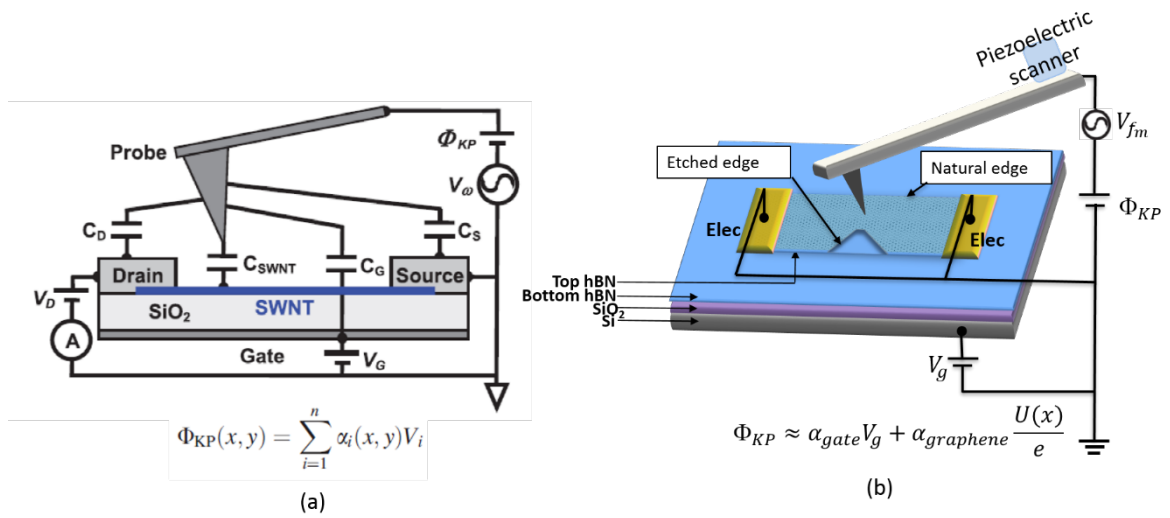


Figure 5.1 (a) Schematic of the KPFM and the coupling effects of the measuring probe to the distant surfaces, adapted from [134]. (b) With respect to one of the investigated gated graphene devices in this work, the KPFM-imaged surface potential is approximately the weighted sum of the coupling of the probe to the device and the metallic gate.

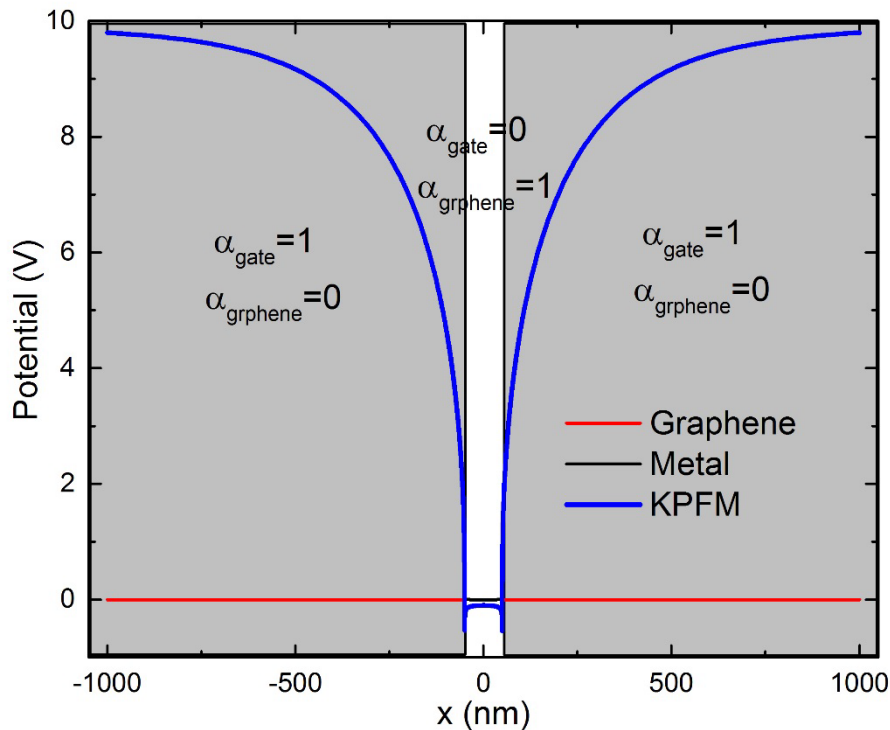


Figure 5.2 The electrostatic potential profile of the gated graphene from KPFM in the ideal cases (solid blue line), the solid red line is the graphene-specific potential profile with respect to the gated graphene nanostrip, the solid black line is corresponding to the potential distribution of a perfect metal. The applied gate bias is +10 V.

In this chapter, two different device architectures, including open graphene supported by HMDS-rendered SiO₂/Si and hBN encapsulated graphene on SiO₂/Si, were investigated. The graphene flakes were shaped into a constriction using the standard EBL fabrication method. Two etching techniques (PA etching and RIE etching) enable us to obtain different roughness at the graphene edges (note that the fabrication details can be found in [Chapter 4, section 4.4](#)). The experimental setup and results are discussed in the following sections. All devices in this chapter regarding to the fabrication are proceeded using the standard E-beam lithography (EBL) on the mechanically exfoliated monolayer graphene.

5.2 Gate Electrostatics in HMDS-supported Open Graphene Nanoconstrictions

As an extension of the previous work from Jose M. Caridad[16], the HMDS-supported open graphene nanoconstrictions of different edge roughness were investigated. Details of the sample fabrication have been clarified in [Chapter 4](#).

5.2.1 Experimental setup

A schematic of the experimental setup is shown in **Figure 5.3 (a)**. Metal electrodes of 15 nm Ti / 15 nm Au were deposited on each end of the graphene constriction, and the electrodes were led out using the silver epoxy. A bond wire was used to connect the backgate to a Keithley 2280S-60-3 Digital sourcemeter for various gate voltages. Samples were mounted on an insulating holder specifically with a conductive spring clip used to fix and ground the sample (see **Figure 5.3 (b-c)**). The KPFM measurements on open graphene nanoconstrictions were conducted on a NTEGRA Aura SPM Platform from NT-MDT using the conventional dual-pass AM-KPFM operation. Doped silicon PFQNE-AL probe from Bruker with a tip radius of ~5 nm and a spring constant of 0.8 N/m were used for the electrical measurements, as shown in (**Figure 5.3 (d-e)**).

In the dual pass AM-KPFM, the topography of the graphene constriction is mapped with a tapping mode first, which is then traced at a set lift height above the sample surface imaging measurements of the surface potential. The AC bias (~2 V) was applied to the probe at the mechanical resonant frequency $f_0=300$ kHz.

All the KPFM measurements were performed in ambient air environment at room temperature.

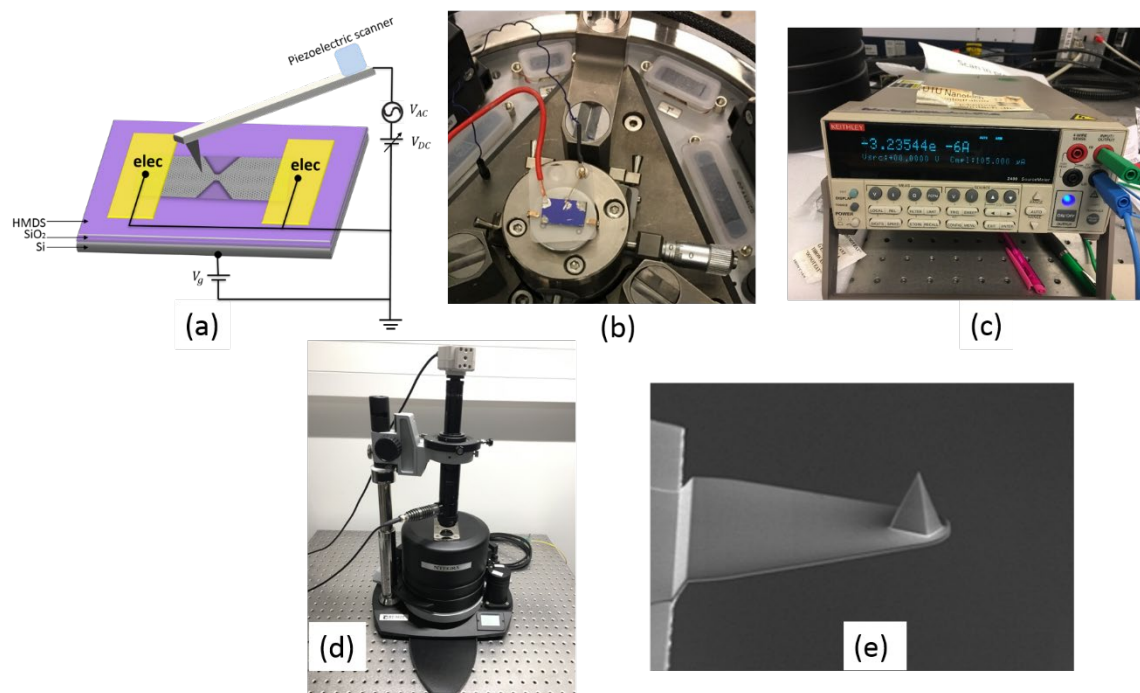


Figure 5.3 (a) Schematic diagram for performing the surface potential of open-graphene constriction on HMDS/SiO₂ using KPFM. (b) The red wire is used to lead out the back gate. The black wire is used to ground the sample by placing the spring contact on the silver which is connected to the metal electrodes of the sample. (c) The employed Keithley Digital sourcemeter outputs different gate voltages for the system. (d) The employed NTEGRA Aura SPM Platform from NT-MDT. (e) A scanning electron microscopy image of the doped silicon PFGNE-AL probe from Bruker.

5.2.2 Results and Discussion

Morphology and surface potential mapping of open graphene constriction with a lower edge disorder

KPFM measurements on the RIE-etched constrictions were performed first. As described in literature[16], an edge roughness of $\leq 1\text{nm}$ was expected using RIE, which is referred to as smooth constriction (SC). **Figure 5.4 (a)** demonstrates the global topography of the obtained graphene nanoconstrictions. The position of metal electrodes misaligned a bit during the exposure, but a clear contour of the constriction can be seen from the AFM images of the sample.

Individual topography AFM images of the smooth constriction 1 (SC1) and the smooth constriction 2 (SC2) and the corresponding width line profiles are shown in **Figure 5.4 (b-e)**. The well-constructed constrictions are clearly presented. However, excessive contaminants from the device fabrication process are also found on the graphene surface and the substrate. Width line profiles are extracted by crossing the narrowest part of the constriction. The width of SC1 is about 150 nm, and a width of ~ 260 nm is for SC2.

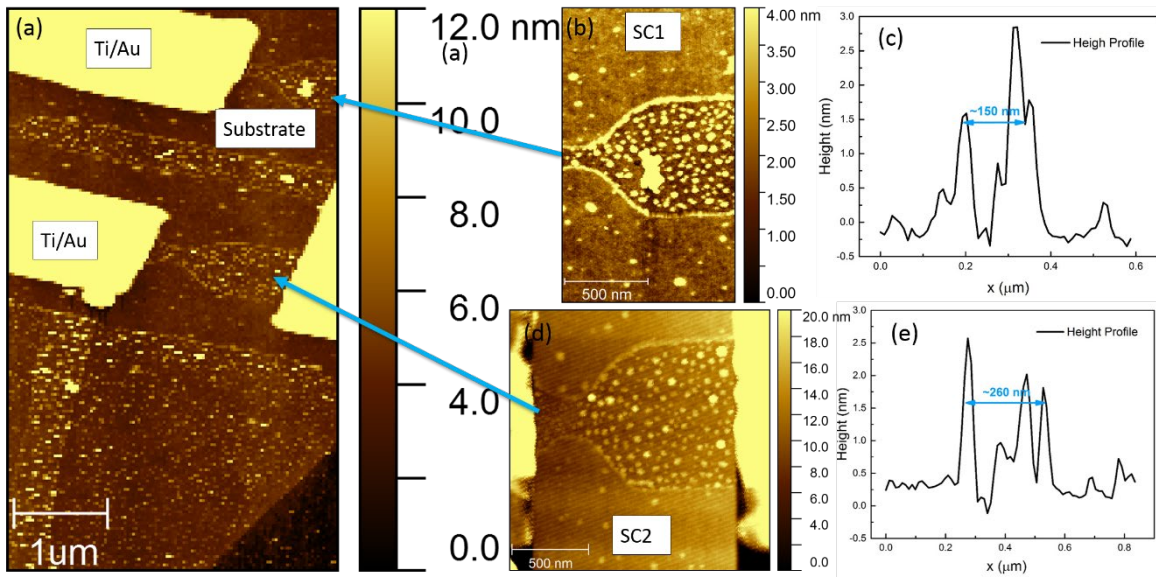


Figure 5.4 Topographic AFM images of the open graphene constriction device which is supported by HMDS-rendered SiO_2/Si substrate. (a) Topography AFM image of the smooth constrictions from an overall standpoint; (b) and (d) shows the individual AFM images of SC1 and SC2, a clear contour of constriction can be seen. The highlighted contaminates on graphene surface are possibly the polymer residuals from the device fabrication. (c) and (e) correspondingly show the width line profiles of the two smooth constrictions by crossing the narrowest part of the graphene channel.

Figure 5.5 demonstrates surface potential mappings of SC1 and SC2 at different back gate voltages. The contours of the two constrictions are clearly seen from the surface potential mappings and the rest area corresponds to the substrate. Here, it is worth pointing out that all the surface potential mappings have been rescheduled relatively to the surface potential of the insulating substrate. It is because the intrinsic potential distribution of graphene constriction varies in a big range when the gate voltage changes from -15 V to +10 V. In order to show a visible change of the contrast associated to the applied gate voltages, the surface potential of the insulating substrate was aligned and centred at 0 V using a data visualization and process tool for scanning probe microscopy. Each potential mapping shows a relative surface potential and reveals the effective injected charges from the applied electric field. Clearly, the contrast changes of the constriction imply the polarity and magnitude of the applied gate voltage.

Additionally, the charge neutral point, V_{CNP} , which indicates the voltage at which the external gate voltage balances the sum of the induced charge doping from impurities, contamination and trapped charges, can be read from the potential mappings: V_{CNP} is approximately -7.5 V for SC1, suggesting that this constriction is electron doped; SC2 is slightly electron doped with the $V_{CNP} \approx -2.5$ V.

Intrinsic data is needed for the investigations of the electrostatic potential distribution across the graphene channel, and used to verify the presence of charge accumulation at the boundaries. Potential line profiles are extracted from the narrowest portion (as the dashed line shown in **Figure 5.5 (a) and (A)**) of the constrictions and the raw data are plotted in **Figure 5.6**.

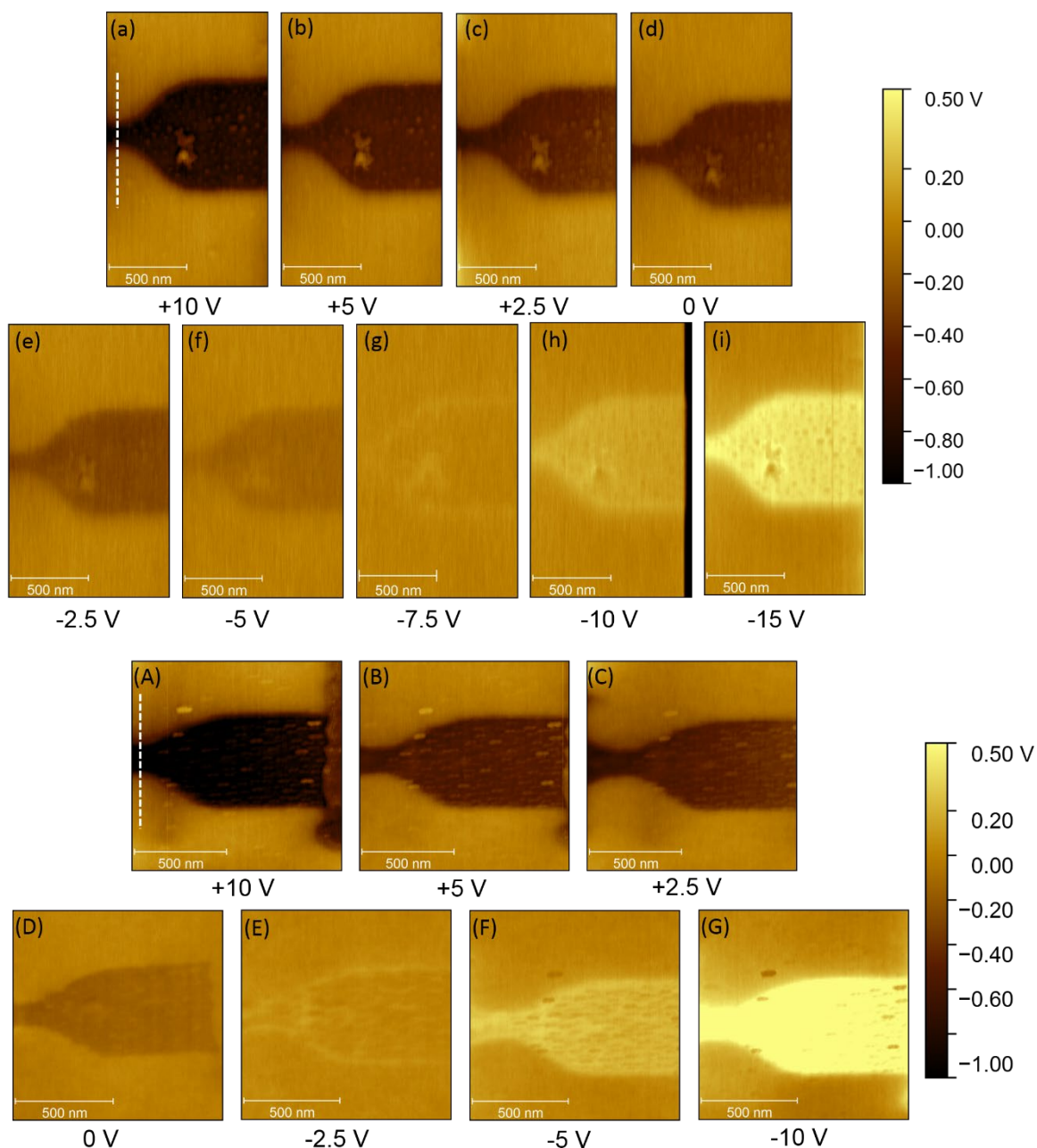


Figure 5.5 Surface potential mappings of SC1 (a-i) and SC2 (A-G) at different gate voltages are shown. The surface potential distribution with respect to the insulating substrate has been aligned and set as 0 V. The white dashed lines in (a) and (A) imply the crossing line from which the potential line profile is extracted. All the surface potential maps are represented with the same surface potential scale bar.

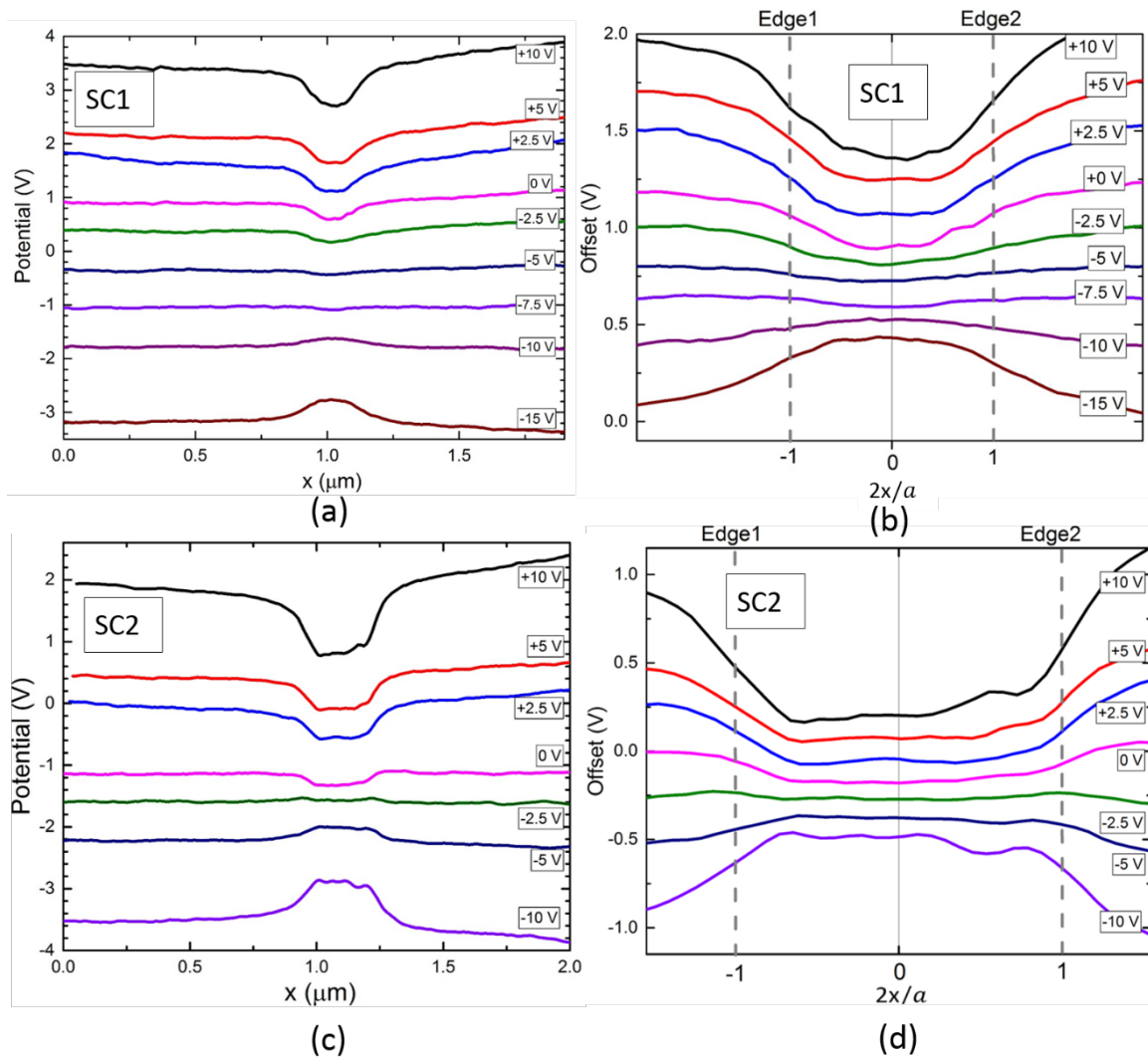


Figure 5.6 line cuts of the surface potential profile across the SC1 (a-b) and SC2 (c-d). (a) and (c) are the raw data extracted from the KPFM potential mappings, while (b) and (d) are addressed to focus the potential distribution with respect to the amplitude changes from the constriction center to the edges.

Figure 5.6 (a-b) depicts the in-plane local potential profile across the SC1, and **(c-d)** is that of SC2. The position of the constrictions can be read roughly from the different response from the graphene and the substrate to the applied V_g . Combining with channel width obtained from the topography, the graphene nanoconstriction edges are marked with the dashed lines in **(b)** and **(d)**. It is necessary to point out that one should not refer the magnitude (y-axis) of the surface potential in **(b)** and **(d)**. Because the potential line profile of each V_g has been offset to highlight the local potential distribution with respect to the graphene constriction segment. So that it is easy to compare the local potential of the

constriction center to that of the edge of each gate voltage at the same time. Knowing that the graphene-specific potential profile across the channel develops an inverted “U” shape with downturned brims at the edge (Specifically for a $V_g=+10$ V applied on an intrinsic graphene strip, see [Section 2.3, Chapter 2](#)), it can be concluded an absence of the charge accumulation from our KPFM measurements of SC1 and SC2. The fact of graphene only consists of surface atoms makes it more susceptible to be affected by the substrate beneath and environment. Besides the trapped charges in substrate, external contributions such as p-type adsorbates: water, oxygen, and hydrocarbons, are responsible for a redistribution of the charge in graphene[46], [73], [139], [140], which could be the reason for the absence of accumulation around the boundaries.

In particular, an ambipolar response to the external applied electric field is seen from the plotted surface potential (see **Figure 5.6 (a)** and **(c)**), which implies an effective tuning on the Fermi energy of graphene using the gate voltage V_g applied to the degenerately doped Si substrate. However, if fixing the gate voltage, i.e. $V_g = +10$ V, there are obvious discrepancies on the probed surface potential between SC1 and SC2 with respect to the effective tuning from the bias, which is probably related to the constriction width[10], [13], [16] and the density of the contaminants on the graphene device. Additionally, the charge neutral point of each constriction can be also obtained from the plotted line profiles which is consistent with the estimation from the potential mappings: $V_{CNP}(SC1) \approx -7.5$ V and $V_{CNP}(SC2) \approx -2.5$ V.

Morphology and surface potential mapping of open graphene constriction with a higher edge disorder

Constrictions etched by PA (Plasma Asher) discussed in the following are more complicated than the smooth constrictions etched by RIE. The planar electrostatic potential distribution of rough PA-etched graphene constrictions (which are referred to as rough constriction, RC) is severely affected by both the channel and the edge disorders.

KPFM measurements performed on RC1 and RC 2 with respect to the morphology are shown in **Figure 5.7**. Line profiles in **(b)** and **(d)** associated to the width of each constriction are extracted by crossing the waist of the constriction. A width of about 260 nm is obtained for the two rough constrictions. From the topography, the rough constrictions demonstrate noticeable roughness at the graphene boundaries (see **Figure 5.7 (a)** and **(c)**). Moreover, the visible contaminations over all the rough constrictions tend to be piled together forming into sharp islands rather than distributed flat and evenly in the smooth constrictions.

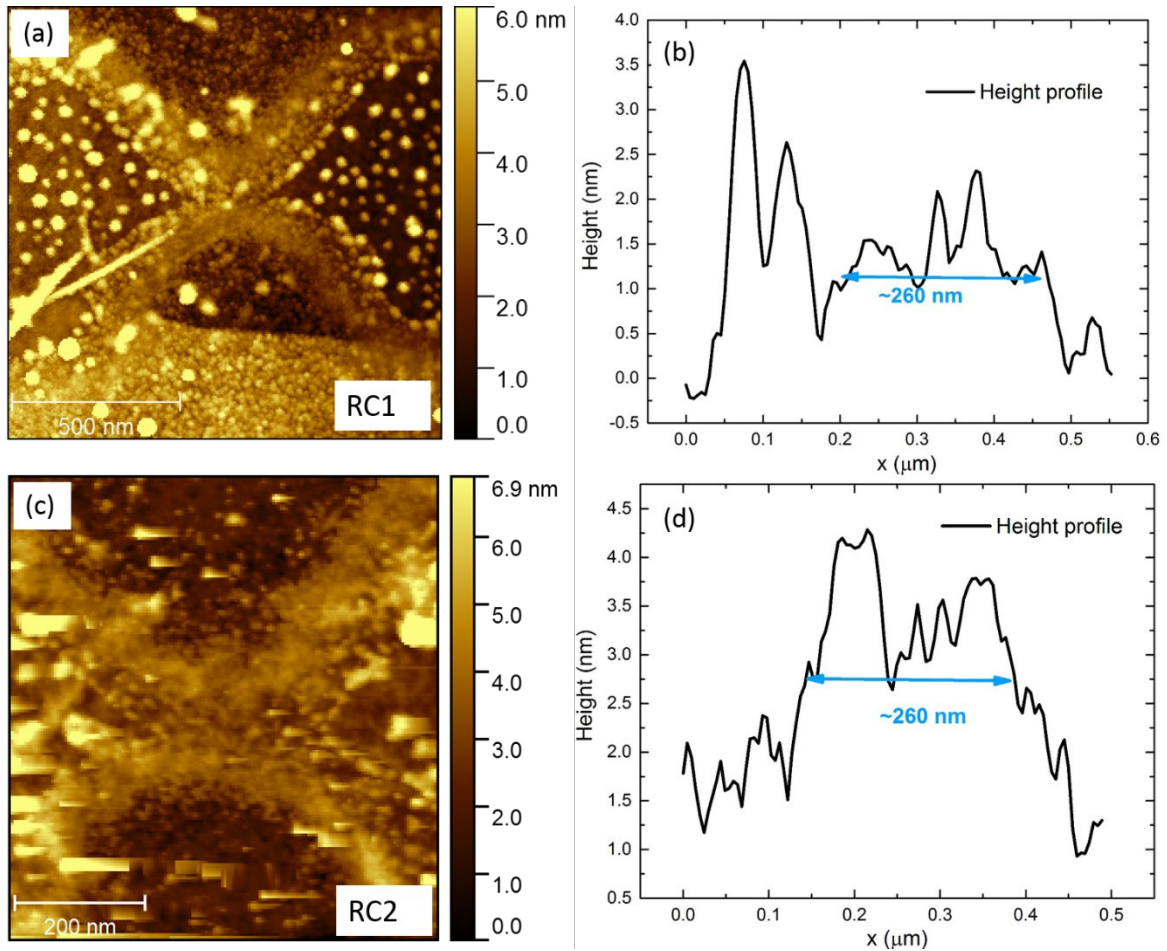


Figure 5.7 (a)(c) Topography AFM images of the rough constrictions RC1 and RC2. (b) and (d) correspondingly show the width line profiles of the two rough constrictions by crossing the narrowest part of the graphene channel.

As previously method used to address the KPFM measurements in the smooth constrictions, the line profiles of local potential distribution across the rough graphene constriction with respect to various gate voltages are shown in **Figure 5.8**. The transitional boundary from graphene to substrate is implicit relatively to the case of smooth constrictions. The position of the constriction edges are marked based on the width line profile. The charge neutral point of RC1 and RC2 can be acquired first from potential line profiles (a) and (b), $V_{CNP}(RC1) \approx +1.5$ V and $V_{CNP}(RC2) \approx -1$ V, both seem less doped than the constrictions etched by RIE. Here, RC1 is hole doped rather than electron-doped of all other investigated constrictions. It is known that both the substrate and externally-implanted impurities contribute to the doping of graphene[58], [59], [67], [105], [139]. The lower doping level in rough constrictions is probably attributed to the instabilities in electron transport caused by the PA etching[93], [129]. Additionally, the electric response of rough constrictions to the applied electric field is not as sensitive as that of the smooth constrictions, this can be observed from the magnitude of the potential profile. Potential line profiles focusing the channel are shown in (c) and (d), besides a fact of the absence of

charge accumulation at constriction edges, the local potential varies rather small from the channel center to the edge comparing with SC2 which has the same width.

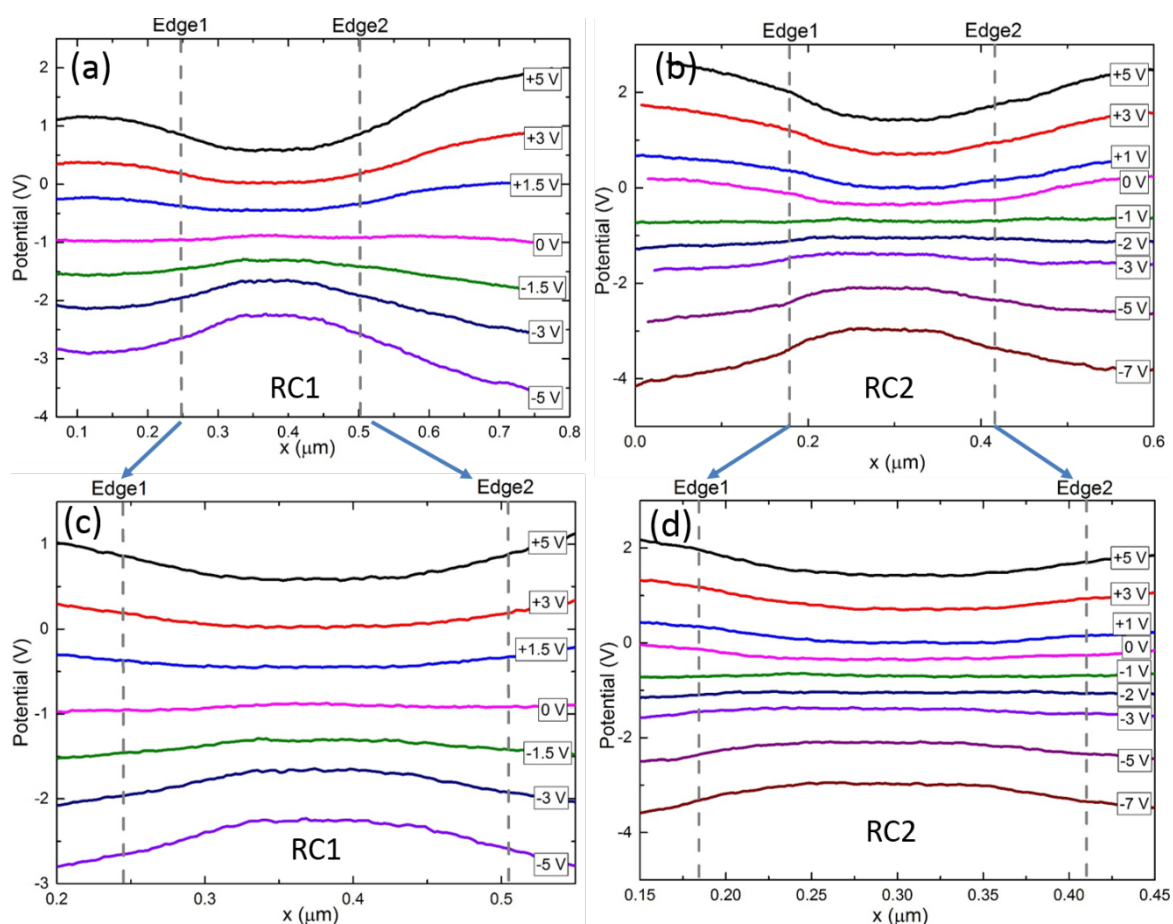


Figure 5.8 Line profiles of the probed surface potential of RC 1 and RC2 are depicted in (a) and (b) separately. (c) and (d) are the local potential distribution focusing on the device channel.

Additionally, height profile of a cut line across the constriction edge with respect to SC2 and RC1., as depicted in **Figure 5.9**, are plotted for further investigations on the magnitude of the etching-caused disorders. We found an interesting fact: Regarding to the topography of SC2, the surficial contaminates build up at the edges and construct a sharp “wall” (with a spanning length of about 30 nm) between the graphene and the substrate. However, a transition with a spanning length of ~ 200 nm blurs the boundary in RC1, and the “wall” is much shorter, see the height profiles in (c) and (d). Considering the obtained width of ~ 260 nm, the rather flat surface potential profiles of rough constrictions may attribute to an averaging effect from etching-caused disorders distributed over all the constriction channel. Moreover, external contributions from the adsorbates with respect to the presence of air and surficial contaminants from the fabrication process are also responsible for the charge distribution. Due to the complex interplay between graphene

and the adsorbates/impurities[140], it is hard to quantitatively calculate such kind of contribution.

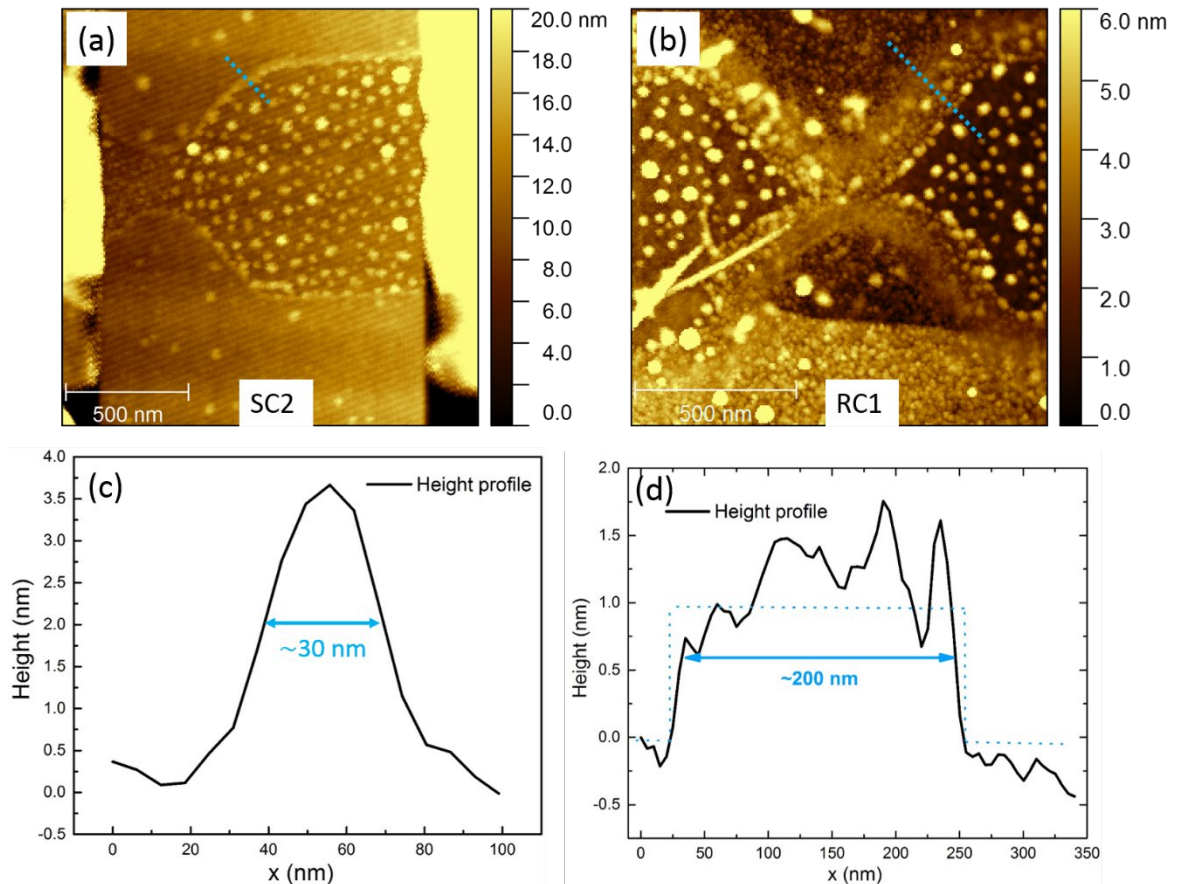


Figure 5.9 (a) and (b) are the topography AFM images of SC2 and RC1 respectively. (c) and (d) are the height profile of the dashed line which are depicted in the AFM images.

Apart from the previous discussion on the externally implanted impurities and disorders, parasitic contributions, which are induced from the long-range capacitive coupling effect generated between the conducting cantilever assembly and the sample surface, can make noticeable influences on the measured surface potential[110], [133], [136]–[138]. It is therefore KPFM measures a weighted average of the surface potential underneath the tip apex. We performed the effects of the measuring tip in a simple 2D numerical modelling using COMSOL Multiphysics. The gated graphene nanoconstrictions were addressed as a classical capacitor. The graphene constriction with a width of 300 nm was treated as a metal. The tip component was simplified using a triangle which set at a distance of 20 nm from the metal. Both metal and tip are grounded, the bias is applied on the metallic gate which is separated from the metal by 300 nm-thick SiO₂. The computed results with respect to the electrostatic potential and electric field distribution at a $V_g = +10$ V are shown in **Figure 5.10**.

The spatial distributions of both the electrostatic potential and electric field are largely affected by an implantation of the tip in the simulation. The electrostatic potential around the tip apex is reconstructed. Most of the electric field lines end on the tip rather than the graphene (the metal in the model). Therefore, we infer that the discrepancy in applied bias and measured potential can be explained by the spatial averaging of AM-KPFM due to the tip effects. It is worthy to point out that the limited spatial resolution of AM-KPFM is related the captative coupling. The size of the cantilever is considerably larger comparing with the device channel, it is hence the captative coupling between the conducting probe and the sample is unavoidable. However, the parasitic captative coupling can be decreased by performing the measurements in FM-KPFM. Since it is out of the scope of the main interest of the work, the captative coupling is briefly discussed here.

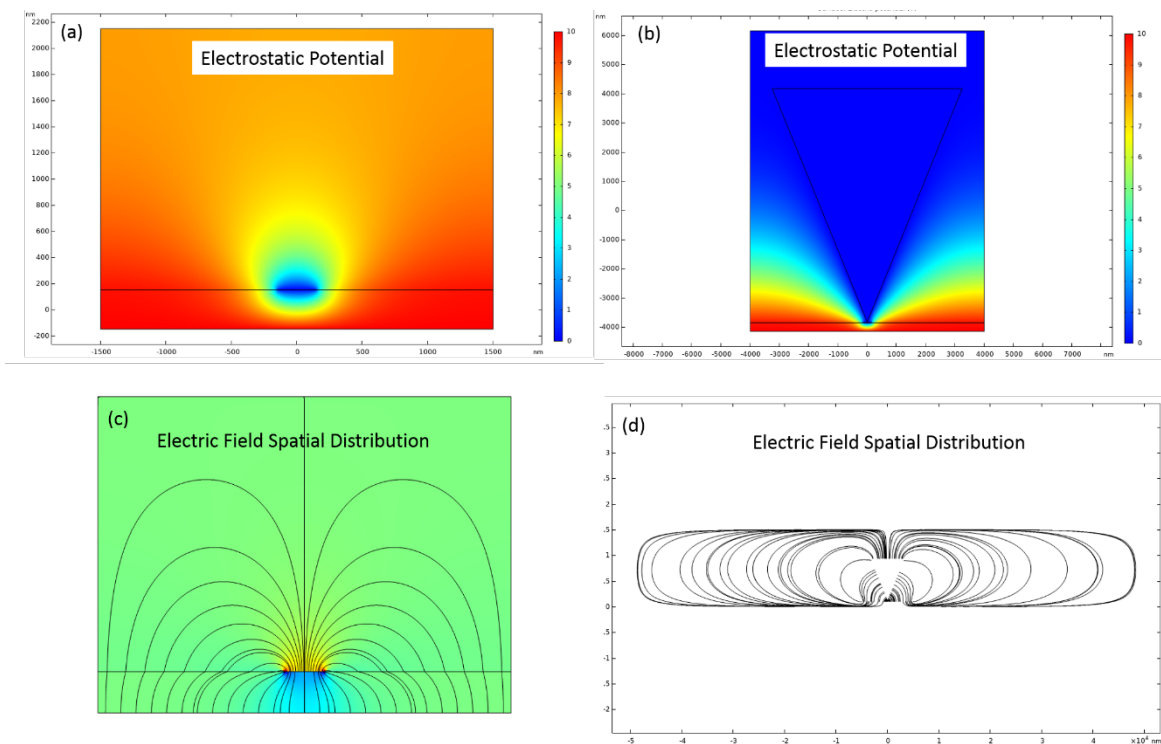


Figure 5.10 The computed electrostatic potential and electric field distribution from the numerical models. (a) and (c) correspond to the case with the tip; (b) and (d) are the results from the simulation including the tip.

5.2.3 Concluding Remarks

To summarise, the gate electrostatics of RIE-etched (SC) and PA-etched (RC) graphene constrictions have been investigated by performing the planar surface potential using AM-KPFM. The expected charge accumulation around graphene constriction edges is absent even for the constriction with lower edge disorders. According to the analysis on the

results, it may attribute to: (1) The edges are probably not sharp and clean enough to accommodate the injected charges. (2) The presence of air. The detrimental adsorbates, such as water molecules, gas molecules and particles from the air may redistribute the charge distribution and cause potential variations. (3) Surficial contaminates, which are induced from the device fabrication process. (4) It is known that charge traps are typically found in SiO₂, and considering the few nanometres thickness of the HMDS, substrate effects from SiO₂ would also make a difference on the carrier concentration in graphene. (5) The KPFM measurements were carried out in dual-pass AM-KPFM. Substantial parasitic capacitance has an effect on the magnitude of the measured potential.

Based on the conclusions on the HMDS-supported open graphene nanoconstrictions, it is therefore the gate electrostatics in hBN encapsulated graphene nanoconstriction has been further investigated. Surface potential mapping were carried out using FM-KPFM performed in vacuum.

5.3 Charge Distribution in Semi-etched Encapsulated Graphene Nanoconstrictions

As the previous discussion, the probed surface potential via KPFM is more likely influenced by the disorder, measuring environment, surface contaminations, the substrate and the performing technique. We did not observe any clear indications of the charge accumulation at the graphene edges. A semi-etched graphene constriction was thus studied as a promising candidate for visualizing the presence of the charge accumulation. In the semi-etched constriction, we kept one of the edges unprocessed to avoid the external disorders and contaminants at the edge, while the other edge was etched by RIE. Additionally, graphene was encapsulated in hBN layers using the hot pick-up technique. Giving the fact of KPFM being as surface characterization technique, the top hBN layer must be thin enough so that the electric response of graphene to the applied gate bias can be effectively detected by the probe. We found out a thickness around 10 nm is appropriate based on our performed measurements.

The presented samples in this section were all fabricated at DTU, the KPFM measurements were all performed at the National Physical Laboratory.

5.3.1 Sample Preparation and Experimental Setups

In an attempt to investigate the edge disorder effects on the charge distribution, hBN encapsulated graphene was semi-etched. First, we aimed to find the graphene flakes with straight edge(s), then accomplished the stacking following the instructions of the thin stack assembly ([Chapter 4](#)). **Figure 5.11 (a-c)** illustrates the process of the stacking assembly. **(d-f)** shows the OM images of the individual step with respect to the sample preparation. The obtained device is shown in **(g)**. The metal electrode consists of 5 nm Cr

and 45 nm Au. A probe station, which is located in DTU Danchip cleanroom, was employed to test the electrodes⁵. It is worth mentioning that only the top hBN layer and the graphene have been etched, the bottom hBN layer was kept to screen charge variations from the underlying SiO₂[141].

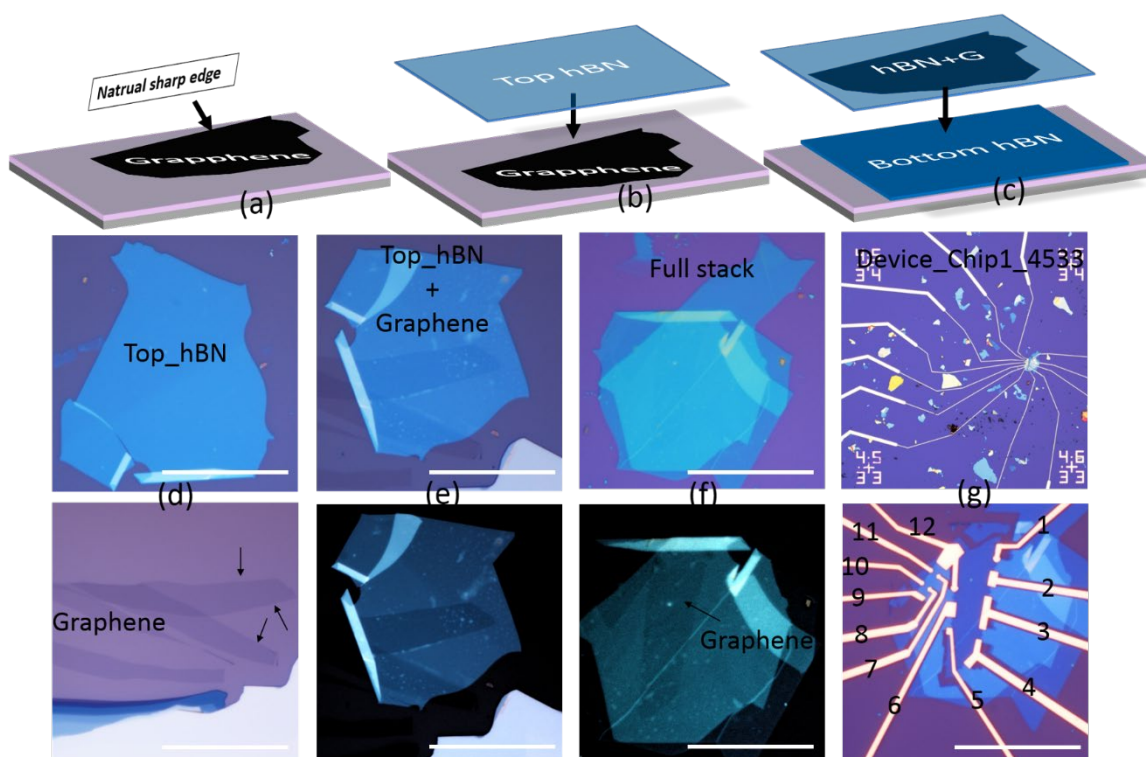


Figure 5.11 (a)-(c) depicts the stacking process after a precheck by optical microscope identifies graphene flakes with clean and sharp edge(s); (d)-(f) shows OM image of the individual fabrication step of device Chip1_4533: (d) top hBN needs to be thin, and at least one edge of the graphene flake has to be clean and sharp (see the arrows); (e) and (f) are the OM images of the stack with enhanced contrast to check the cleanliness and contamination between the neighbouring layers as well as the contour of graphene. (g) The final view of the device. The scale bars are 20 μm .

A schematic of the experimental setup is shown in **Figure 5.12 (a)**. A ceramic chip holder with 12 conductive metal pads around the chip and corresponding 12 pin connections on the backside was used. Silver paste was used to fix the chip as well as a connection between the backgate and one of the metal pads. Aluminium wires (\varnothing 30 μm) were bonded as the interconnections between the device and metal pads, see **Figure 5.12 (b)**. A probe station was subsequently used to check the connection between the device and the chip holder. An NT-MDT Ntegra Aura SPM system (from National Physical Laboratory) was employed which can be operated either in ambient environment at a controlled temperature of 18 $^{\circ}\text{C}$ and humidity of $\sim 35\%$ or in vacuum ($P \approx 10^{-6}$ mbar), see **Figure 5.12 (c-d)**. Bruker highly doped silicon tips (PFQNE-AL) with a force constant of ~ 0.9 N/m

⁵ The electrode tests were carried out with the help of Lene Gammelgaard and Bjarke Sørensen Jessen.

and resonant frequency of ~ 300 kHz were used. A single pass FM-KPFM technique, which takes advantage of the electric force gradient to calculate the contact potential difference between the tip and the sample, was used in this work. An AC bias of 3-5 V was applied at a lower modulated frequency, $f_m \approx 5$ kHz, and the DC bias was applied based on the detected amplitude signal at $(f_0 \pm f_m)$ to nullify the potential difference. It is by recording the DC bias to create a map of the sample's surface potential. The topography was recorded simultaneously with the surface potentials. In the FM-KPFM measurements, the graphene devices were grounded. A gate voltage was applied to the back side of the chip with respect to the ground and the gate leakage current was constantly monitored.

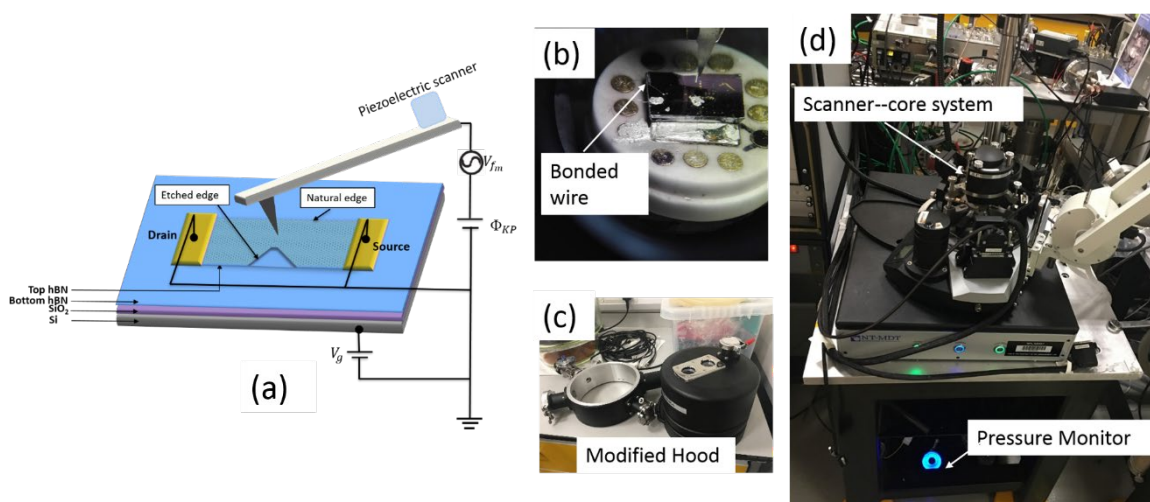


Figure 5.12 (a) A schematic of the experimental setup. (b) The sample is mounted on a ceramic chip holder. and Aluminium wires build up the connection between the sample and the metal pads on the chip holder using the ultrasonic bonding. (c) and (d) are the modified NT-MDT Aura scanning probe microscopy system. It allows the KPFM measurements carried out in vacuum.

5.3.2 KPFM Results and Discussion

Morphology and surface potential mapping of the semi-etched metal constriction

We first performed the KPFM measurements on a semi-etched metal constriction in vacuum, as shown in **Figure 5.13**. The metal consists of a 5 nm Cr and a 45 nm Au. A gate voltage of 0 V, 1 V and 2V were applied on the sample individually. **Figure 5.13 (a)** shows the topography AFM image of the semiconstriction, the contour is clearly seen. **Figure 5.13 (b)** is the surface potential mapping at $V_g=0$ V. A probe work function of 4.09 eV from the previous work *V. Panchal et al.* [110] can be referred to calculate the work function of the Cr/Au. The obtained contact potential difference is read from the potential mapping, $\Delta V_{CPD} = -0.6$ V. Based on $\Phi_{Cr/Au} = \Phi_{Tip} - e\Delta V_{CPD}$, the sample work function is hence obtained by substituting the values into the equation, $\Phi_{Cr/Au} = 4.69$ eV. Considering a presence of the surficial contaminations and a possible diffusion[142] between the Cr ($\Phi_{Cr}=4.5$ eV) and Au ($\Phi_{Au}=5$ eV), the measured work function is reasonable. The surface

potential profiles by crossing the narrowest part of the semiconstriction is plotted in **Figure 5.13 (c)**.

As expected for any metallic strip, the electrostatic potential across the metal semiconstriction is rather flat for any applied gate voltage. The fluctuations of the measured surface potential and the non-zero surface potential of the substrate are probably related to a presence of the contaminations from the device fabrication. However, the surface potential of the substrate stays stationary with the applied gate bias, it is hence the presence of the contamination will not qualitatively affect the surface potential of the device. Additionally, we have not seen charge accumulation at the metal semiconstriction. The performed KPFM measurements are discussed in the following.

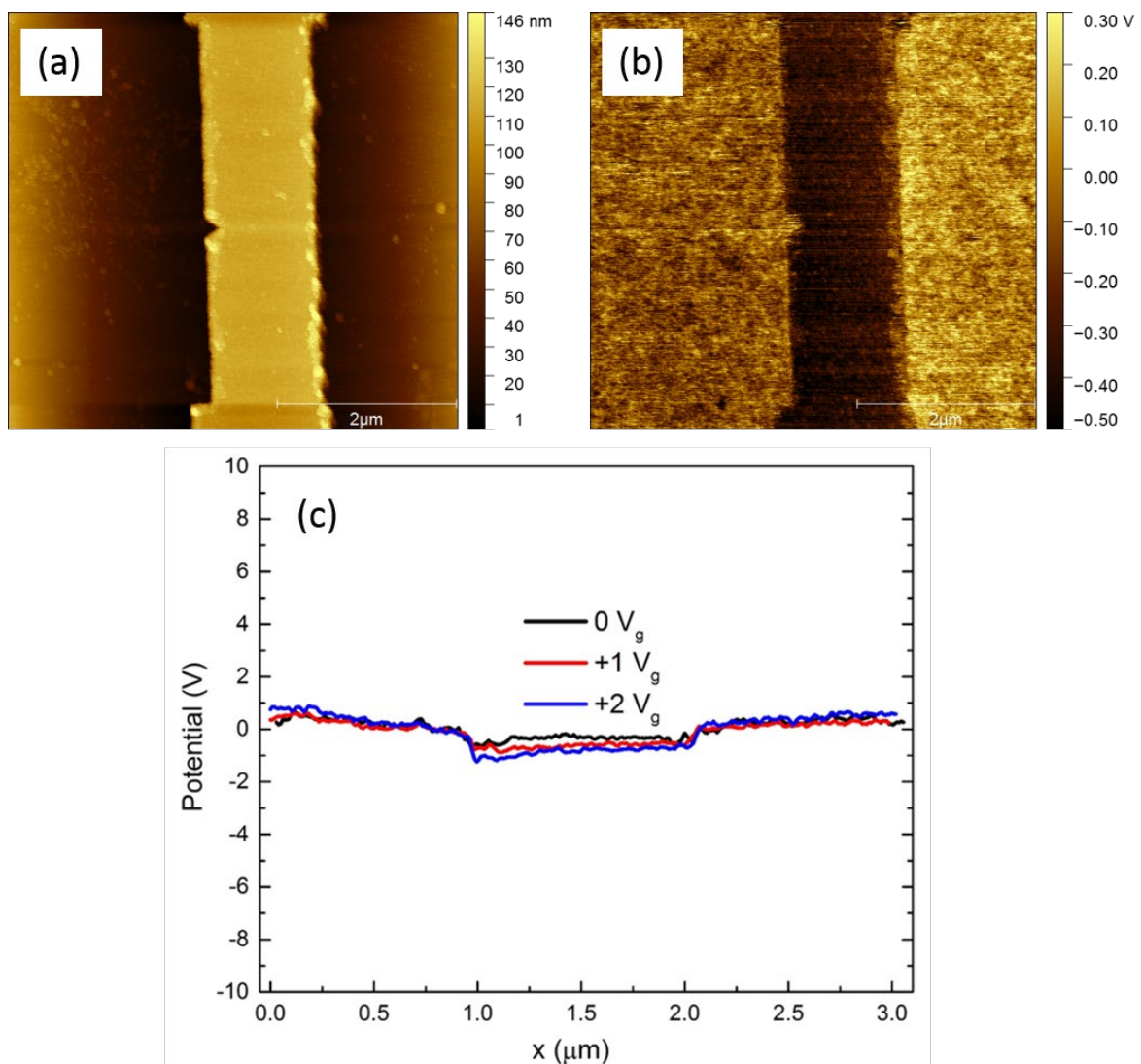


Figure 5.13 (a) Topography map of the device showing the semi-etched Cr/Au constriction. The width with respect to the narrowest section is about 700 nm, which is consistent with the width of the investigated graphene semiconstrictions. (b) FM-KPFM surface potential map of the device at a $V_g = 0$ V. (c) Plot of the surface potential for the biased device across the semiconstriction.

Morphology and surface potential mapping of the semi-etched encapsulated graphene constriction

The first investigated device is semiconstriction elec2-3⁶ on Chip1_4533, topography map and the surface potential map at 0 V_g are shown in **Figure 5.14 (a)** and **(b)**⁷. We noticed something unusual in regard of the device. From the AFM image, it seems that the top layer slid away with a distance of ~ 350 nm before the metallisation forming an “overlapped” semiconstriction. It was unclear either the whole top hBN layer or just partly of the top hBN layer or both the top hBN layer and the graphene or the whole stack has slid away. It is also necessary to check the presence of the graphene in the stack. In order to dispel the doubts, the height profile across the overlapped semi-constriction was investigated and a C-AFM was further carried out on the device. Additionally, the semiconstriction is shaped well using the standard lithography fabrication methods, which is observed from the AFM image of the device. The width of the narrowest part of obtained overlapped semiconstriction is about 700 nm.

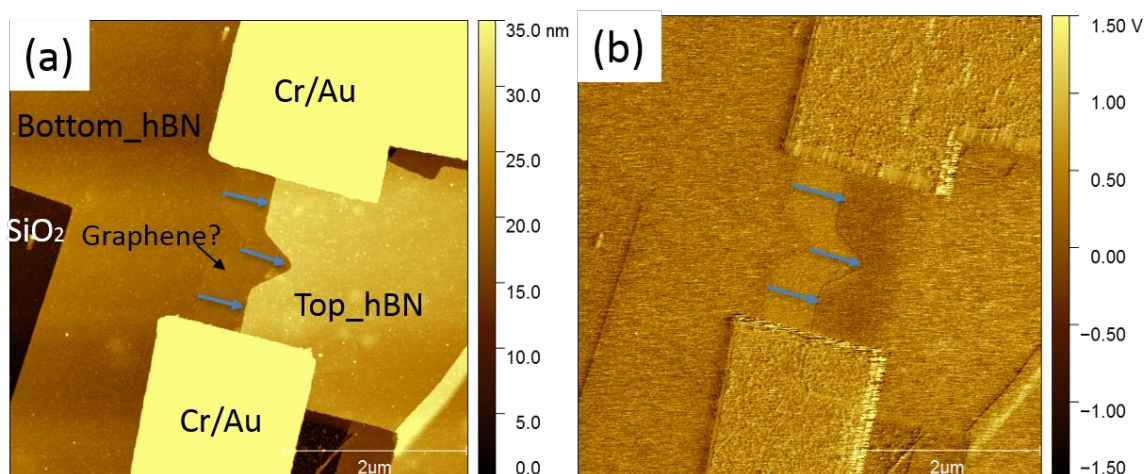


Figure 5.14 (a) AFM topographic image of device semiconstriction elec2-3 on the chip1_4533. An overlapped semiconstriction can be observed from the topography; (b) is the surface potential mapping at 0 V_g . Blue arrows indicate the distance and direction of the sliding layer.

Plot of the height profile for the overlapped semiconstriction elec2-3 along the dashed line depicted in **Figure 5.15 (a)** was shown in **Figure 5.15 (b-c)**. The cut line is divided into

⁶ A “elec2-3” means the semi-constriction device between electrode 2 and electrode 3, as shown in Figure 5.11 (g).

⁷ It is worth mentioning that only the KPFM measurements in Figure 5.13 and Figure 5.14 were performed on a Bruker Dimension Icon SPM system, since a C-AFM was needed to check the device. The NT-MDT Aura SPM system was not available for C-AFM in the lab of Nation Physical Laboratory.

A, B and C three parts to represent an explicit guide to the eye. From the height profile, a thickness of around 10 nm is obtained, which is very close to the top hBN layer used for the stacking. The height difference between area B and C is around 1.2 nm, which is comparable to the topography map of graphene using the scanning probe microscopy [110], [143], as the standard lithography device fabrication method usually induces a thin layer (1-2 nm) of polymer residual on top of graphene. A conductive-AFM (C-AFM) was further performed to check the presence of graphene. As illustrated in **Figure 5.15 (d)**, contour of the conductive graphene and the metal electrode (the top metal electrode was not in use during the scan of the C-AFM operation) are observed. According to the location and the presence of graphene, we hence infer the slid layer is only the top hBN layer, and partly of the graphene is exposed in the air while the rest is encapsulated in hBN layers.

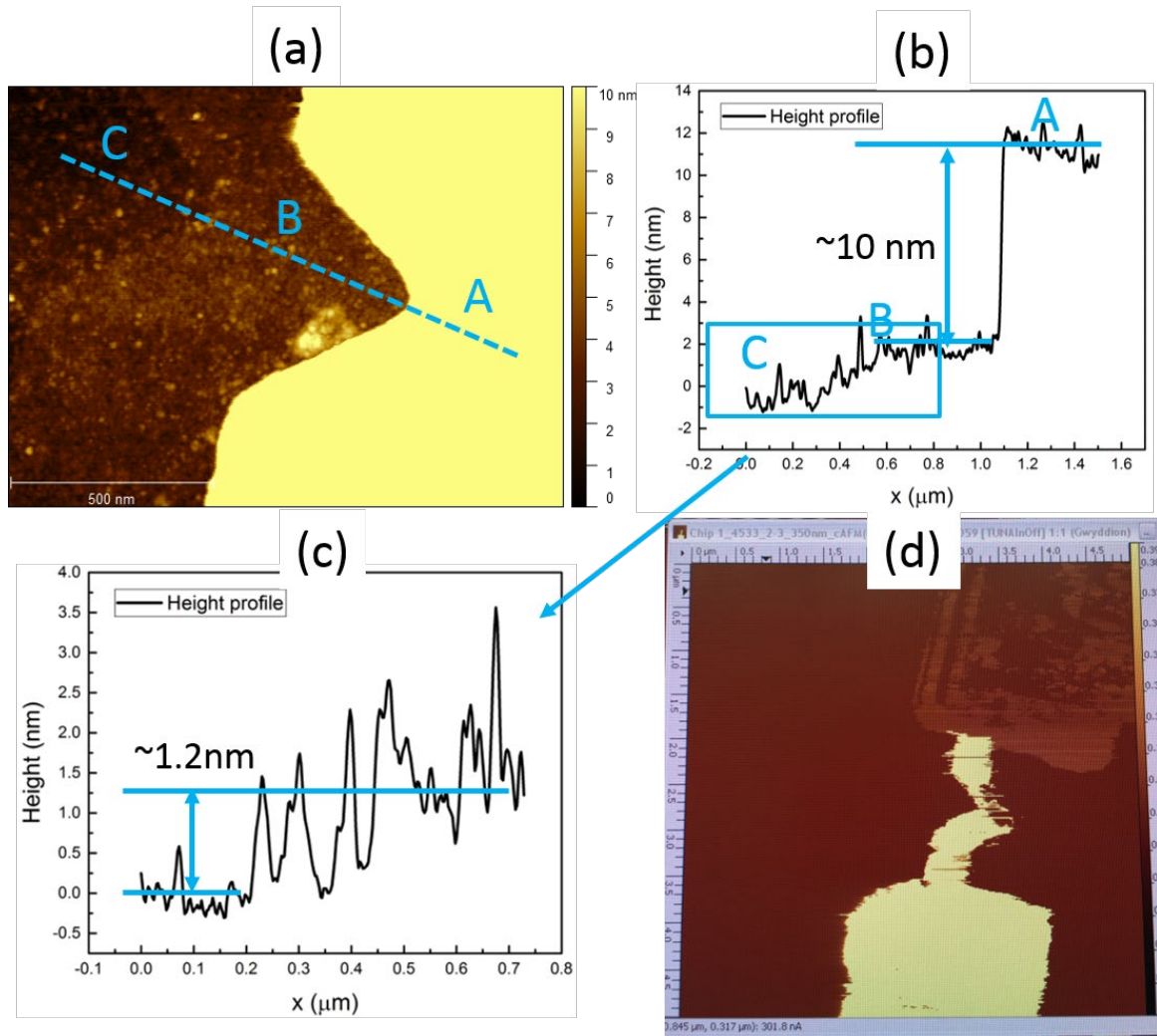


Figure 5.15 (a) A focused AFM scan is conducted on the overlapped semi-constriction. (b) The height line profile along the cut line indicated in (a). (c) A magnified height profile of the blue square area depicted in (b). (d) A C-AFM⁸ is performed on the device to check the presence of graphene, noted the top electrode was not in use.

Subsequent KPFM measurements were performed in vacuum, **Figure 5.16 (a)** presents the topography map of the semiconstriction elec2-3. The obtained topography map is slightly different from the previous topography (**Figure 5.14 (a)** and **Figure 5.15 (a)**). It seems slightly damaged. This could be attributed to the probe accidentally touching the sample to locate the sample position at the beginning. However, the presence of the graphene is validated using the previously method, this can be observed from the height line profile across the overlapped semiconstriction elec2-3, as shown in **Figure 5.16 (b)** and **(c)**.

⁸ The C-AFM image presented here is a photo captured during the measurement, the initial data is lost.

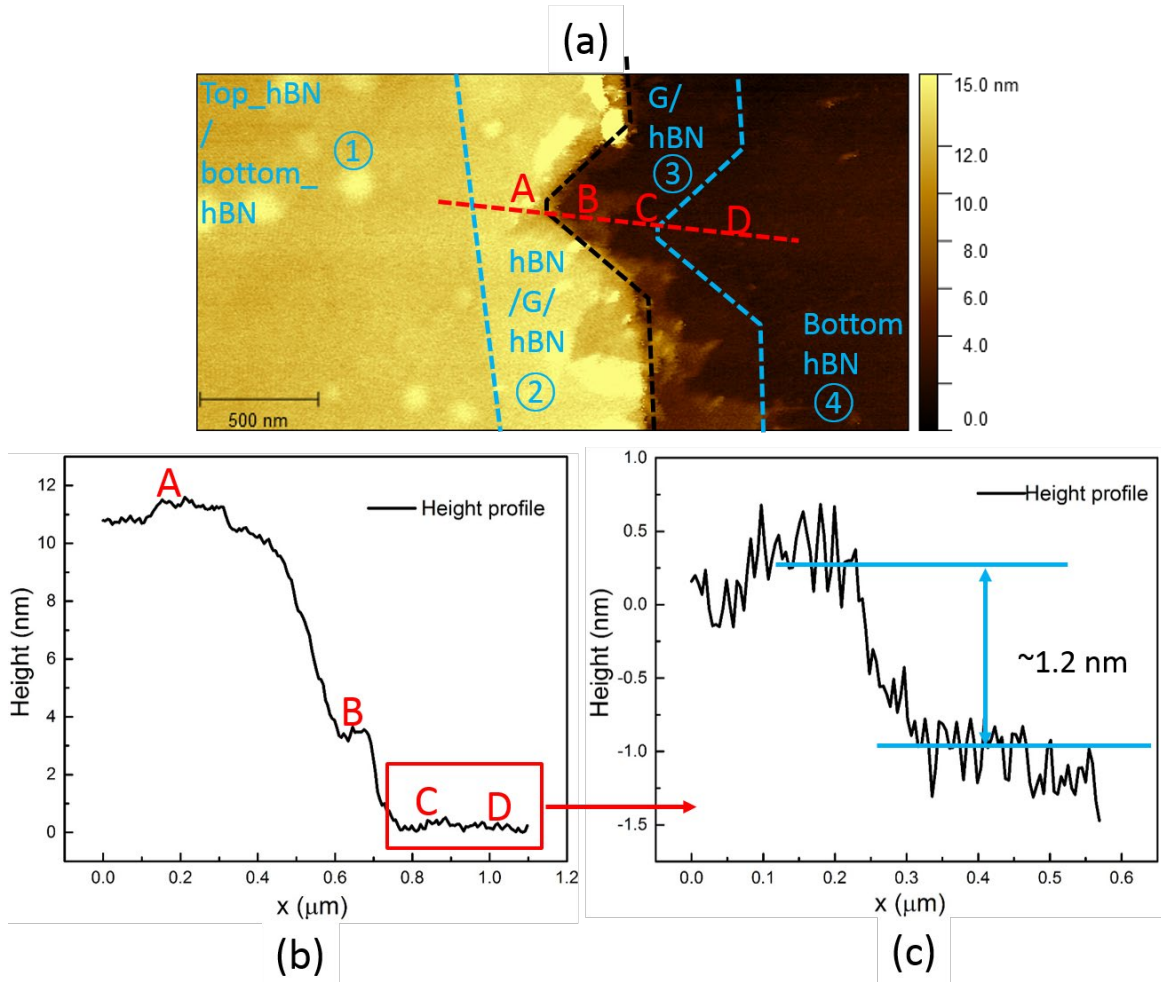


Figure 5.16 The topography map of the semiconstriction elec2-3 performed in vacuum. (a) Four different zones are indicated here to represent an explicit guide to the eye, including: Zone ① of only hBN layers, zone ② of the full stack with the natural graphene edge depicted in dashed line, zone ③ graphene located on bottom hBN layer and zone ④ of the bottom hBN layer with the other etched edge depicted in dashed line. The black dashed line indicates edge of the slid top hBN layer. (b) and (c) are height line profiles of the red cut line depicted in (a). The letters of A, B, C and D are used to denote the position on the sample.

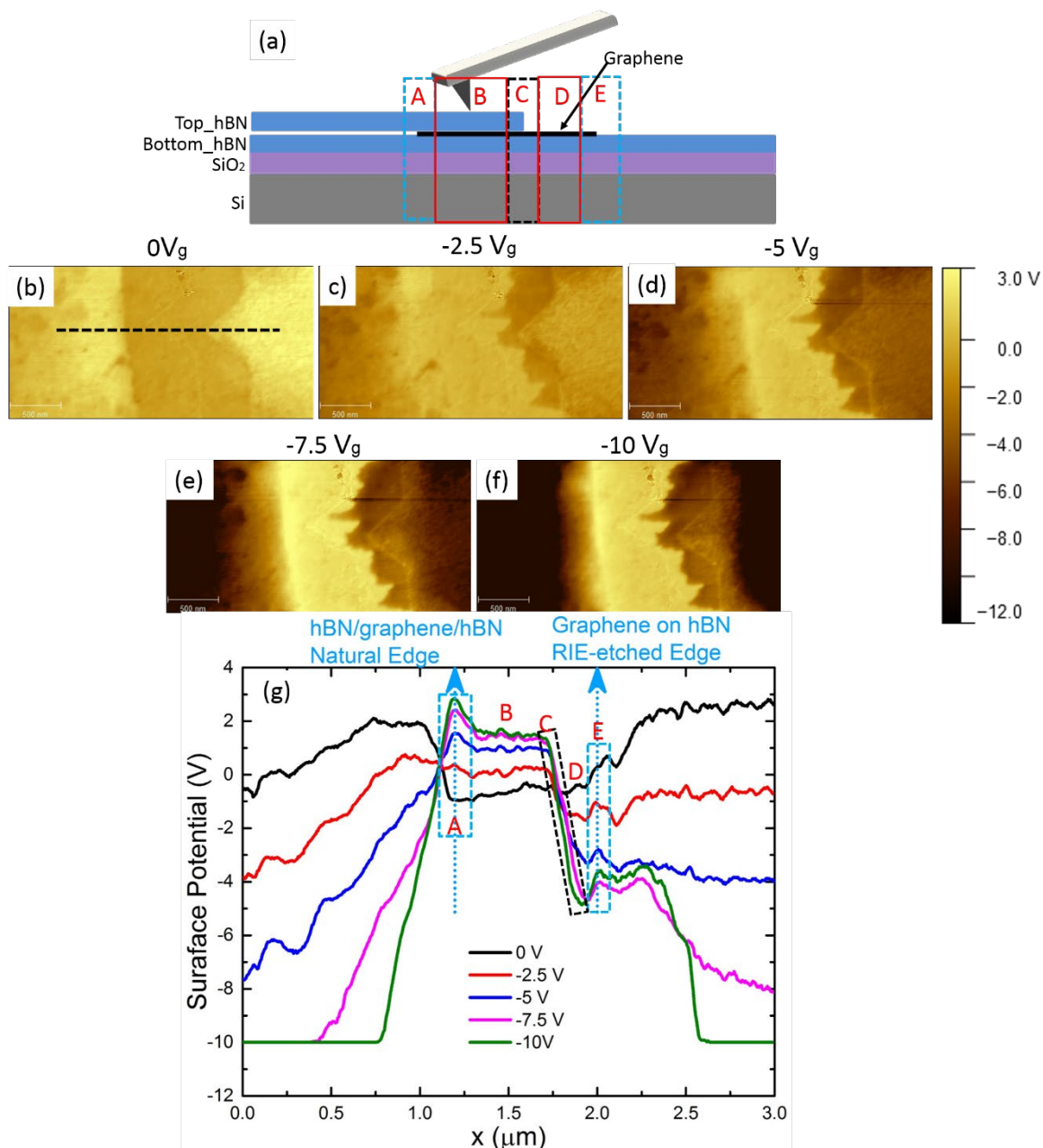


Figure 5.17 KPFM measurements of semiconstriction elec2-3. (a) A sideview of the device, the divided zones with the capital letters represent a guide to the eye on the layout of the device. Parts from A to E corresponds the natural graphene edge (A), the fully embedded graphene (B), the boundary of the slid top hBN layer (C), the exposed graphene situated on bottom hBN layer (D) and the etched graphene edge (E) separately. (b)-(f) The surface potential maps with different gate bias. All the surface potential maps are represented with the same surface potential scale bar. (g) Plot of the surface potential for the gated device along the dashed line depicted in (a).

The KPFM measurements of the gated semiconstriction elec2-3 are shown in **Figure 5.17**. A sideview of the device is depicted in **Figure 5.17 (a)** to provide an explicit interpretation of the device configuration. In order to facilitate the discussion on the result, the device is hence divided into five parts: A, B, C, D and E corresponding to the natural graphene

edge (A), the fully embedded graphene (B), the hBN layer boundary of the overlapped semiconstriction (C), the exposed graphene on the bottom hBN layer (D) and the etched graphene edge (E). The surface potential line profiles across the semiconstriction elec2-3 are plotted in **Figure 5.17 (g)**.

There are noticeable upturns at both the natural graphene edge and the RIE-etched graphene edge, which is in a good agreement with the analytical description in the theory (**Chapter 2, section 2.3**), suggesting that the charge accumulation at the graphene edges is vitrified in our work using the KPFM. The upturned degree is proportional to the magnitude of the applied gate voltage, see the **Table 5.1**, which implies an effective electron injection from the applied electric field. Utilizing the extracted data from the table, we carry out the comparison on the potential enhancement of the two types of edge. The slightly smaller values ($V_E - V_D$) suggest a relevance of the etching-induced disorders at the edge, here V_E, V_D are referred to as the mean value of surface potential of part E and part D separately. The potential enhancement at the 0 V is not obvious, probably because it is close to the charge neutral point.

V_g (V)	The surface potential difference between A and B ($V_A - V_B$)	The surface potential difference between E and D ($V_E - V_D$)
0	--	--
-2.5	0.33	0.33
-5	0.59	0.5
-7.5	0.93	0.73
-10	1.36	1.23

Table 5.1 A comparison on the potential enhancement between the natural graphene edge and the etched graphene edge.

As one may have noticed, from V_B to V_D there is a “switch” in terms of the polarity of the measured surface potential. It is known that the probed surface potential is related to the work function difference between the employed tip and the graphene, given as: $V_{CPD} = \frac{\Phi_{tip} - \Phi_{graphene}}{-e}$, and $\Phi_{graphene} \propto E_F$ where E_F is related to the applied gate bias, V_g . Back to the surface potential plot shown in **Figure 5.17 (g)**, the opposite polarity of the measured surface potential implies this graphene semiconstriction somehow represents both p-type and n-type regions. In other words, the graphene here forms a seamless lateral p-n junction. The boundary of the slid top hBN layer (Part C) becomes the transition between the p-type graphene (Part A and B) and n-type graphene (Part D and E). Such carrier type from the n- to p-type transition in graphene has previously been reported for graphene using scanning gate microscopy[15], scanning photocurrent microscopy (SPCM)[144] and KPFM[145]. But it is very different from the case here: J. Chae et al.[15]

observed the transition at the graphene channel edge which is related to the tip gating potential. The applied the tip can locally tune the carrier type in graphene, owing to the charge accumulation at the edges, if the injected carriers from the tip bias are less than the accumulated charges, it is therefore a carrier-type transition occurs at the graphene channel edge. But it will disappear when the injected carriers are comparable to the accumulated charges at the edge. This is similar to the case from *V. Panchal* et al. [145], except using a side gate to tune the doping in the graphene channel. But they attributed this carrier type transition at graphene channel edge to the etching induced defects and the adsorbates. Another work with respect to observation of the transition is from *J.H. Lee* et al. [144]. However, such carrier type transition was overserved at the graphene/electrode interface, which we will not further discussed.

It is well known that graphene can be doped using a chemical or physical method[146]–[150]. However, it is “mysterious” considering the formed p-n junction in our device. Several scenarios may be considered for the origin of the observed carrier type transition in the device. First, the surficial contamination on the semiconstriction. Since the top hBN layer slid away, the surface of the exposed graphene is supposed to be cleaner. Although the trapped impurities can be charged, they only make quantitatively change on the surface potential as the fluctuations over all the device, which we have mentioned in the KPFM measurements performed on the metal semiconstriction. Second, the top hBN layer is only difference in terms of the device configuration. However, hBN is a wide-gap insulator which is often used to enhance the quality of graphene[84], [151]. This attribution is probably not convincing. Third, it may be related to the coupling between the probe and the sample, which is also hard to verify. It is difficult to give an explicitly interpretation from our results. Therefore, it would be interesting if the investigation on the p-n junction can be further carried out.

FM-KPFM was further performed on another semiconstriction elec1-2 on Chip1_4533 in both vacuum and the ambient environment. **Figure 5.18** and **Figure 5.19** show the topography map and the surface potential maps at different gate voltages. Unlike the slid top hBN layer in semiconstriction elec2-3, the semiconstriction elec1-2 is a bit more complicated. In particular, the top hBN layer in the stack here was somehow cleaved, which can be observed from the height line profile (see **Figure 5.18 (b)**). The denotations represent a guide of the device configuration to the eye. Zone ① Indicates an area consisting of top hBN layer and bottom hBN layer. Zone ② indicates the complete stack in which the thickness of the top hBN layer is ~ 10 nm. Zone ③ indicates the “new” stack in which the thickness of the top hBN layer is ~ 3 nm. Zone ④ indicates the unetched bottom hBN layer. The width of the narrowest part of obtained overlapped semiconstriction is about 700 nm.

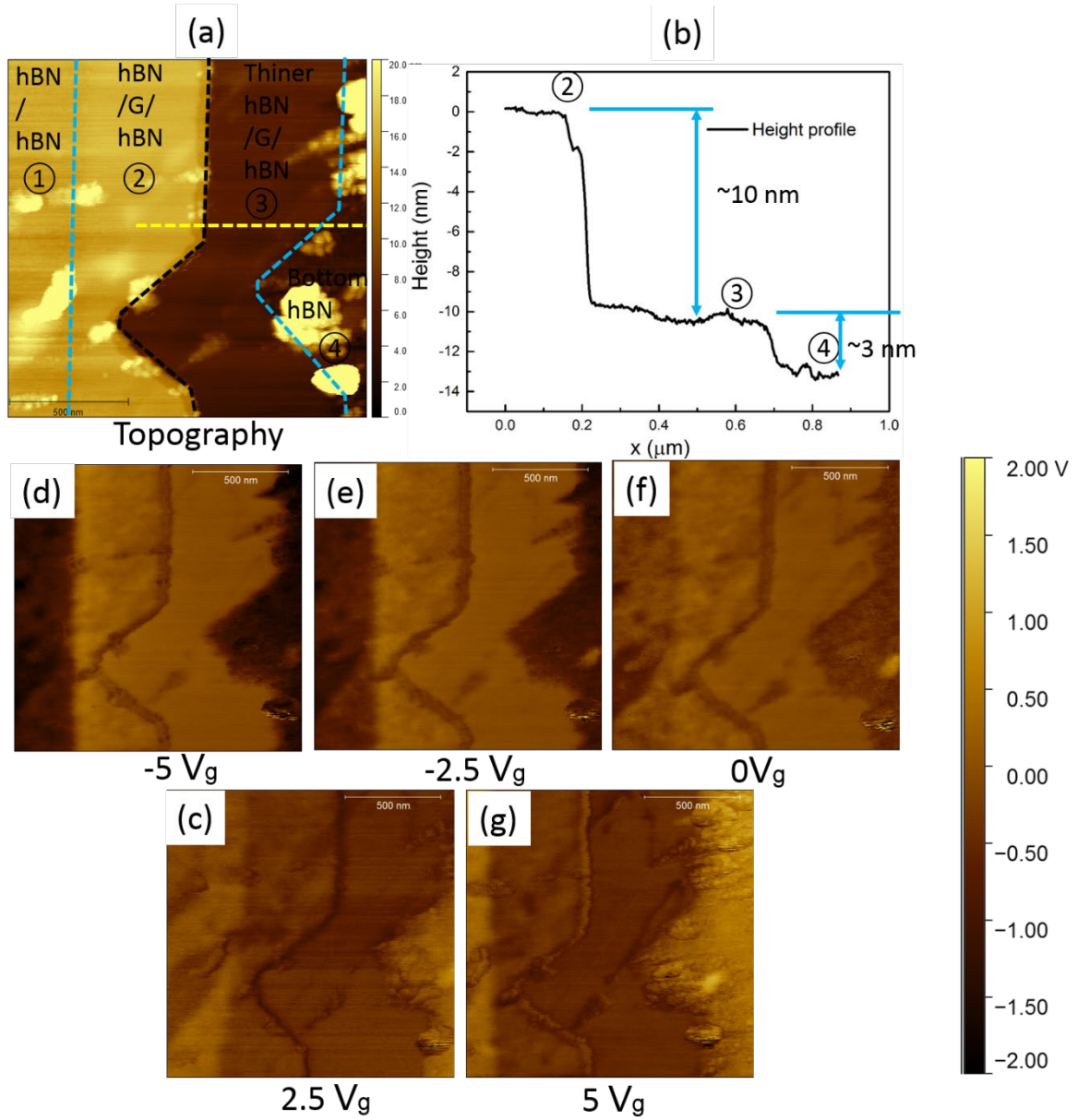


Figure 5.18 Topography map (a) and surface potential maps (d-g) of semiconstriction elec1-2 on chip1_4533 which are performed using FM-KPFM in ambient environment. All the surface potential maps are represented with the same surface potential scale bar. (b) Height line profile of the cross section which is indicted in (a) using the yellow dashed line.

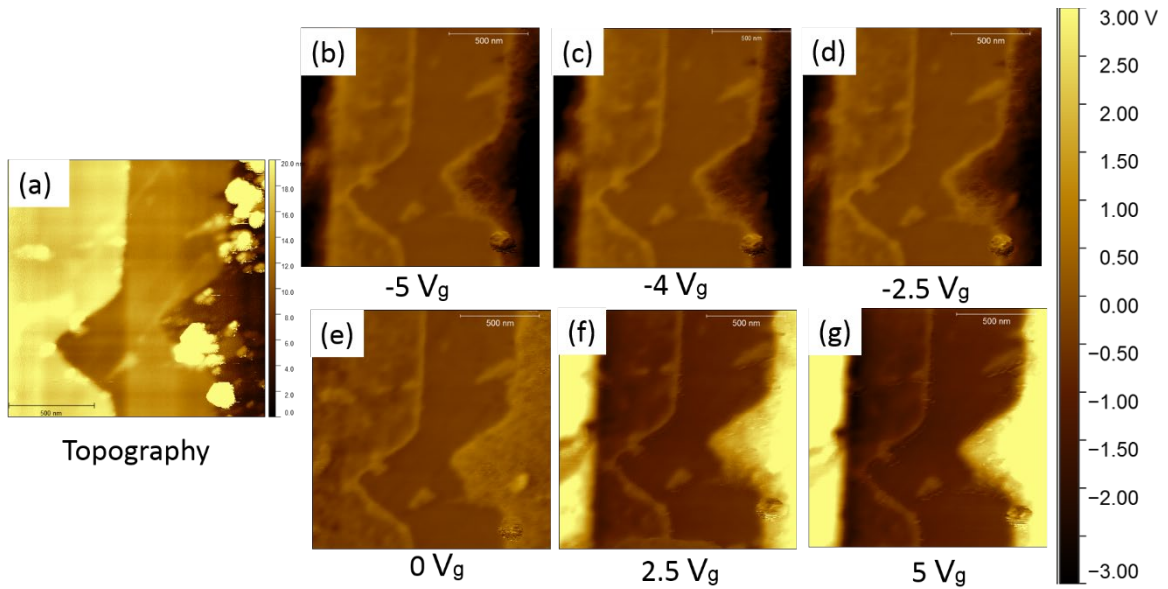


Figure 5.19 Topography map (a) and surface potential maps (b-g) of semiconstriction *elec1-2* on *chip1_4533* which are performed using FM-KPFM in Vacuum. All the surface potential maps are represented with the same surface potential scale bar.

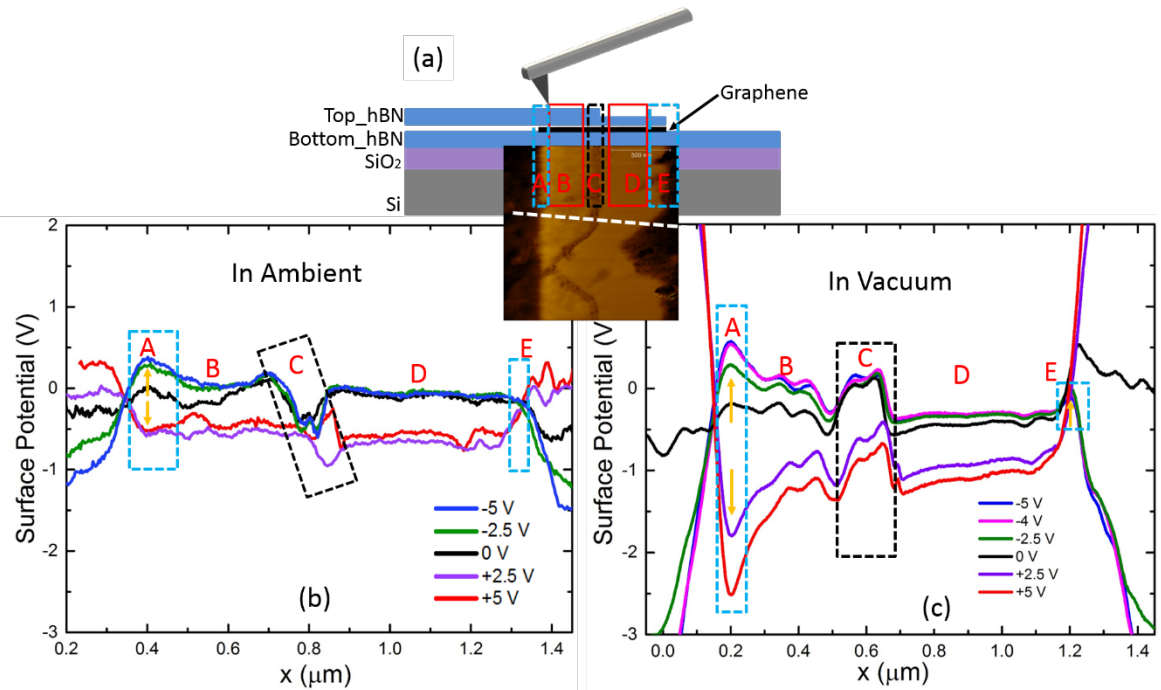


Figure 5.20 (a) A sideview of the device configuration. Capital letters from A to E are used to represent a guide to the eye. A: the natural graphene edge; B: the initial stack with a thicker top hBN layer; C: the boundary of top hBN layer; D: the new stack area with a thinner top hBN layer; E: the etched graphene edge. (b) and (c) are the plots of surface potential line profiles across the whole overlapped semiconstriction along the white dashed line depicted in (a).

A schematic of the sideview in terms of the device configuration is shown in **Figure 5.20 (a)**. The denotations A-E indicate the natural graphene edge, the initial stack with a thicker top hBN layer, the boundary of top hBN layer, the new stack area with a thinner top hBN layer and the etched graphene edge, separately. **(b)** and **(c)** in **Figure 5.20** individually show the cross section (along the white dashed line in **(a)**) of the back gated KPFM in ambient environment and vacuum.

The upturns/downturns of the measured surface potential at the graphene edges representing a presence of the charge accumulation are observed in both KPFM measurements (as the arrows indicated in **Figure 5.20 (b)** and **(c)**). However, the charge accumulation caused potential enhancement at the etched graphene edge is not observed in the ambient measurements, as the dashed square E indicated in **Figure 5.20 (b)**. As for the comparison on the potential enhancement of the two types of edge, it is consistently with the previous semiconstriction elec2-3. The enhancement of the surface potential at the natural graphene edge is larger than that at the etched graphene edge, which is related to the etching induced disorders and contaminations from the device fabrication process. Moreover, the potential enhancement at both edges from the KPFM measurements carried out in ambient environment is much smaller than that from the KPFM measurements performed in vacuum, suggesting that a charge redistribution across the graphene channel caused by the adsorbates from the air [139], [140], [152]. As such, this to some extent explains the missing of charge accumulation in the HMDS-supported open graphene constriction devices.

Besides the observation of the charge accumulation, there are something else interesting from the plots which also grabbed our attentions. First, regarding the KPFM measurements performed in vacuum, it seems there is an absence of the charge accumulation at the etched edge when a positive gate voltage is applied, which we do not fully understand. Another fact that one may have noticed is the potential fluctuations at part B while part D presents to be rather flat. This is understandable since the top hBN layer of the new stack (part D) was cleaved from the initial top hBN layer, although we do not know how and when that happened, the cleaved hBN presents to be much cleaner. Third, rather than a n-doped graphene is usually obtained in the open graphene constriction situated on HMDS/SiO₂, the encapsulated graphene semiconstriction is p-doped.

Considering the accidental slid hBN layer in last two semiconstriction, new devices were made for more KPFM measurements, as shown in **Figure 5.21 (a)**. Surface potential measurements were further carried out on two graphene semiconstriction (which are referred to as Device1 and Device2 individually) using FM-KPFM in vacuum. **Figure 5.21 (b)** and **(c)** show the topography map and surface potential map at 0 V_g. Plots of the surface potential line profile along the dashed line depicted in **(c)** at different gate voltages are demonstrated in **Figure 5.21 (d)** and **(e)**.

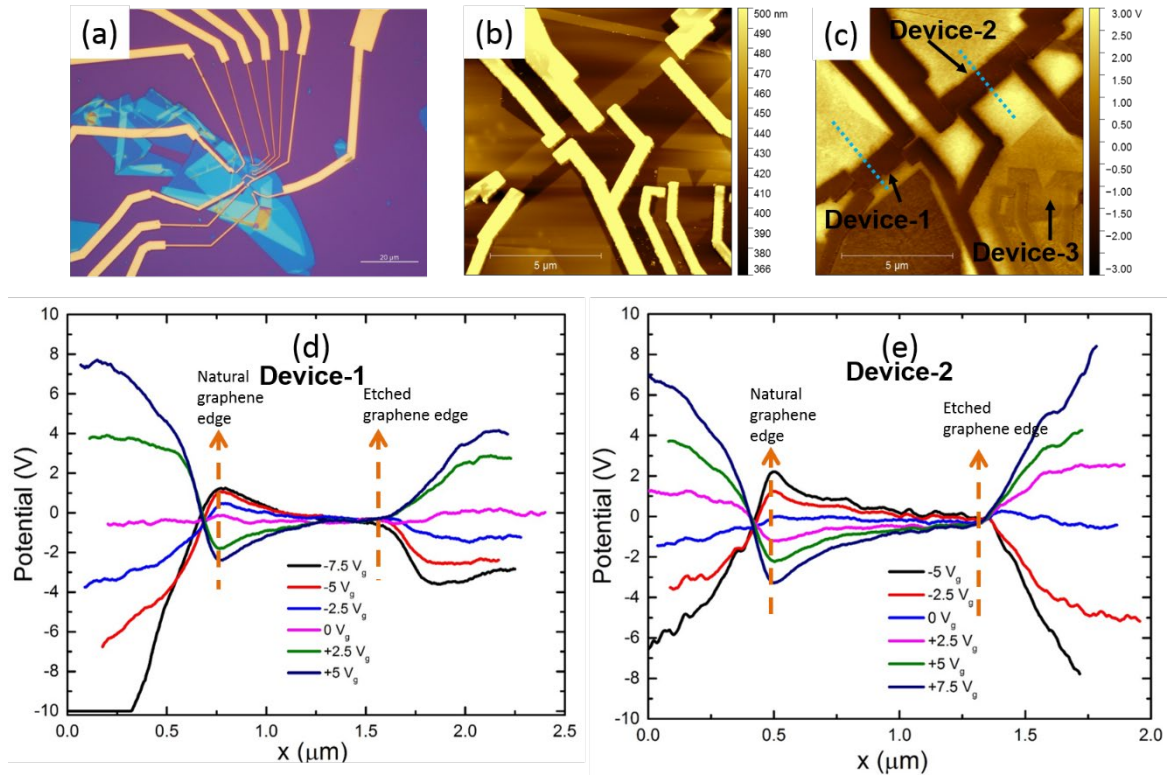


Figure 5.21 (a) The OM image of the sample. Topography map and surface potential map focused on the devices are illustrated in (b) and (c), the applied back gate voltage is 0 V. (d) and (e) are the plots of surface potential line profiles across the semiconstriction along the dashed line depicted in (c). the natural graphene edge and the etched graphene edge are denoted with arrows.

The graphene semiconstrictions are well-shaped and accidents with respect to the slid hBN are not observed from the topography map. We kept the width as the same as the previously investigated semiconstrictions, which is 700 nm. Surprisingly, the charge accumulation is only observed at the natural graphene edges and absent at the etched edges for both Device1 and Device 2. Additionally, we noticed that there is a big difference on the surface potential between the trace KPFM measurements obtained from the forward scan and the retrace KPFM measurements obtained from the backward scan, which is shown in **Figure 5.22**. Such discrepancies are referred to as the “trace and retrace issue” in the following discussions. Prior to that, it is worth mentioning the presence of the charge accumulation at both the natural graphene edge and the etched graphene edge with respect to the measurements obtained from the backward scans, although the induced potential enhancements are small.

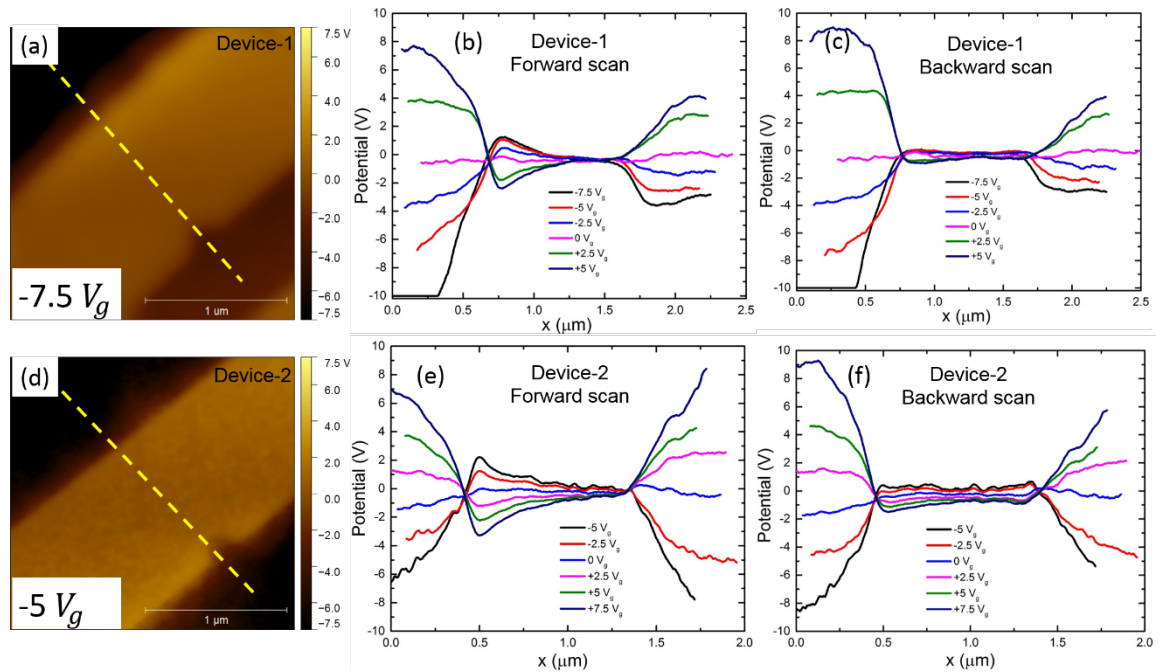


Figure 5.22 (a) and (d) are the surface potential maps of Device1 and Device2 at a $V_g = -7.5$ V and a $V_g = -5$ V individually, which represent a guide to the cross sections of the back gated KPFM measurements depicted in (b), (c), (e) and (f). The trace data obtained from the forward scan and the retrace data obtained from the backward scan are indicated.

Back to the trace and retrace issue, we tend to ascribe the discrepancies to the capacitive coupling between the tip and the underneath sample. It is known that KPFM working as a surface characterization technique is sensitive to the potential variations on the sample. Apart from an application of the gate bias, the measured KPFM is a weighted average of the surface potential[134], which we have discussed in [Section 5.1](#). Although the FM-KPFM has been previously proved to be slightly affected by the coupling[110], [131], [153], *G. Elias et al.* [136] concluded that the cantilever may largely influence the absolute value of the surface potential difference between the tip and the sample, and such influence has a relation to the tip-sample distance and the probe-surface angle. *V. Panchal et al.* [110] have also described that performing the scan across the device decreases the parasitic capacitance induced from the coupling.

Therefore, a comparison is carried out between the previous semiconstriction elec2-3 and the Device1, which is demonstrated in **Figure 5.23**. As for the semiconstriction elec2-3, the trace and retrace issue is not observed from the KPFM measurements (the proof is put in the [Appendix C](#)), which is probably related to the position of the probe and the scan angle, as shown in **Figure 5.23 (c)**. The probe-surface angle is 0 and tip moves across the graphene channel. However, as for the Device1, owing to a limitation from the bonding on electrodes, the KPFM measurements were performed in a way as shown in **Figure 5.23 (d)**. The probe-sample angle is about 45° , and the probe is tilted so that it could scan across the graphene channel. The possible presented parasitic capacitance is illustrated in **Figure 5.23 (e)** for FM-KPFM in vacuum. We infer that the total parasitic capacitance has been

changing or more likely increasing during the forward scan in a direction of distancing the graphene channel simultaneously getting more influences from the parasitic capacitance induced from the contaminations. The probed surface potential at the end of the forward scan is probably affected by the parasitic capacitance the most, which may explain the asymmetry of the surface potential beyond the graphene constriction in both the forward scan and the backward scan (see **Figure 5.22 (b) and (c)**).

Considering the charge accumulation induced enhancement on the surface potential is rather small as a function of the applied gate voltage, the influences from the parasitic capacitance are more likely unneglectable although the fact of the cantilever assembly considerably larger than the device.

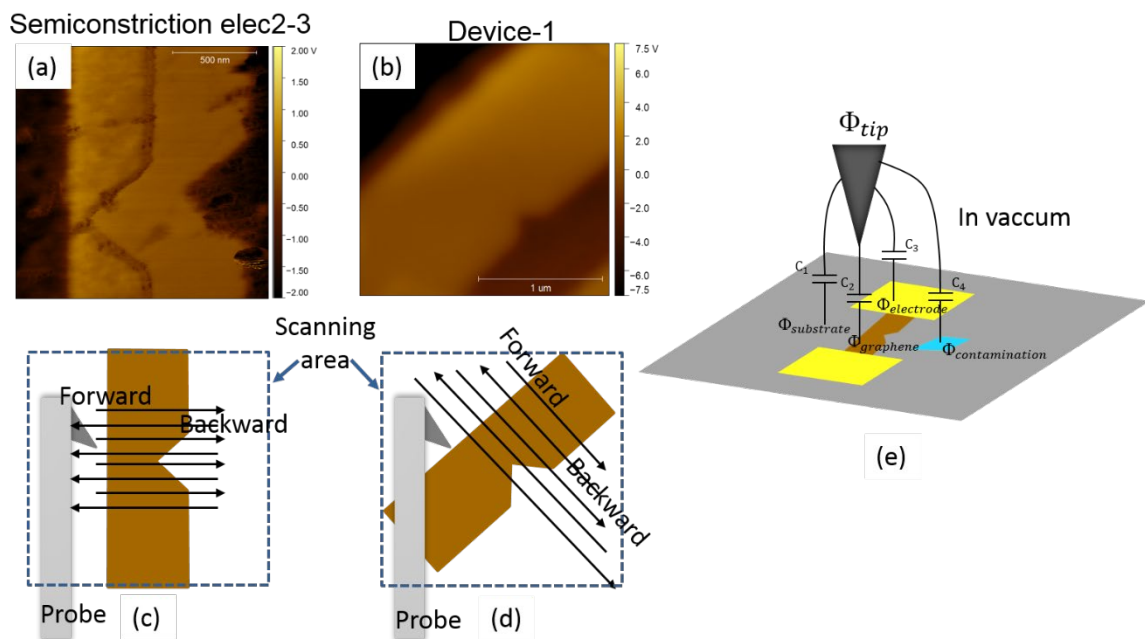


Figure 5.23 (a) (b) show the surface potential maps of semiconstriction elec2-3 and the Device1. The schematics in (c) and (d) are in accordance with the potential maps. The location of the probe and the scanning angel are indicated. The scanning area is defined using a square. (e) All the possible presented parasitic capacitance (C_1 , C_3 and C_4) is described in the model with respect to the case of FM-KPFM performed in vacuum. C_1 is induced from the difference between Φ_{tip} and $\Phi_{substrate}$. C_2 is induced from the difference between Φ_{tip} and $\Phi_{graphene}$. C_3 is induced from the difference between Φ_{tip} and $\Phi_{electrode}$. C_4 is induced from the difference between Φ_{tip} and $\Phi_{contamination}$.

Additionally, the KPFM measurements were also performed on an encapsulated graphene strip with a width of 3 μm in vacuum. Topography maps and the surface potential maps are demonstrated in [Appendix A](#), the charge accumulation is absent due to the large aspect ratio of the strip width to the insulator depth which weakened the fringe electrostatic field[10], [13], [22], [71].

5.3.3 Concluding Remarks

In this section, the hBN layer encapsulated semi-etched graphene constrictions, where one graphene edge is natural and another is RIE-etched, were investigated with respect to the gate electrostatics. The surface potential of a few devices were performed using FM-KPFM in vacuum. One of the devices has been measured in both vacuum and the ambient environment. The surface potential enhancements at the edges induced by the charge accumulation were observed in all the investigated devices.

In particular, the potential enhancement always presented at the graphene natural edge and was sensitive to the edge disorder and the measuring environment when it comes to the etched graphene edge. Additionally, the charge accumulation led to a higher enhancement of the potential at the natural graphene edge, the relatively smaller potential enhancement at the etched edge is related to a charge redistribution caused by the disorders from the etching. Specially, a somehow formed p-n junction was observed in one of the devices, a carrier type transition happened when the gate bias was applied on the device. A trace and retrace issue, with respect to the discrepancy of KPFM measurements between the forward scan and the backward scan, was discussed. We infer that the location of the probe and the probe-sample surface angle were the possible attributions. Last, all the investigated graphene semiconstrictions in this section presented slightly hole doped. This is different from the previously observed electron dope type in open graphene constrictions.

5.4 Summary

This work was carried out to study the gate electrostatics of the graphene nanoconstrictions. We aimed for the visualization of the charge accumulation using KPFM based on our analytical calculation. Two types of graphene constrictions were investigated including the HMDS-supported open graphene constrictions and the hBN encapsulated graphene semi-etched constrictions.

The first type includes the smooth constriction and rough constriction which were etched using RIE and PA separately. The KPFM measurements were performed on both constrictions using AM-KPFM in the ambient environment. However, the charge accumulation was not observed. It is possibly related to the presence of the air, edge disorders and the low resolution of AM-KPFM. The effects of the measuring tip may also be related.

The surface potential mapping of the other type were carried out using FM-KPFM in both vacuum and the ambient environment. We observed the potential enhancement at the graphene edges which are caused by the charge accumulation in all the demonstrated devices. However, the charge accumulation was only seen at the natural graphene edge

with respect to the device which was measured in air. Additionally, the charge accumulation induced potential enhancement presented larger at the natural edge. Owing to an accident of the slid top hBN layer in one of the devices, a somehow formed p-n junction was seen when the gate bias was applied, and we discussed the possible attributions. The long-range capacitive coupling between the probe and the sample was also mentioned relatively to the trace and retrace issue. Our results are qualitatively consistent with the analytical calculation. The charge accumulation can be visualized from the distribution of the local potential in the gated graphene device using KPFM.

6 Raman Characterisation of Bubbles in van der Waals (vdW) Heterostructure

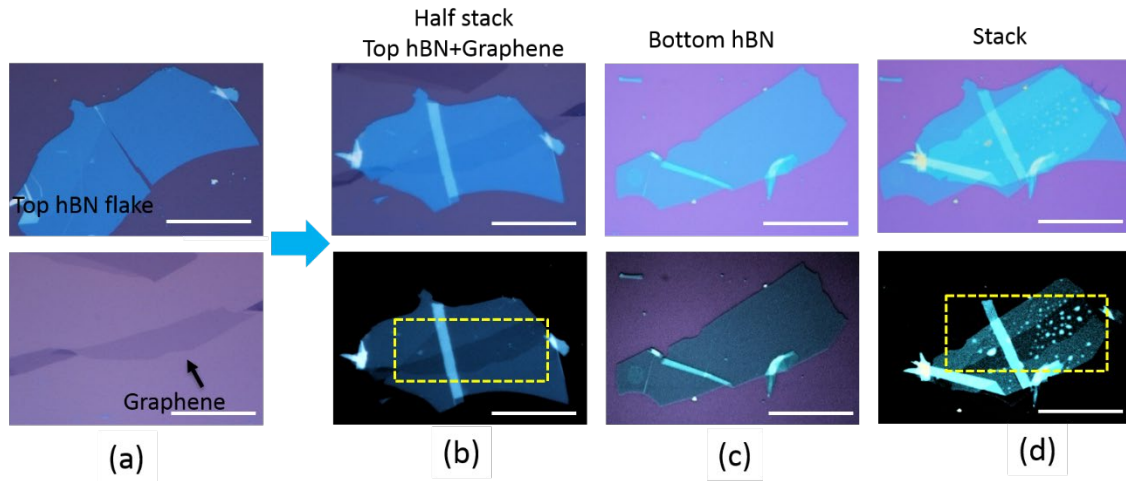
Chapter acknowledgements: all the presented samples were fabricated at DTU by myself, and all the Raman measurements as well as the fitting procedures were carried out by Tom Vincent at National Physical Laboratory, Tom and I were both contributed to the analysis and discussions, thus we both contributed to the work presented in this chapter.

6.1	Bubble Configuration in The vdW Heterostructure Assembly.....	81
6.2	The fitting model used for Raman measurements.....	83
6.3	Results and discussion.....	85
6.4	Concluding remarks.....	93

In this chapter, graphene bubbles are created below and above graphene by controlling the stacking assembly. The objective is to examine the strain and doping of the graphene bubbles in hBN/graphene/hBN vdW Heterostructures with a dependence on the bubbles' location.

6.1 Bubble Configuration in the vdW Heterostructure Assembly

To control the bubble location, each stacking procedure was recorded using the optical microscope during the van der Waals integration, see **Figure 6.1**. A careful and slow drop-down often avoids the bubble creation, while a hasty drop-down gives the occurrence of bubbles. Based on this hypothesis, the bubble location with respect to graphene is thus controllable. For example, **Figure 6.1** displays the creation of bubbles below graphene. First of all, top hBN and graphene flake both were carefully prechecked to exclude external contaminations. After obtaining the half stack (top hBN + graphene), another check on the half stack assured the interfaces bubble-free. The bubbles below graphene were created by performing a fast drop-down on the bottom hBN. The obtained stack1 in **Figure 6.1** was further checked using OM and AFM after the standard lithography device fabrication to assure the presence of the bubbles (see **Figure 6.2**). Two bubbles were selected for the study which are referred to as bubble #1 and bubble #2, as indicated in the **Figure 6.2 (b)**. The height of bubble #1 is about 40 nm while bubble #2 seems flatter with a height of around 14 nm, this can be observed from the height line profile of the cross section along the white line depicted in the AFM images.



* Bubble location: Between the graphene and the bottom hBN

Figure 6.1 The hBN/Graphene/hBN assembly. (a) OM images of the top hBN layer and the graphene flake. (b) OM images of the half stack containing the top hBN layer and the graphene). The enhanced contrast OM image is to check the presence of the bubbles in the stack area which is indicated in a yellow square. (c) OM images of the bottom hBN. (d) OM images of the final stack. A large amount of bubbles are seen in the stack area. The scale bars are 20 μm .

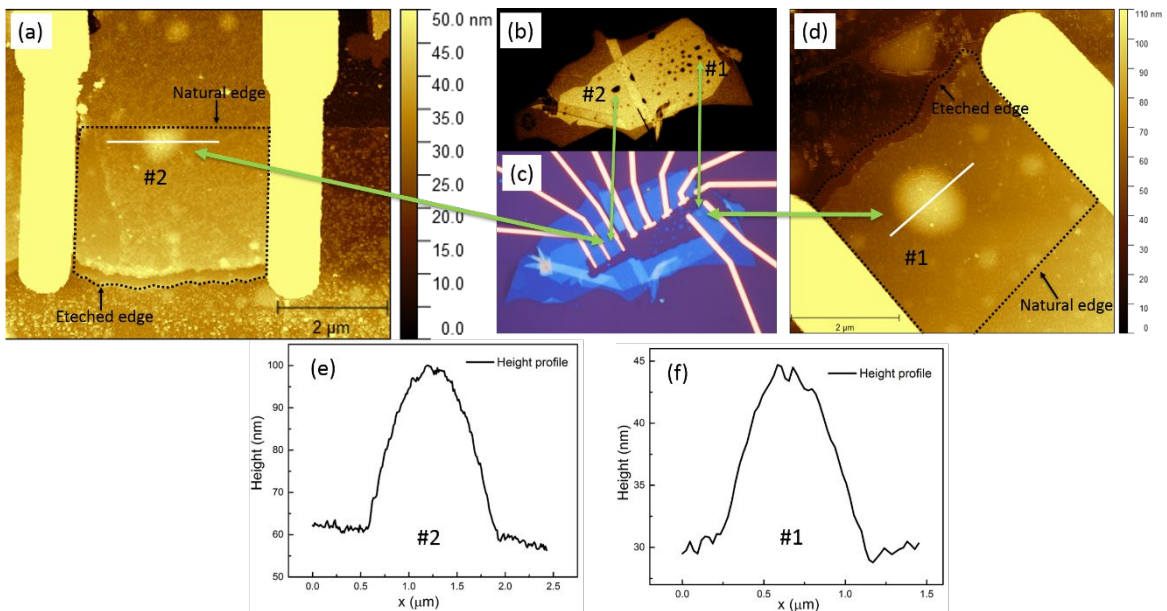


Figure 6.2 Bubble #1 and #2 before and after the device fabrication process. (a) and (d) are the topography of bubble #2 and bubble #1 individually. The outline of the graphene is indicated in dashed lines. OM images of the initial stack before and after device fabrication are shown in (b) and (c) separately. (e) and (f) are the height line profiles across bubble #2 and #1 along the white line depicted in (a) and (d).

Stack 2 was obtained using the same assembly method as the stack 1, it is therefore bubbles were also trapped between the graphene and the bottom hBN layer (**Figure 6.3 (b)**). It should be noted that bubble #3 are a group of small bubbles. Stack 3 was obtained by dropping the top hBN layer quickly on the graphene while slowly dropping the half stack (top hBN layer + graphene) on the bottom hBN layer. Bubble #4 was hence trapped between the top hBN layer and the graphene, see **Figure 6.3 (c)**.

A confocal Raman microscope was employed for characterising these bubbles with no prior surface processing. The characteristics of graphene were determined from the G, 2D and D peaks.

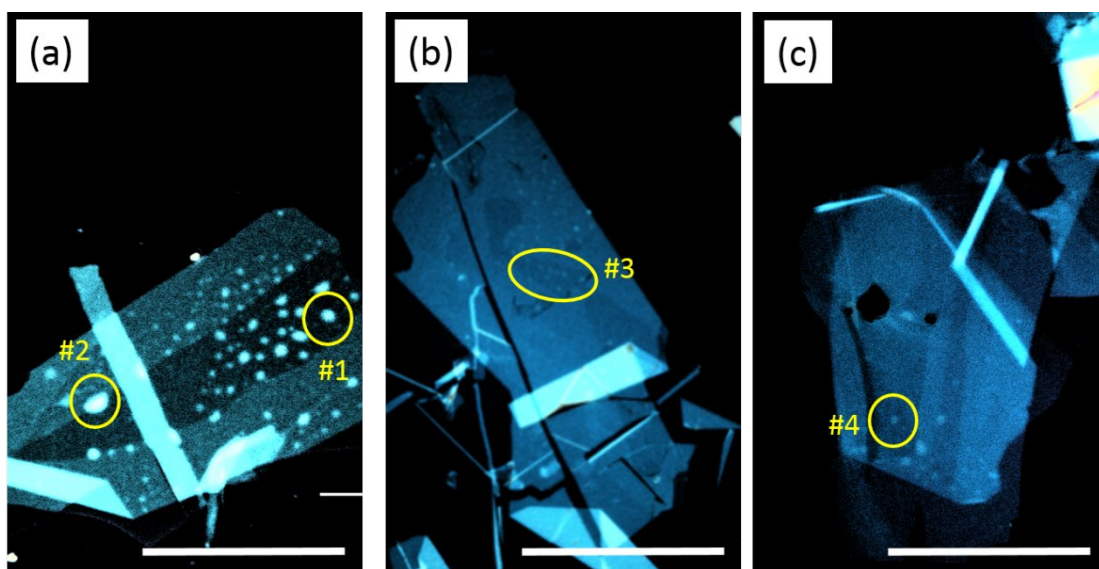


Figure 6.3 (a) OM image of the stack 1. Here bubble #1 and bubble #2 are both trapped below graphene. As one can see, bubble #1 is at the graphene edge while bubble #2 is in the central region. (b) OM image of the bubble #3, the small bubbles are observed in then stack2. (c) OM image of the stack 3. Bubble #4 is trapped above graphene. The scale bars 20 μm .

6.2 The Fitting Model Used for Raman Measurements

The Raman measurements were performed using a Renishaw inVia confocal Raman microscope at the National Physical Laboratory. A high confocality mode with an estimated spot size of 450 ± 10 nm at the full width at half maximum (FWHM) was selected, and a laser excitation of 532 nm ($E_L = 2.33$ eV) is used focusing on the surface through a 100 \times objective with numerical aperture of 0.85; the laser output energy was about 1 mW with an exposure time of 5 s, such that heating effects can be neglected[98], and an 1800 line/mm diffraction grating was used. All measurements were carried out in ambient at room temperature with a $\sim 40\%$ RH.

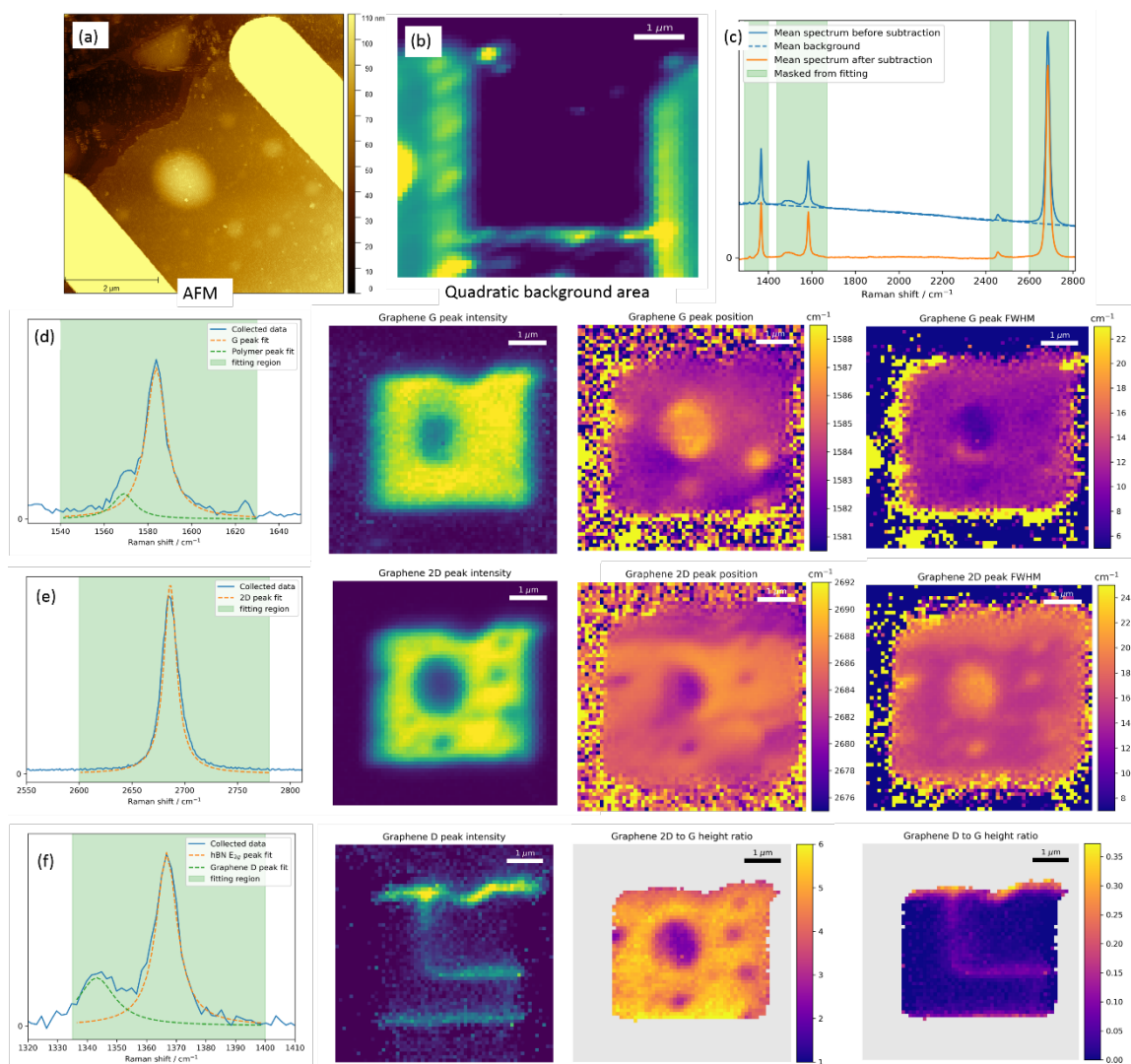


Figure 6.4 Fitting models and the procedures of Raman measurements. (a) The AFM image of bubble #1; (b) and (c) f show the background subtraction process. (d), (e) and (f) are the fitting process and results of G, 2D and D peak.

To extract the information of graphene from the Raman measurements, we did some subtraction and fittings. Examples of the process, based on the Raman measurements of bubble #1, are shown in **Figure 6.4**.

Firstly, sharp spikes in the data due to cosmic rays hitting the detector were first identified and removed from the maps by comparison with nearest neighbour spectra, then a quadratic background was fit and subtracted from each spectrum, with the regions containing studied peaks masked from the fitting process, as shown in **Figure 6.4 (b)** and **(c)**. The highest background in **(b)** comes from the electrode while the integrated background area shows background is the lowest on the graphene and SiO₂ area. Finally, peaks were fit to the regions of interest (**Figure 6.4 (d)-(f)**). All curve fitting was performed with nonlinear least squares regression and all Raman peaks were fitted with a single Lorentzian. Three regions accounting for graphene were individually fitted:

- (i) The graphene G peak, the fitting region is from 1540-1630 cm^{-1} . An additional single Lorentzian fixed at 1569 cm^{-1} was included in the fit to account for a Raman peak which appeared on the lower shoulder of the G peak in some regions, as shown in the spectrum of Figure 6.4 (d). We assume this peak comes from polymer contamination (i.e. PMMA from the device fabrication or PDMS from the stacking assembly). Raman maps of G peak in terms of the position as well as the intensity and FWHM are obtained after the fitting;
- (ii) The graphene 2D peak with a fitting region covering 2600-2780 cm^{-1} , as illustrated in Figure 6.4 (e), Raman maps including the intensity, position and FWHM of 2D peak are demonstrated in order;
- (iii) The hBN E2g peak and graphene D peak, which are shown in Figure 6.4 (f). The D peak and hBN peak are very close in wavenumber, but, thanks to their relatively constant Raman shifts, we were able to fix their locations, with D position at 1343.2 cm^{-1} and hBN position at 1366.8 cm^{-1} , to resolve each peak individually in the fitting process

All the Raman data analysis was performed using Renishaw WiRE 5.0 software.

6.3 Results and Discussion

Based on an approach of the correlation analysis between ω_G and ω_{2D} [82], [96], [97], see **Figure 3.4**, our Raman measurements with respect to the hydrostatic strain and the hole doping in the graphene were estimated by correlating the positions of the G and 2D peaks in graphene.

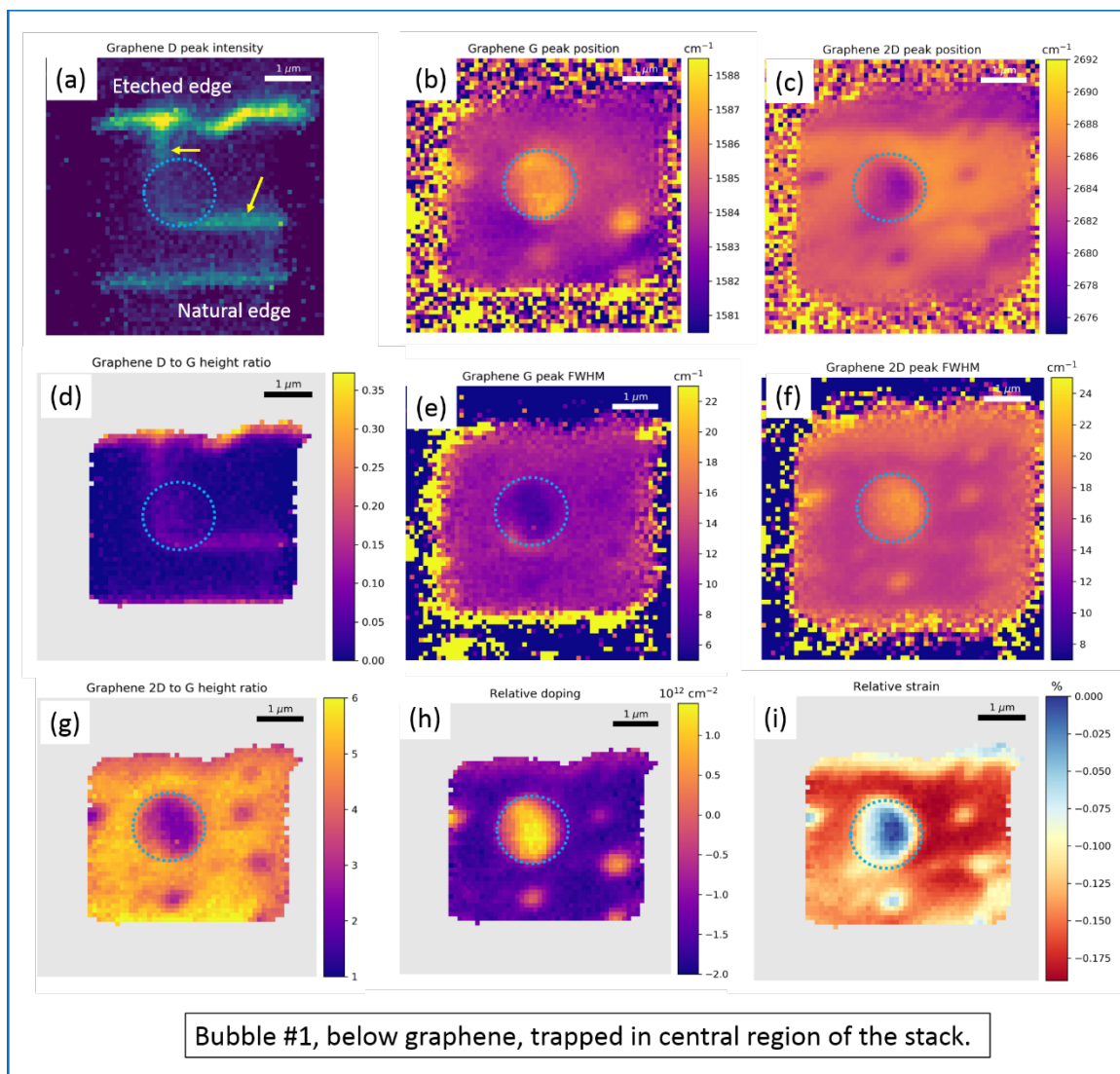


Figure 6.5 Raman measurements of bubble #1.

Maps of the Raman parameters for bubble #1 are shown in **Figure 6.5**. As discussed in [Chapter 3](#), the D-peak in graphene only presents when there are lattice defects[89], [91], and the ratio of D to G is usually used as an indicator of the presence of defects. From the Raman maps of bubble #1, defects are clearly seen at both the natural graphene edge and the etched graphene edge due to the bond disorders (**Figure 6.5 (a)** and **(d)**). The etching is responsible for the higher defect density due to O₂ induced functional groups and more disorders[93], [154]. Apart from that, a slightly higher defect density is present at the bubble area indicated with blue circle, which is attributed to strain-induced deformation of the graphene lattice[27]. One may notice the two accumulated defect-lines around bubble #1 which are indicated with yellow arrows, it is possibly related to the polymer which we will discuss later. The remaining area shows a very low D to G ratio below 0.05, which implies the encapsulated graphene to be mostly free of defects.

The distribution of graphene within the area of interest can be identified from the maps showing the intensities of the 2D and G peaks. It is noted the ratio of 2D to G is often used as an indicator of the quality and the number of layers in graphene[89], and the obtained ratio of this sample is $\sim 5-6$ which is typical for the hBN-encapsulated graphene. The bubble #1 in this heterostructure can be seen as the marked roughly circular region. It demonstrates an increased ω_G and a reduced ω_{2D} , see **Figure 6.5 (b)** and **(c)**. When we compare the bubble area with the bubble-free graphene area, we find something interesting.

As one can see from the Raman mappings of the G peak, in the bubble area, the increased ω_G corresponds to a decreased FWHM (G). Generally, the G peak is associated to the E_{2g} phonon at the Brillouin zone center, and the linewidth of ω_G is related to contributions from the stretching vibrations of carbon bonds in the rings, and such contribution indicates the electron-phonon coupling which is responsible for the FWHM (G). A sharp FWHM (G) is attributed to a homogenous broadening on the E_{2g} phonon induced by the phonon decaying into electron-hole pairs[92], [95], [155], [156]. Hence, the decreasing FWHM (G) in bubble #1 is related to a large electron-hole gap caused by a very high doping. It is reported that a FWHM (G) of $\sim 16 \text{ cm}^{-1}$ is close to a charge neutral state[155], [157]. The bubble-free area shows a FWHM (G) of around 15 cm^{-1} , which is ascribed the hBN shielding graphene from environmental effects. Whereas bubble #1 with the minimum FWHM (G) below $\sim 8 \text{ cm}^{-1}$ implies a very high doping in that area, which can be also observed from the Raman map of relative doping⁹ (**Figure 6.5 (h)**). The upshifts of ω_G are also arising from such doping. Now let us take a look at the relative changes in the graphene's hydrostatic strain of bubble #1 (**Figure 6.5 (i)**). The native strain in graphene is slightly more compressive, but bubble #1 shows the other way around which implies an intensely structural graphene. As discussed previously, tensile strain causes downshifts of the ω_G , doping results in upshifts of the ω_G , and both exist in the bubble area, but the FWHM(G) sharpening in the bubble area suggests that doping is dominated in bubble #1. While strain is dominating where FWHM (G) is maximal, and the variations of ω_G and ω_{2D} are related to the tensile strain (downshifts) or the compressive strain (upshifts)[57], [155].

⁹ It is noted that the negative and positive values of doping are estimated by correlating the position of G and 2D peaks, displaying the doping level relatively, and we contribute the negative value to an indication of pristine graphene[82].

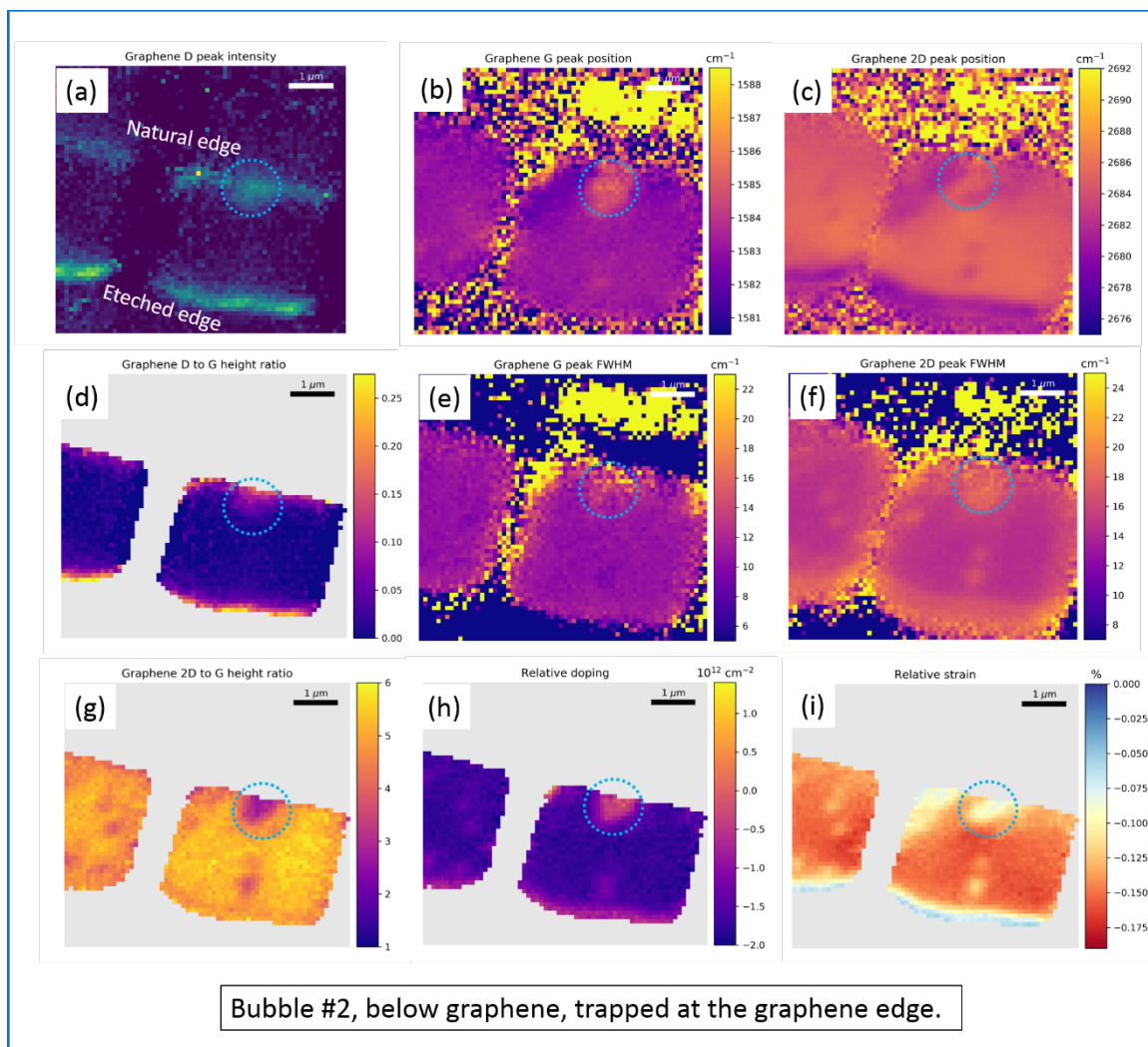


Figure 6.6 Raman measurements of bubble #2.

Similar to the bubble #1, bubble #2 demonstrates a higher defect density at the edge, and a very low D to G ratio in bubble-free area implying that the stack is of high quality, see **Figure 6.6**. The 2D to G ratio is typical for the hBN-encapsulated graphene. Bubble #2 also shows a higher doping than the rest bubble-free area. The native graphene is more compressive while the bubble area demonstrates a tensile strain. Based on our discussions on the competition between the doping and the strain, doping is also dominated in bubble #2, while the broadening FWHM of bubble #2 indicates the doping here is not as fierce as that in bubble #1, even though bubble #2 is almost three times higher than bubble #1 from the height profile of both bubbles. It is possibly related to the position of the bubbles, as illustrated in **Figure 6.3 (a)**. Bubble #2 is very close to the graphene edge, and only partly trapped below the graphene.

As earlier mentioned, we noticed the increased D-peak intensity at the areas above and below bubble #1, indicating an increased defect density (see solid rectangles in **Figure 6.7 (b)**). This could be caused by the polymer residues originating from the assembly. The

Raman map of the polymer distribution is shown in **Figure 6.7 (c)**, and indeed some contaminations seem to present. Correspondingly, some of the polymer sites exhibit a slightly increased tensile strain which suggests that graphene deforms around the contamination. But these polymers site do not match the area of the increased D-peak well. In the bubble itself, the D-peak intensity is only slightly increased, indicating the graphene lattice to be intact. On the other hand, panel **(d)** shows a strong increase of the strain in the bubble region, which implies bubble #1 is not affected by the polymers. Some spectra of the single points on the bubble #1 sample were collected, as shown in **Figure 6.8 (d)** and **(e)**. It is clearly to see the edge-induced D peak from A and E, and polymer peaks are visible in spectra D and E, which is as expected. We did not see clear D peak from the spectrum of B, considering the high tensile strength of graphene, which suggests the graphene structure is intact within the bubble.

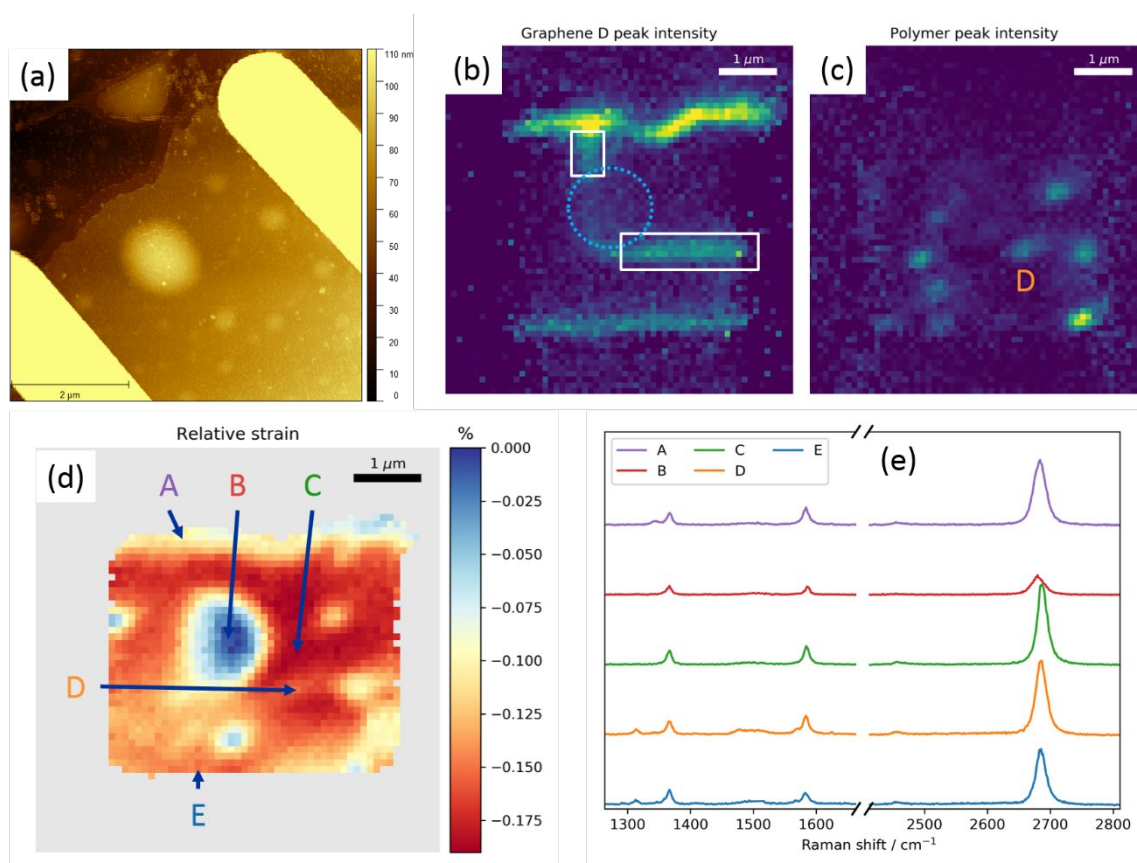


Figure 6.7 (a) AFM topography of bubble #1. (b) Raman map of the defect intensity in graphene. (c) polymer distribution map. (d) and (e) displays the Raman spectrum of the selected point on the sample.

Bubble #3 sample is a stack with a group of small bubbles (**Figure 6.8 (a)**) trapped between the graphene and the bottom hBN. Raman maps related to the graphene are shown in **Figure 6.8**. The graphene in this stack was torn apart from a large graphene flake (the assembly of this sample is illustrated in **Appendix B**), which may contribute to the higher density of the defects displayed at the unprocessed graphene edges. A higher contrast presented at the left middle region in the D area map is attributed to the accumulated

folds of the graphene, which can be observed from the optical image. The D to G ratio in this sample is overall low, including the bubble area, with a mean and standard deviation of 0.06 ± 0.13 and a median value of ~ 0.026 , which indicates that the graphene is mostly free of defects. The ratio of 2D to G has a mean and standard deviation of 6.6 ± 1.5 , just as expected for the hBN-encapsulated graphene. These bubbles show similar Raman characteristics as the single bubble #1 with ω_G increasing and FWHM(G) having a smaller value. Considering the offset caused by the dielectric screening from the substrate, we could only qualitatively compare bubble #3 sample with the previously discussed bubbles. There is a pronounced doping in the bubble regions which may relate to the increased number of contaminants trapped inside the bubbles. As one can view from the relative changes in the graphene's hydrostatic strain, the overall strain distribution tends to be tensile strain dominated, which is reasonable considering the high density of bubbles. To summarise, graphene above bubbles which are trapped between the graphene and the bottom hBN is doping dominated, and the doping level is very high giving the sharp FWHM (G) of $\sim 8 \text{ cm}^{-1}$.

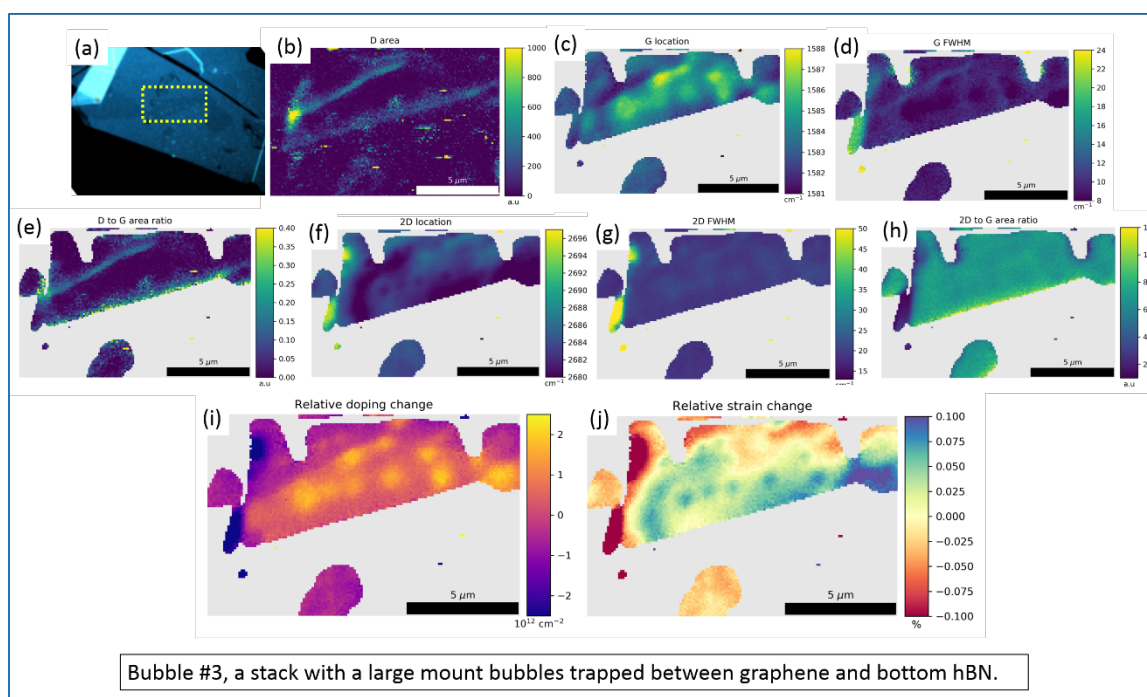


Figure 6.8 Maps of remaining graphene peak fitting results: (a) optical image of the Raman scanning area, indicated with a yellow square. G peak location (c) and FWHM (d). D peak to G peak ratio; 2D peak location (f) and FWHM (g). (h) is the 2D peak to G peak ratio, revealing the graphene is with high quality. (i) The estimated variation in hydrostatic strain in the single layer graphene across the heterostructure. (j) The estimated variation in hole doping in the single layer graphene across the heterostructure. In all maps, grey areas correspond to regions with no graphene.

Last, we investigated the bubble #4. Based on our hypothesis, the bubble is expected to be trapped between the top hBN layer and the graphene from the assembly (see **Figure 6.9 (a)-(c)**). As shown in the optical images of the initial graphene flake, there is one edge presented as a bilayer graphene, but considering our fitting being based on the presence of monolayer graphene, the Raman analysis is only carried out for the regions with single-layer.

Firstly, there are no indications for the presence of defects in bubble #4 from the D intensity map and D to G area ratio map. A mean and standard deviation of 0.01 ± 0.02 and a median value of 0.0 are obtained from the fitting procedure, which indicates that the graphene is almost completely free of defects. The D to G ratio at the edges are also very low, even considering the broken lattice symmetry at the edge. More supporting data can be found from the doping map (**Figure 6.10 (e)**) and the hydrostatic strain map (**Figure 6.10 (f)**). Secondly, the ratio of 2D to G is around 7, which indicates a high quality hBN/graphene/hBN stack. Last, we found bubble #4 is very different from the previous bubbles: rather than an increasing ω_G in bubble #1-#3, there is a decrement of $\sim 3 \text{ cm}^{-1}$ associated with ω_G in bubble #4. Additionally, the FWHM (G) of the bubble turns to be larger comparing with that in the bubble-free graphene area. All these converse changes imply that the tensile strain is mainly responsible for the G peak shift in the bubble area, see the **Figure 6.10 (f)**. The bubble #4 demonstrates a very intense tensile strain comparing with the nearly-strain-free graphene area, which is surprising for a bubble above the graphene. It is probably attributed a higher adhesion energy from the top hBN. As we discussed, the doping is discounted where the FWHM (G) is maximal and the shifts of the ω_G and the ω_{2D} are ascribed to the strain. Thus, for a bubble located above graphene, at least from the performed Raman measurements on bubble #4, the tensile strain is accounting for the bubble-induced modifications in the graphene structure.

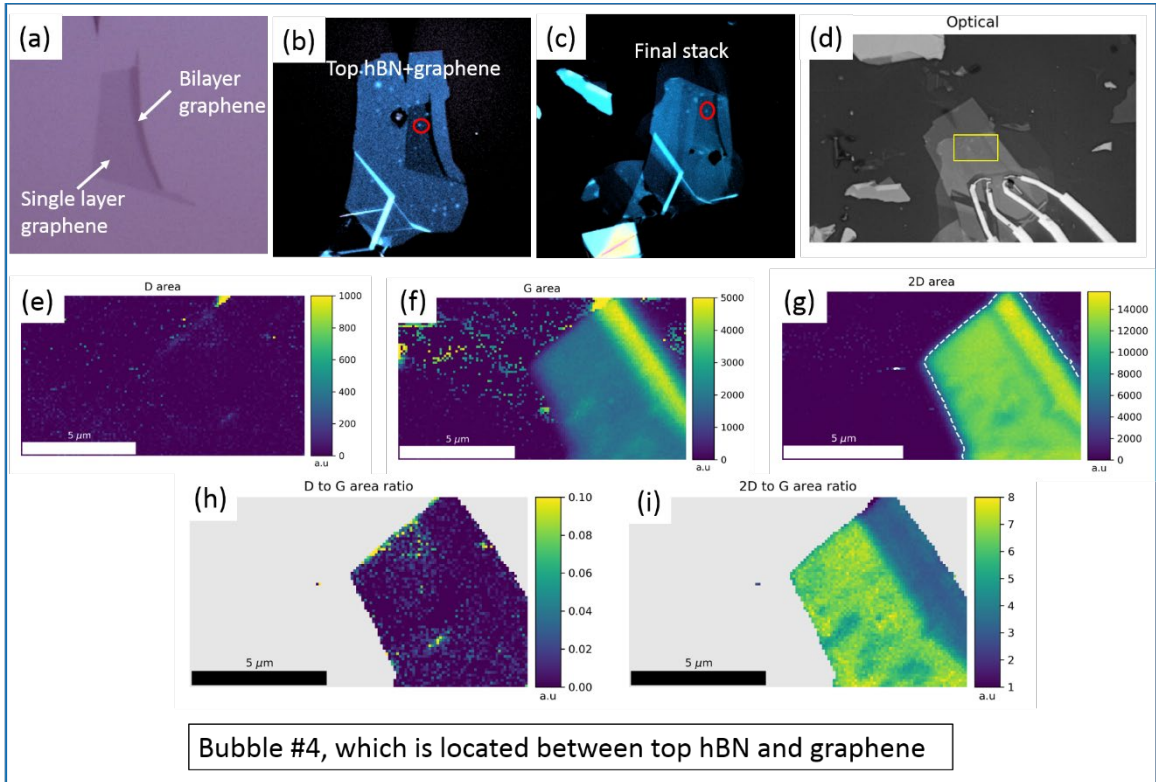


Figure 6.9 (a)-(c) Show the assembly of the bubble #4 sample, as indicated with the red circle, the bubble #4 was created when drop down the top hBN on graphene(b), and it is further presented in the full stack (c). (d) Optical image of the sample taken with the Raman microscope. (e)-(f) Maps of remaining graphene peak fitting results: the D area, the G peak area, the 2D peak area; and the D to G ration as well as the 2D to G ratio.

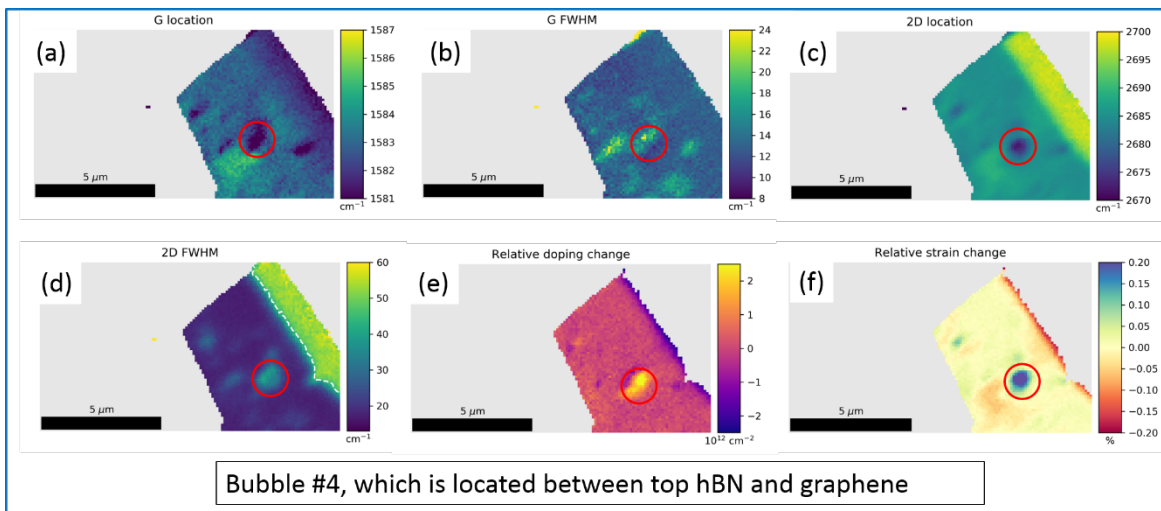


Figure 6.10 Maps of remaining graphene peak fitting results: G peak location (a) and FWHM (b), 2D peak location (c) and FWHM (d). (e) The estimated variation in hydrostatic strain in the single layer graphene across the heterostructure. (f) The estimated variation in hole doping in the single layer graphene across the heterostructure. In all maps, grey areas correspond to regions with no graphene.

6.4 Concluding Remarks

In this chapter, we investigated the bubble induced local stain and doping with a dependence on its location in hBN/graphene/hBN heterostructures using Raman characterization technique. Based on our hypothesis, the configuration of bubble can be controlled by the drop-down in the stacking assembly. From discussions on the Raman measurements, the doping and the tensile strain both contribute to the variations in the ω_G and the ω_{2D} . Since the doping upshifts the ω_G and the tensile strain causes a downshift on the ω_G , there is hence a competition between the both. We found that the doping is dominated in the bubbles which are trapped between the graphene and the bottom hBN layer. However, for the bubble trapped between the top hBN layer and the graphene, the strain is more pronounced. More Raman measurements on the bubbles trapped above the graphene should be further performed.

7 Thesis summary

7.1 Conclusions

In this thesis, I investigated the gate electrostatics of the graphene constrictions. A fringe field effects induced charge accumulation was visualized from a distribution of the local potential along the graphene channel via Kelvin Probe Force Microscopy (KPFM). First, an analytical calculation was described in Chapter 2. Using the Thomas-Fermi model, a relation between the electrostatically-induced charge density and the electrostatic potential was analytically solved. The electrostatic potential profile was further solved numerically using the COMSOL Multiphysics. Second, KPFM measurements were performed on different back gated graphene constrictions in both vacuum and the air ambient. Three different graphene edges including unprocessed edge, RIE-etched graphene edge and PA-etched graphene edge were focused for the observation of the charge accumulation. AM-KPFM and FM-KPFM have been used for the surface potential mapping. A noticeable potential enhancement caused by the charge accumulation was often seen at the natural graphene edge. However, the occurrence was observed at the RIE-etched edge only in vacuum and never been seen at the PA-etched edge. Based on our discussions, presence of the charge accumulation is largely influenced by the edge disorder and the employed KPFM technique. Third, our results were qualitatively consistent with the analytical calculation. Considering the facts of the surficial contaminations, edge disorders, measuring environment and KPFM working as a surface characterization technique, it is hard to obtain a quantitatively study on the gate electrostatics, which is not reliable enough to obtain the charge density using the measured surface potential. However, the work gives a specific insight into the fundamental physics with respect to the gate electrostatics of the 2D material graphene.

Additionally, we accidentally observed that the surface potential of the graphene bubbles in vdW heterostructures presents inhomogeneous when we conducted the previous study via KPFM. The local potential over all the bubble area slightly changes when a gate voltage is applied. It is therefore we carried out the Raman study on graphene bubbles. In Chapter 6, bubbles induced strain and doping in vdW heterostructures with a dependence on the location was discussed. By controlling the assembling process, bubble can be configured at different interfaces: Bubbles locates between top hBN and graphene or locates between graphene and bottom hBN. The Raman measurements with respect to the hydrostatic strain and the hole doping in the bubbles were estimated by correlating the position of the G and 2D peaks in graphene. In the case of bubbles located below graphene plane, the bubble area presented doping dominated. A minimum FWHM (G) of $\sim 8 \text{ cm}^{-1}$ was observed in the bubble area which implied a very high doping. However, as for the case of bubbles located above graphene plane, surprisingly, a pronounced tensile strain was observed. The tensile strain turned out to be dominated which can be observed from the variations of ω_G and ω_{2D} . From this point of view, the Raman may give a new perspective on the stain engineering in graphene.

7.2 Outlook

Regarding the study of gate electrostatics in narrow graphene devices, although the charge accumulation has been visualized using KPFM, there are works which I here strongly suggest for future studies with respect to this project. First, the trace and retrace issue should be solved. The study can be carried out by keeping the position of the probe to be either parallel (with a probe-surface angle of 0° or 180°) or perpendicular to the graphene constriction (with a probe-surface angle of 90° or 270°). Moreover, minimizing the size of the electrode is also suggested and the probe is better not be tilted during the scanning. Second, a few more KPFM measurements on the hBN encapsulated graphene semiconstriction should be performed in both vacuum and the ambient environment. A surface cleaning is highly suggested. The charge density distribution across the contribution may be approachable by this way. Third, giving the fact of KPFM being as surface characterization technique, an open hBN supported graphene semiconstriction is of interest for a quantitative investigation on the charge density distribution across the channel. Last, given the charge accumulation is also sensitive to the channel width, it is therefore graphene constrictions with various width are also suggested to be further investigated. Additionally, it would be also interesting to visualize the enhanced carrier transport in scanning gate microscopy and control the electron transport using a magnetic field. The Raman study on the graphene bubbles, has not been explicitly solved from the demonstrated measurements. More Raman measurements are necessary. It is also hard to conclude the position simply from the stacking assembly using OM. Last, KPFM is suggested to be further carried out on the bubbles with respect to the location.

Appendix A

Electrostatic Charge Distribution in Wide Graphene device:

As we discussed in Chapter 2 and Chapter 5, the fringe field effect induced charge accumulation shows a dependence on the device dimension. A $3\ \mu\text{m}$ wide graphene strip which is encapsulated in hBN layers were measured using FM-KPFM in vacuum, the electrostatic potential maps are shown in Figure A.2, and the potential line profiles across the strip is shown in Figure A.3. There is no charge accumulation observed for the wide graphene device, since the fringe field effect can be neglected in such case.

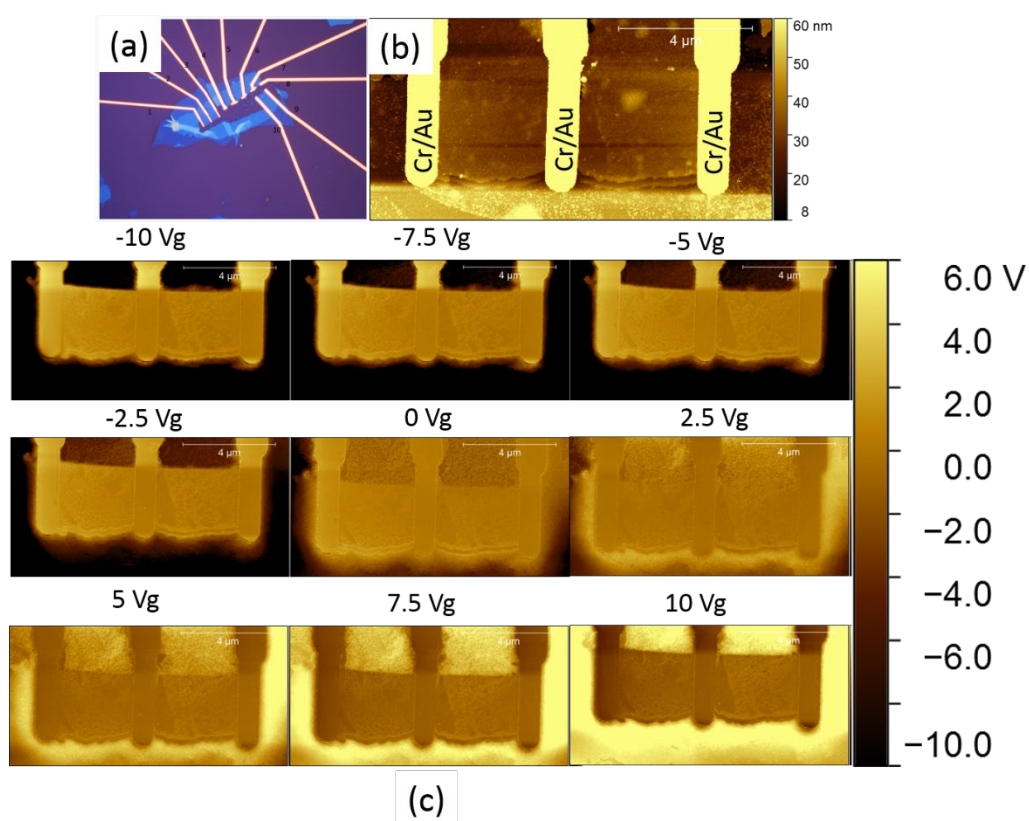


Figure A.2 (a) the optical image of the device, it is located between electrode 1, 2 and 3. (b) The AFM topography of the wide graphene strip device. (c) the surface potential maps with different applied gate bias. The KPFM was performed in vacuum.

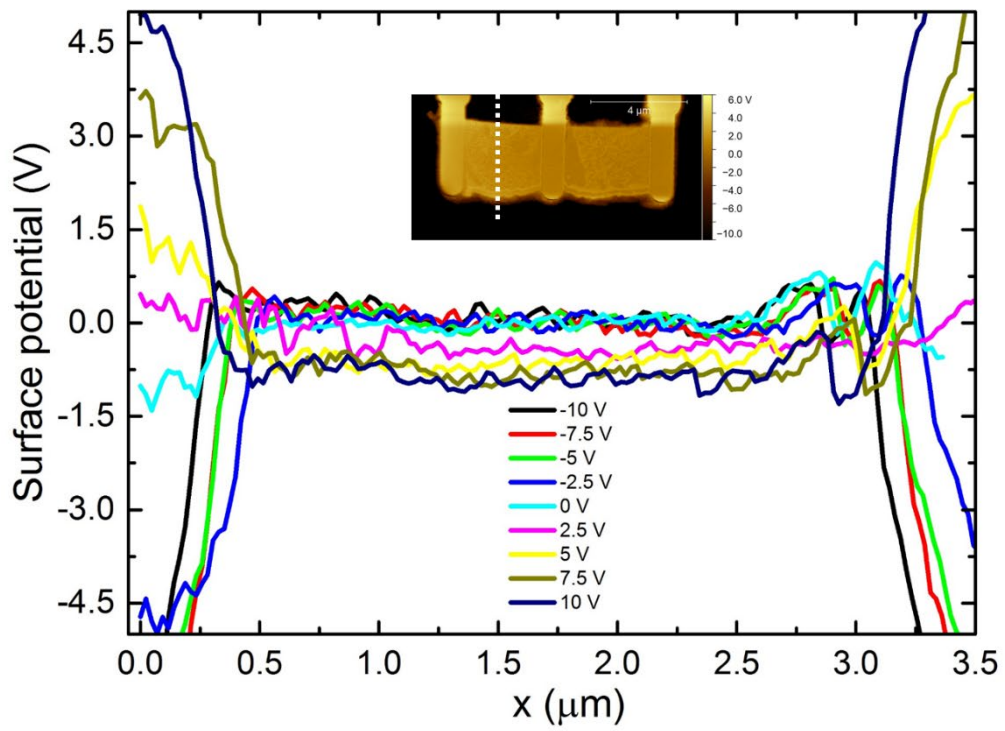


Figure A.3 The surface potential line profiles across the wide graphene channel, the cross section is indicated in the inset. No charge accumulation is observed in the wide graphene strip device.

Appendix B

The vdW heterostructure assembly process (Figure B.1) for sample bubble #3: (a) is the optical image taken with the Raman microscope. (b) is the OM of the graphene flake. It is clear to see some folds at the edge. In figure (c), the half stack is present free of bubbles. However, the graphene flake was torn apart during the last transfer process, which can be seen by comparing (b) and (c). A number of bubbles were trapped in the last transfer process as well.

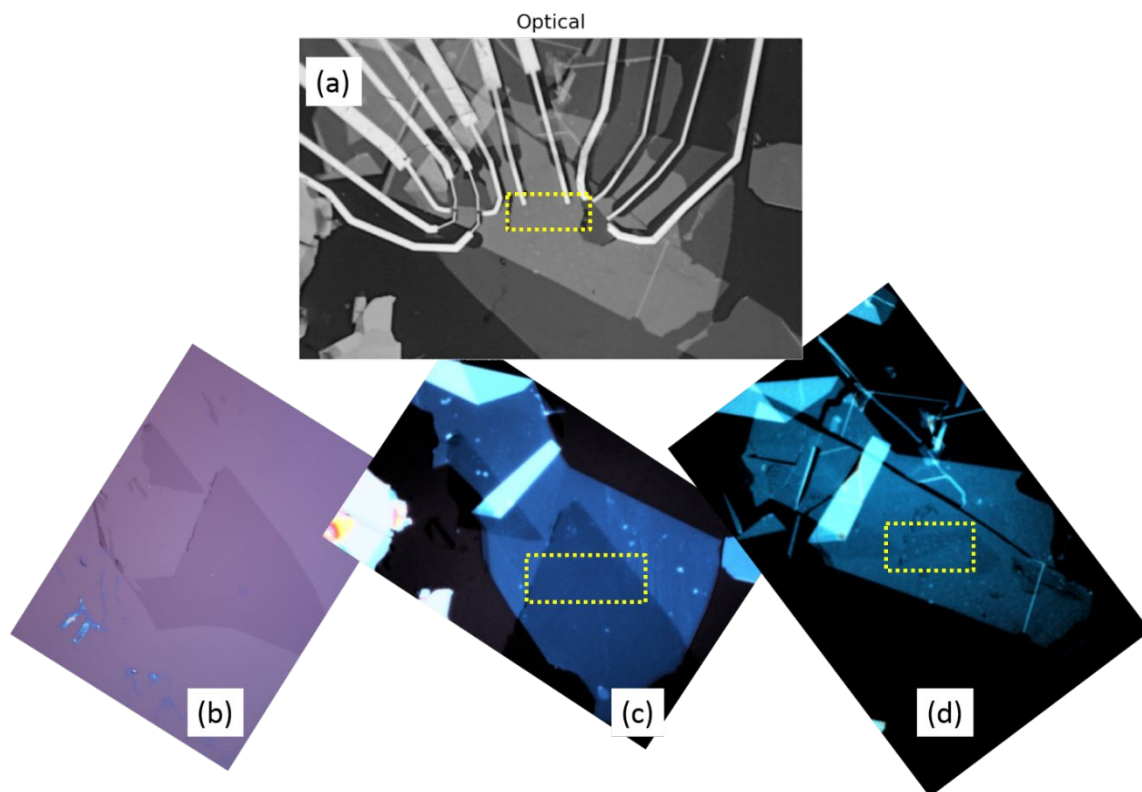


Figure B.1 The vdW heterostructure assembly process for sample bubble #3.

The vdW heterostructure assembly process (Figure B.2) for sample bubble #4 where the bubble is trapped between top hBN and graphene.

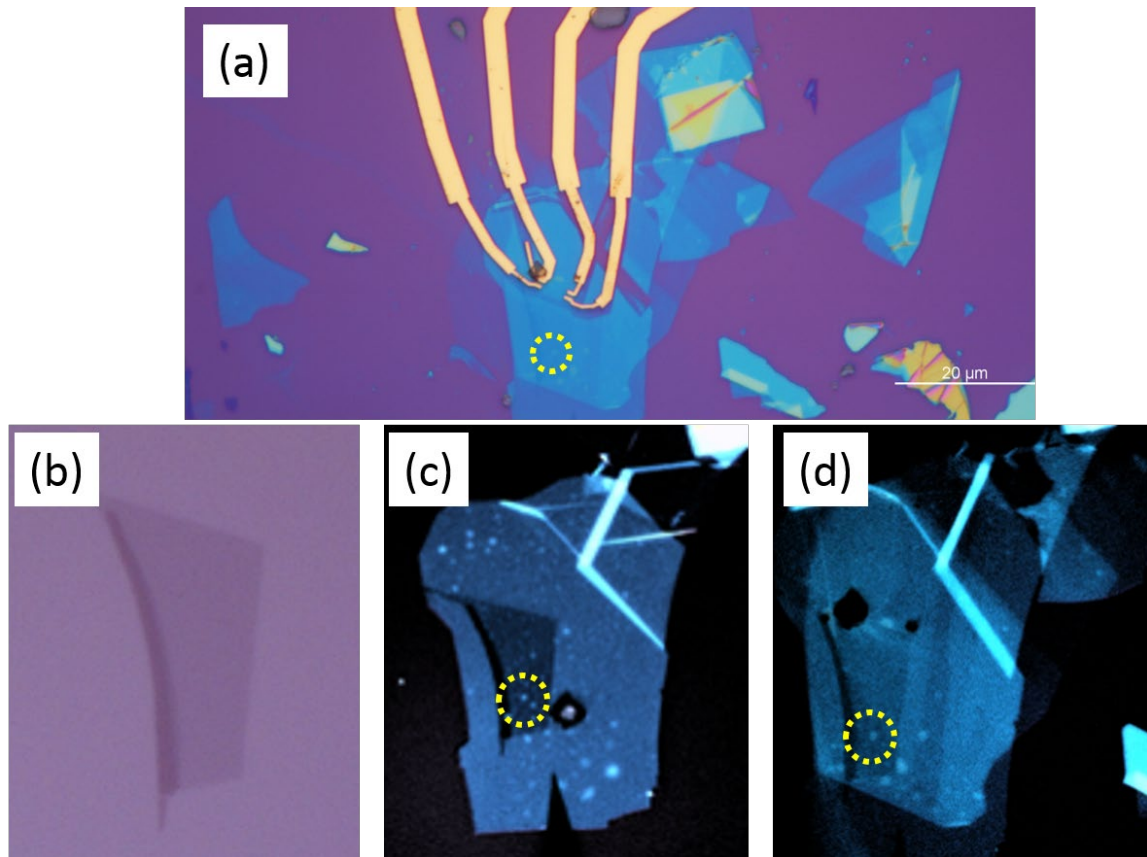


Figure B.2 The vdW heterostructure assembly process for sample bubble #3. (a) OM of the device. (b) The mechanically exfoliated graphene flake. (c) OM image of the half stack. The target bubble #4 is indicated with the yellow circle. (d) The bubble #4 is present after the full stack achieved, it can be observed from the OM image.

Appendix C

The KPFM measurements of graphene semiconstriction elec2-3 obtained from the backward scans were not saved, because we have not observed the discrepancies between the trace data and the retrace data, this can be observed from the photo below.

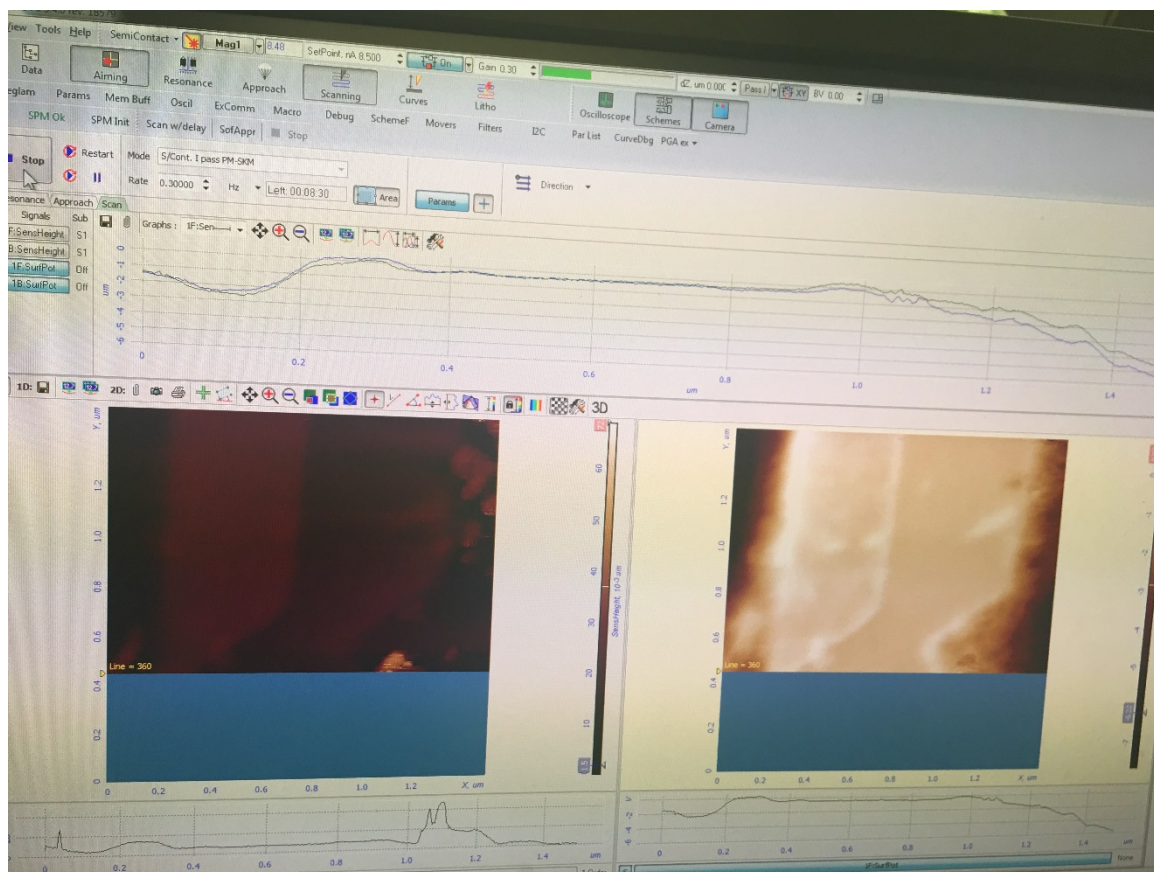


Figure C.1 The photo here captures the surface potential of the forward scan (blue line) and the backward scan (green line) in semiconstriction elec2-3. The trace and retrace issue is not observed from the picture.

Bibliography

- [1] K. S. Novoselov, A. K. Geim, S. V. Morozov, D. Jiang, 1 Y. Zhang, S. V. Dubonos, I. V. Grigorieva, "Electric Field Effect in Atomically Thin Carbon Films," *Science (80-)*, vol. 666, no. 54, pp. 37–66, 2004.
- [2] D. G. Papageorgiou, I. A. Kinloch, and R. J. Young, "Mechanical properties of graphene and graphene-based nanocomposites," *Prog. Mater. Sci.*, vol. 90, pp. 75–127, 2017.
- [3] H. Y. Nan, Z. H. Ni, J. Wang, Z. Zafar, Z. X. Shi, and Y. Y. Wang, "The thermal stability of graphene in air investigated by Raman spectroscopy," *J. Raman Spectrosc.*, vol. 44, no. 7, pp. 1018–1021, 2013.
- [4] R. K. Singh Raman and A. Tiwari, "Graphene: The thinnest known coating for corrosion protection," *Jom*, vol. 66, no. 4, pp. 637–642, 2014.
- [5] S. V. Morozov *et al.*, "Giant intrinsic carrier mobilities in graphene and its bilayer," *Phys. Rev. Lett.*, vol. 100, no. 1, pp. 11–14, 2008.
- [6] R. Murali, "Graphene transistors," *Graphene Nanoelectron. From Mater. to Circuits*, vol. 9781461405, no. 7, pp. 51–91, 2012.
- [7] "The International Technology Roadmap for Semiconductors,." [Online]. Available: <http://www.itrs.net>.
- [8] M. C. Lemme, S. Member, T. J. Echtermeyer, M. Baus, and H. Kurz, "A Graphene Field-Effect Device," vol. 28, no. 4, pp. 282–284, 2007.
- [9] J. Fernández-Rossier, J. J. Palacios, and L. Brey, "Electronic structure of gated graphene and graphene ribbons," *Phys. Rev. B - Condens. Matter Mater. Phys.*, vol. 75, no. 20, pp. 1–8, 2007.
- [10] P. G. Silvestrov and K. B. Efetov, "Charge accumulation at the boundaries of a graphene strip induced by a gate voltage: Electrostatic approach," *Phys. Rev. B - Condens. Matter Mater. Phys.*, vol. 77, no. 15, pp. 1–5, 2008.
- [11] A. A. Shylau, J. W. Kłos, and I. V. Zozoulenko, "Capacitance of graphene nanoribbons," *Phys. Rev. B - Condens. Matter Mater. Phys.*, vol. 80, no. 20, pp. 1–9, 2009.
- [12] J. M. Caridad, S. R. Power, A. A. Shylau, L. Gammelgaard, A. P. Jauho, and P. Bøggild, "Gate electrostatics and quantum capacitance in ballistic graphene devices," *Phys. Rev. B*, vol. 99, no. 19, pp. 1–7, 2019.
- [13] F. T. Vasko and I. V. Zozoulenko, "Conductivity of a graphene strip: Width and gate-voltage dependencies," *Appl. Phys. Lett.*, vol. 97, no. 9, pp. 1–4, 2010.
- [14] P. J. Zomer *et al.*, "Quantum Hall transport as a probe of capacitance profile at graphene edges," *Appl. Phys. Lett.*, vol. 102, no. 1, p. 013106, 2013.
- [15] J. Chae *et al.*, "Enhanced carrier transport along edges of graphene devices," *Nano*

- Lett.*, vol. 12, no. 4, pp. 1839–1844, 2012.
- [16] J. M. Caridad *et al.*, “Conductance quantization suppression in the quantum Hall regime,” *Nat. Commun.*, vol. 9, no. 1, pp. 1–6, 2018.
- [17] J. Guo, Y. Yoon, and Y. Ouyang, “Gate electrostatics and quantum capacitance of graphene nanoribbons,” *Nano Lett.*, vol. 7, no. 7, pp. 1935–1940, 2007.
- [18] Z. Wang and R. W. Scharstein, “Electrostatics of graphene: Charge distribution and capacitance,” *Chem. Phys. Lett.*, vol. 489, no. 4–6, pp. 229–236, 2010.
- [19] L. Colombo *et al.*, “Effective mobility of single-layer graphene transistors as a function of channel dimensions,” *J. Appl. Phys.*, vol. 109, no. 10, p. 104511, 2011.
- [20] J. Guo, Y. Yoon, and Y. Ouyang, “Gate electrostatics and quantum capacitance of graphene nanoribbons,” *Nano Lett.*, vol. 7, no. 7, pp. 1935–1940, 2007.
- [21] E. R. Mucciolo, A. H. Castro Neto, and C. H. Lewenkopf, “Conductance quantization and transport gaps in disordered graphene nanoribbons,” *Phys. Rev. B - Condens. Matter Mater. Phys.*, vol. 79, no. 7, pp. 1–5, 2009.
- [22] J. M. Caridad, S. R. Power, A. A. Shylau, L. Gammelgaard, A. P. Jauho, and P. Bøggild, “Gate electrostatics and quantum capacitance in ballistic graphene devices,” *Phys. Rev. B*, vol. 99, no. 19, pp. 1–13, 2019.
- [23] N. a Gershenfeld *et al.*, “Strain-Induced Pseudo-Magnetic Fields Greater Than 300 Tesla in Graphene Nanobubbles,” *Science (80-.)*, no. July, pp. 544–547, 2010.
- [24] G. F. E. Stolyarova, D. Stolyarov, K. Bolotin, | S. Ryu, L. Liu, K. T. Rim, M. Klima, ⊥ M. Hybertsen, I. Pogorelsky, I. Pavlishin, K. Kusche, J. Hone, ⊥ P. Kim, H. L. Stormer, O V. Yakimenko, “Observation of graphene bubbles and effective mass transport under graphene films,” *Nano Lett.*, vol. 9, no. 1, pp. 332–337, 2009.
- [25] J. Zabel *et al.*, “Raman spectroscopy of graphene and bilayer under biaxial strain: Bubbles and balloons,” *Nano Lett.*, vol. 12, no. 2, pp. 617–621, 2012.
- [26] A. V. Tyurnina *et al.*, “Strained Bubbles in van der Waals Heterostructures as Local Emitters of Photoluminescence with Adjustable Wavelength,” *ACS Photonics*, vol. 6, no. 2, pp. 516–524, 2019.
- [27] N. Leconte *et al.*, “Graphene bubbles and their role in graphene quantum transport,” *Nanoscale*, vol. 9, no. 18, pp. 6041–6047, 2017.
- [28] W. Pan *et al.*, “Biaxial compressive strain engineering in graphene/boron nitride heterostructures,” *Sci. Rep.*, vol. 2, pp. 2–7, 2012.
- [29] G. Zamborlini *et al.*, “Nanobubbles at GPa Pressure under Graphene,” *Nano Lett.*, vol. 15, no. 9, pp. 6162–6169, 2015.
- [30] R. Larciprete *et al.*, “Self-Assembly of Graphene Nanoblisters Sealed to a Bare Metal Surface,” *Nano Lett.*, vol. 16, no. 3, pp. 1808–1817, 2016.
- [31] R. Mu *et al.*, “Visualizing chemical reactions confined under graphene,” *Angew.*

- Chemie - Int. Ed.*, vol. 51, no. 20, pp. 4856–4859, 2012.
- [32] X. Y. Shan, G. Zhou, L. C. Yin, W. J. Yu, F. Li, and H. M. Cheng, “Visualizing the roles of graphene for excellent lithium storage,” *J. Mater. Chem. A*, vol. 2, no. 42, pp. 17808–17814, 2014.
- [33] J. H. Fendler *et al.*, “High-Resolution EM of Colloidal Nanocrystal Growth Using Graphene Liquid Cells,” no. April, pp. 61–65, 2012.
- [34] N. Petkov, “In Situ Real-Time TEM Reveals Growth, Transformation and Function in One-Dimensional Nanoscale Materials: From a Nanotechnology Perspective,” *ISRN Nanotechnol.*, vol. 2013, pp. 1–21, 2013.
- [35] P. R. Whelan, X. Zhao, I. Pasternak, W. Strupinski, P. U. Jepsen, and P. Bøggild, “Non-contact mobility measurements of graphene on silicon carbide,” *Microelectron. Eng.*, vol. 212, no. November 2018, pp. 9–12, 2019.
- [36] N. A. Spaldin, “Fundamental Materials Research and the Course of Human Civilization,” no. 2, pp. 11–15, 2017.
- [37] O. For, “International Roadmap for Devices and Systems” 2016 Edition More Moore, 2016.
- [38] R. W. Keyes, “Physical limits of silicon transistors and circuits,” *Reports Prog. Phys.*, vol. 68, no. 12, pp. 2701–2746, 2005.
- [39] G. A.K and N. K.S, “The rise of graphene,” *Nat. Mater.*, vol. 6, pp. 183–191, 2007.
- [40] N. A. A. Ghany, S. A. Elsherif, and H. T. Handal, “Revolution of Graphene for different applications: State-of-the-art,” *Surfaces and Interfaces*, vol. 9, no. June, pp. 93–106, 2017.
- [41] K. S. Novoselov *et al.*, “Two-dimensional gas of massless Dirac fermions in graphene,” *Nature*, vol. 438, no. 7065, pp. 197–200, 2005.
- [42] C. Lee, X. Wei, J. W. Kysar, and J. Hone, “Measurement of the Elastic Properties and Intrinsic Strength of Monolayer Graphene,” vol. 321, no. July, pp. 385–388, 2008.
- [43] A. S. Mayorov, R. V. Gorbachev, S. V. Morozov, L. Britnell and School L. A. Ponomarenko, P. Blake, K. S. Novoselov¹, K. Watanabe, T. Taniguchi⁴, A. K. Geim, “Micrometer-Scale Ballistic Transport in Encapsulated Graphene at Room Temperature,” *Main*, pp. 9–12.
- [44] L. Wang *et al.*, “One-Dimensional Electrical Contact to,” *Sci. (New York, N.Y.)*432, vol. 342, no. November, pp. 614–617, 2013.
- [45] X. Du, I. Skachko, A. Barker, and E. Y. Andrei, “Approaching ballistic transport in suspended graphene,” *Nat. Nanotechnol.*, vol. 3, no. 8, pp. 491–5, 2008.
- [46] R. R. Dammel, “The electronic properties of graphene,” in *Reviews of Modern Physics*, vol. 81, no. 1, p. 216.
- [47] D. R. Cooper *et al.*, “Experimental Review of Graphene,” *ISRN Condens. Matter*

- Phys.*, vol. 2012, pp. 1–56, 2012.
- [48] G. Yang, L. Li, W. B. Lee, and M. C. Ng, “Structure of graphene and its disorders: a review,” *Sci. Technol. Adv. Mater.*, vol. 19, no. 1, pp. 613–648, 2018.
- [49] C. Bena and G. M. Baux, “Remarks on the tight-binding model of graphene,” *New J. Phys.*, vol. 11, 2009.
- [50] Jean-Noël Fuchs; Mark Oliver Goerbig; Marek Potemski, “Des électrons sans masse dans une feuille de carbone.”
- [51] K. S. Novoselov *et al.*, “Electronic properties of graphene,” *Phys. Status Solidi Basic Res.*, vol. 244, no. 11, pp. 4106–4111, 2007.
- [52] G. W. Semenoff, “Condensed-Matter simulation of a three-Dimensional anomaly,” *Phys. Rev. Lett.*, vol. 53, no. 26, pp. 2449–2452, 1984.
- [53] J.-N. Fuchs, “Dirac fermions in graphene and analogues: magnetic field and topological properties,” 2013.
- [54] K. S. Novoselov *et al.*, “Electronic properties of graphene,” *Phys. Status Solidi Basic Res.*, vol. 244, no. 11, pp. 4106–4111, 2007.
- [55] C. R. Dean *et al.*, “Boron nitride substrates for high-quality graphene electronics,” *Nat. Nanotechnol.*, vol. 5, no. 10, pp. 722–726, 2010.
- [56] M. Lafkioti *et al.*, “Graphene on a hydrophobic substrate: Doping reduction and hysteresis suppression under ambient conditions,” *Nano Lett.*, vol. 10, no. 4, pp. 1149–1153, 2010.
- [57] L. Banszerus *et al.*, “Identifying suitable substrates for high-quality graphene-based heterostructures,” *2D Mater.*, vol. 4, no. 2, p. aa5b0f, 2017.
- [58] C. R. Dean *et al.*, “Boron nitride substrates for high-quality graphene electronics,” *Nat. Nanotechnol.*, vol. 5, no. 10, pp. 722–6, 2010.
- [59] T. O. Wehling, M. I. Katsnelson, and A. I. Lichtenstein, “Adsorbates on graphene: Impurity states and electron scattering,” *Chem. Phys. Lett.*, vol. 476, no. 4–6, pp. 125–134, 2009.
- [60] Y. Huang *et al.*, “Reliable Exfoliation of Large-Area High-Quality Flakes of Graphene and Other Two-Dimensional Materials,” *ACS Nano*, vol. 9, no. 11, pp. 10612–10620, 2015.
- [61] K. Kim, J. Y. Choi, T. Kim, S. H. Cho, and H. J. Chung, “A role for graphene in silicon-based semiconductor devices,” *Nature*, vol. 479, no. 7373, pp. 338–344, 2011.
- [62] Y.-J. Yu, Y. Zhao, S. Ryu, L. E. Brus, K. S. Kim, and P. Kim, “Tuning the graphene work function by electric field effect,” *Nano Lett.*, vol. 9, no. 10, pp. 3430–4, 2009.
- [63] K. S. Novoselov, A. K. Geim, F. Guinea, N. M. R. Peres, and A. H. Castro Neto, “The electronic properties of graphene,” *Rev. Mod. Phys.*, vol. 81, no. 1, pp. 109–162, 2009.

- [64] C. Musumeci, "Advanced Scanning Probe Microscopy of Graphene and Other 2D Materials," *Crystals*, vol. 7, no. 7, p. 216, 2017.
- [65] R. Garg, N. Dutta, and N. Choudhury, "Work Function Engineering of Graphene," *Nanomaterials*, vol. 4, no. 2, pp. 267–300, 2014.
- [66] D. S. L. Abergel, V. Apalkov, J. Berashevich, K. Ziegler, and T. Chakraborty, "Properties of graphene: A theoretical perspective," *Adv. Phys.*, vol. 59, no. 4, pp. 261–482, 2010.
- [67] R. Beams, L. Gustavo Cançado, and L. Novotny, "Raman characterization of defects and dopants in graphene," *J. Phys. Condens. Matter*, vol. 27, no. 8, 2015.
- [68] R. R. Dammel, "Disorder and electronic transport in graphene," in *Journal of Physics Condensed Matter*, vol. 22, no. 27, p. 216.
- [69] R. Nouchi, M. Shiraishi, and Y. Suzuki, "Transfer characteristics in graphene field-effect transistors with Co contacts," *Appl. Phys. Lett.*, vol. 93, no. 15, pp. 18–21, 2008.
- [70] M. F. Craciun, S. Russo, M. Yamamoto, and S. Tarucha, "Tuneable electronic properties in graphene," *Nano Today*, vol. 6, no. 1, pp. 42–60, 2011.
- [71] M. Nakamura, "a Strip Capacitor," vol. 13, no. 2, 1990.
- [72] 2 S Haroche *et al.*, "Electric Field Effect in Atomically Thin Carbon Films," *Nat. Phys.* vol. 666, no. 54, pp. 37–66, 2004.
- [73] S. Das Sarma, S. Adam, E. H. Hwang, and E. Rossi, "Electronic transport in two-dimensional graphene," *Rev. Mod. Phys.*, vol. 83, no. 2, pp. 407–470, 2011.
- [74] L. Brey and H. A. Fertig, "Linear response and the Thomas-Fermi approximation in undoped graphene," *Phys. Rev. B - Condens. Matter Mater. Phys.*, vol. 80, no. 3, 2009.
- [75] T. Andrijauskas, A. A. Shylau, and I. V. Zozoulenko, "Thomas-Fermi and Poisson modeling of gate electrostatics in graphene nanoribbon," *Lith. J. Phys.*, vol. 52, no. 1, pp. 63–69, 2012.
- [76] K. Yue *et al.*, "Analytical methods for the mechanics of graphene bubbles Analytical methods for the mechanics of graphene bubbles," vol. 083512, no. May 2015, 2014.
- [77] E. Khestanova, F. Guinea, L. Fumagalli, A. K. Geim, and I. V. Grigorieva, "Universal shape and pressure inside bubbles appearing in van der Waals heterostructures," *Nat. Commun.*, vol. 7, pp. 1–10, 2016.
- [78] M. Settnes, S. R. Power, J. Lin, D. H. Petersen, and A. P. Jauho, "Bubbles in graphene - A computational study," *J. Phys. Conf. Ser.*, vol. 647, no. 1, 2015.
- [79] School T. Georgiou¹, L. Britnell, P. Blake, R. Gorbachev, A. Gholinia, A. K. Geim, C. Casiraghi, K. S. Novoselov¹, "Graphene bubbles with controllable curvature," *Appl. Phys. Lett.*, vol. 99, no. 9, pp. 5–7, 2011.

- [80] E. Iakovlev, P. Zhilyaev, and I. Akhatov, "Atomistic study of the solid state inside graphene nanobubbles," *Sci. Rep.*, vol. 7, no. 1, pp. 1–7, 2017.
- [81] P. Wang, W. Gao, K. Yue, Z. Cao, K. M. Liechti, and R. Huang, "Mechanics of graphene bubbles," *13th Int. Conf. Fract. 2013, ICF 2013*, vol. 6, no. January 2016, 2013.
- [82] T. Vincent *et al.*, "Probing the nanoscale origin of strain and doping in graphene-hBN heterostructures," *2D Mater.*, vol. 6, no. 1, 2019.
- [83] S. J. Haigh *et al.*, "Cross-sectional imaging of individual layers and buried interfaces of graphene-based heterostructures and superlattices," *Nat. Mater.*, vol. 11, no. 9, pp. 764–7, 2012.
- [84] M. Yankowitz, Q. Ma, P. Jarillo-Herrero, and B. J. LeRoy, "van der Waals heterostructures combining graphene and hexagonal boron nitride," *Nat. Rev. Phys.*, vol. 1, no. 2, pp. 112–125, 2019.
- [85] A. K. Geim and I. V Grigorieva, "Van der Waals heterostructures," *Nature*, vol. 499, no. 7459, pp. 419–25, 2013.
- [86] F. Pizzocchero *et al.*, "The hot pick-up technique for batch assembly of van der Waals heterostructures," *Nat. Commun.*, vol. 7, no. May, 2016.
- [87] T. K. Systems, "The IIT Foundation Series - Physics Class." [Online]. Available: <http://www.msnuclous.org/membership/html/jh/biological/microscopes/lesson2/microscopes2c.html>.
- [88] P. Blake *et al.*, "Making graphene visible," *Appl. Phys. Lett.*, vol. 91, no. 6, 2007.
- [89] A. C. Ferrari and D. M. Basko, "Raman spectroscopy as a versatile tool for studying the properties of graphene," *Nat. Nanotechnol.*, vol. 8, no. 4, pp. 235–246, 2013.
- [90] A. C. Ferrari *et al.*, "Raman spectrum of graphene and graphene layers," *Phys. Rev. Lett.*, vol. 97, no. 18, p. 187401, 2006.
- [91] L. M. Malard, M. A. Pimenta, G. Dresselhaus, and M. S. Dresselhaus, "Raman spectroscopy in graphene," *Phys. Rep.*, vol. 473, no. 5–6, pp. 51–87, 2009.
- [92] C. Casiraghi, S. Pisana, K. S. Novoselov, A. K. Geim, and A. C. Ferrari, "Raman fingerprint of charged impurities in graphene," *Appl. Phys. Lett.*, vol. 91, no. 23, pp. 1–4, 2007.
- [93] I. Childres, L. A. Jauregui, J. Tian, and Y. P. Chen, "Effect of oxygen plasma etching on graphene studied using Raman spectroscopy and electronic transport measurements," *New J. Phys.*, vol. 13, 2011.
- [94] A. Eckmann *et al.*, "Probing the nature of defects in graphene by Raman spectroscopy," *Nano Lett.*, vol. 12, no. 8, pp. 3925–3930, 2012.
- [95] A. C. Ferrari, "Raman spectroscopy of graphene and graphite: Disorder, electron-phonon coupling, doping and nonadiabatic effects," *Solid State Commun.*, vol. 143,

- no. 1–2, pp. 47–57, 2007.
- [96] J. E. Lee, G. Ahn, J. Shim, Y. S. Lee, and S. Ryu, “Optical separation of mechanical strain from charge doping in graphene,” *Nat. Commun.*, vol. 3, no. May, p. 1024, 2012.
- [97] M. Kalbáč *et al.*, “Evaluating arbitrary strain configurations and doping in graphene with Raman spectroscopy,” *2D Mater.*, vol. 5, no. 1, p. 015016, 2017.
- [98] F. Forster *et al.*, “Dielectric screening of the Kohn anomaly of graphene on hexagonal boron nitride,” *Phys. Rev. B - Condens. Matter Mater. Phys.*, vol. 88, no. 8, pp. 1–7, 2013.
- [99] G. Giridhar, R. R. K. N. Manepalli, and G. Apparao, *Confocal Raman Spectroscopy*, vol. 2. Elsevier Inc., 2017.
- [100] G. Binnig, C. F. Quate, and C. Gerber, “Atomic Force Microscope,” *Phys. Rev. Lett.*, vol. 56, no. 9, 1986.
- [101] B. Cappella and G. Dietler, “Force-distance curves by atomic force microscopy,” *Surf. Sci. Rep.*, vol. 34, no. 1–3, pp. 1–3, 1999.
- [102] A. M. Goossens, V. E. Calado, A. Barreiro, K. Watanabe, T. Taniguchi, and L. M. K. Vandersypen, “Mechanical cleaning of graphene,” *Appl. Phys. Lett.*, vol. 100, no. 7, pp. 1–4, 2012.
- [103] M. R. Rosenberger, H. J. Chuang, K. M. McCreary, A. T. Hanbicki, S. V. Sivaram, and B. T. Jonker, “Nano-“Squeegee” for the Creation of Clean 2D Material Interfaces,” *ACS Appl. Mater. Interfaces*, 2018.
- [104] C. H. Lui, L. Liu, K. F. Mak, G. W. Flynn, and T. F. Heinz, “Ultraflat graphene,” *Nature*, vol. 462, no. 7271, pp. 339–341, 2009.
- [105] L. Gammelgaard *et al.*, “Graphene transport properties upon exposure to PMMA processing and heat treatments,” *2D Mater.*, vol. 1, no. 3, 2014.
- [106] R. Fujii, *Conductive Atomic Force Microscopy*. 2018.
- [107] G. Fisichella *et al.*, “Micro- and nanoscale electrical characterization of large-area graphene transferred to functional substrates,” *Beilstein J. Nanotechnol.*, vol. 4, no. 1, pp. 234–242, 2013.
- [108] J. A. Kellar, J. M. P. Alaboson, Q. H. Wang, and M. C. Hersam, “Identifying and characterizing epitaxial graphene domains on partially graphitized SiC(0001) surfaces using scanning probe microscopy,” *Appl. Phys. Lett.*, vol. 96, no. 14, pp. 2008–2011, 2010.
- [109] M. Nonnenmacher, M. P. O’Boyle, and H. K. Wickramasinghe, “Kelvin probe force microscopy,” *Appl. Phys. Lett.*, vol. 58, no. 25, pp. 2921–2923, 1991.
- [110] V. Panchal, R. Pearce, R. Yakimova, A. Tzalenchuk, and O. Kazakova, “Standardization of surface potential measurements of graphene domains,” *Sci.*

- Rep.*, vol. 3, no. 2, pp. 1–8, 2013.
- [111] O. Ochedowski *et al.*, “Effect of contaminations and surface preparation on the work function of single layer MoS₂,” *Beilstein J. Nanotechnol.*, vol. 5, no. 1, pp. 291–297, 2014.
- [112] M. Altvater *et al.*, “Electrostatic imaging of encapsulated graphene,” *2D Mater.*, no. Xxxx, 2019.
- [113] W. Melitz, J. Shen, A. C. Kummel, and S. Lee, “Kelvin probe force microscopy and its application,” *Surf. Sci. Rep.*, vol. 66, no. 1, pp. 1–27, 2011.
- [114] S. S. Datta, D. R. Strachan, E. J. Mele, and A. T. C. Johnson, “Surface Potentials and Layer Charge Distributions in Few-Layer Graphene Films arXiv : 0807 . 1650v1 [cond-mat . mtrl-sci] 10 Jul 2008,” 2008.
- [115] H. M. Chunzeng Li, Stephen Minne, Yan Hu, Ji Ma, Jianli He and T. M. Vinson Kelly, Natalia Erina, Senli Guo, “PeakForce Kelvin Probe Force Microscopy,” *Bruker*, pp. 1–14, 2007.
- [116] B. J. Robinson, C. E. Giusca, Y. T. Gonzalez, N. DKay, O. Kazakova, and O. V. Kolosov, “Structural, optical and electrostatic properties of single and fewlayers MoS₂: Effect of substrate,” *2D Mater.*, vol. 2, no. 1, 2015.
- [117] M. J. Shearer, M. Y. Li, L. J. Li, S. Jin, and R. J. Hamers, “Nanoscale Surface Photovoltage Mapping of 2D Materials and Heterostructures by Illuminated Kelvin Probe Force Microscopy,” *J. Phys. Chem. C*, vol. 122, no. 25, pp. 13564–13571, 2018.
- [118] Q. H. Wang *et al.*, “Understanding and controlling the substrate effect on graphene electron-transfer chemistry via reactivity imprint lithography,” *Nat. Chem.*, vol. 4, no. 9, pp. 724–732, 2012.
- [119] R. R. Dammel, “Effect of disorder on transport in graphene,” in *Physical Review Letters*, vol. 97, no. 23, p. 216.
- [120] R. R. Dammel, “Theory of charged impurity scattering in two-dimensional graphene,” in *Solid State Communications*, vol. 149, no. 27–28, Elsevier Ltd, p. 216.
- [121] R. R. Dammel, “Charged Impurity Scattering in Graphene Nanostructures,” in *Nature Physics*, vol. 4, no. 5, p. 216.
- [122] W. G. Cullen *et al.*, “High-fidelity conformation of graphene to SiO₂ topographic features,” *Phys. Rev. Lett.*, vol. 105, no. 21, pp. 1–4, 2010.
- [123] R. R. Dammel, “Chapter 5. Step-by-step View of the Lithographic Process,” p. 216.
- [124] K. S. Novoselov *et al.*, “Two-dimensional atomic crystals,” *Proc. Natl. Acad. Sci. U. S. A.*, vol. 102, no. 30, pp. 10451–3, 2005.
- [125] G. A. Luinstra and E. Borchardt, “Material properties of poly(propylene carbonates),” *Adv. Polym. Sci.*, 2012.
- [126] R. Frisenda *et al.*, “Recent progress in the assembly of nanodevices and van der

- Waals heterostructures by deterministic placement of 2D materials," *Chem. Soc. Rev.*, vol. 47, no. 1, pp. 53–68, 2018.
- [127] S. J. Haigh *et al.*, "Cross-sectional imaging of individual layers and buried interfaces of graphene-based heterostructures and superlattices," *Nat. Mater.*, vol. 11, no. 9, pp. 764–7, 2012.
- [128] C. Susskind, "Introduction to electron beam technology," *Proc. IEEE*, vol. 51, no. 4, pp. 648–648, 2008.
- [129] P. Simonet, D. Bischoff, A. Moser, T. Ihn, and K. Ensslin, "Graphene nanoribbons: Relevance of etching process," *J. Appl. Phys.*, vol. 117, no. 18, pp. 15–20, 2015.
- [130] Sascha Sadewasser; Thilo Glatzel, *Kelvin Probe Force Microscopy Measuring and Compensating Electrostatic Forces*. Springer Series in Surface Sciences, 2012.
- [131] G. Cohen *et al.*, "Reconstruction of surface potential from Kelvin probe force microscopy images," *Nanotechnology*, vol. 24, no. 29, 2013.
- [132] U. Zerweck, C. Loppacher, T. Otto, S. Grafström, and L. M. Eng, "Accuracy and resolution limits of Kelvin probe force microscopy," *Phys. Rev. B - Condens. Matter Mater. Phys.*, vol. 71, no. 12, pp. 1–9, 2005.
- [133] H. O. Jacobs, P. Leuchtman, O. J. Homan, and A. Stemmer, "Resolution and contrast in Kelvin probe force microscopy," *J. Appl. Phys.*, vol. 84, no. 3, pp. 1168–1173, 1998.
- [134] E. J. Fuller, D. Pan, B. L. Corso, O. Tolga Gul, J. R. Gomez, and P. G. Collins, "Quantitative Kelvin probe force microscopy of current-carrying devices," *Appl. Phys. Lett.*, vol. 102, no. 8, 2013.
- [135] F. Robin, H. Jacobs, O. Homan, A. Stemmer, and W. Bächtold, "Investigation of the cleaved surface of a p-i-n laser using Kelvin probe force microscopy and two-dimensional physical simulations," *Appl. Phys. Lett.*, vol. 76, no. 20, pp. 2907–2909, 2000.
- [136] G. Elias, T. Glatzel, E. Meyer, A. Schwarzman, A. Boag, and Y. Rosenwaks, "The role of the cantilever in Kelvin probe force: Microscopy measurements," *Beilstein J. Nanotechnol.*, vol. 2, no. 1, pp. 252–260, 2011.
- [137] T. MacHleidt, E. Sparrer, D. Kapusi, and K. H. Franke, "Deconvolution of Kelvin probe force microscopy measurements - Methodology and application," *Meas. Sci. Technol.*, vol. 20, no. 8, 2009.
- [138] A. Gil, J. Colchero, J. Gómez-Herrero, and A. M. Baró, "Electrostatic force gradient signal: Resolution enhancement in electrostatic force microscopy and improved Kelvin probe microscopy," *Nanotechnology*, vol. 14, no. 2, pp. 332–340, 2003.
- [139] D. Ziegler *et al.*, "Variations in the work function of doped single- and few-layer graphene assessed by Kelvin probe force microscopy and density functional theory," *Phys. Rev. B - Condens. Matter Mater. Phys.*, vol. 83, no. 23, pp. 1–7, 2011.

- [140] T. Latychevskaia, F. Wicki, C. Escher, and H. W. Fink, "Imaging the potential distribution of individual charged impurities on graphene by low-energy electron holography," *Ultramicroscopy*, vol. 182, pp. 276–282, 2017.
- [141] A. Di Bartolomeo *et al.*, "Comparison of trapped charges and hysteresis behavior in hBN encapsulated single MoS₂ flake based field effect transistors on SiO₂ and hBN substrates," *Nanotechnology*, vol. 28, no. 28, p. 335202, 2018.
- [142] R. E. Thomas and G. A. Haas, "Diffusion measurements in thin films utilizing work function changes: Cr into Au," *J. Appl. Phys.*, vol. 43, no. 12, pp. 4900–4907, 1972.
- [143] C. A. Chavarin, A. A. Sagade, D. Neumaier, G. Bacher, and W. Mertin, "On the origin of contact resistances in graphene devices fabricated by optical lithography," *Appl. Phys. A Mater. Sci. Process.*, vol. 122, no. 2, pp. 1–5, 2016.
- [144] E. J. H. Lee, K. Balasubramanian, R. T. Weitz, M. Burghard, and K. Kern, "Contact and edge effects in graphene devices," *Nat. Nanotechnol.*, vol. 3, no. 8, pp. 486–490, 2008.
- [145] V. Panchal, A. Lartsev, A. Manzin, R. Yakimova, A. Tzalenchuk, and O. Kazakova, "Visualisation of edge effects in side-gated graphene nanodevices," *Sci. Rep.*, vol. 4, no. 4, 2014.
- [146] J. R. Williams, L. DiCarlo, and C. M. Marcus, "Quantum hall effect in a gate-controlled p-n junction of graphene," *Science (80-.)*, vol. 317, no. 5838, pp. 638–641, 2007.
- [147] L. Lin, L. Liao, J. Yin, H. Peng, and Z. Liu, "Building graphene p-n junctions for next-generation photodetection," *Nano Today*, vol. 10, no. 6, pp. 701–716, 2015.
- [148] X. Feng *et al.*, "All carbon materials pn diode," *Nat. Commun.*, vol. 9, no. 1, pp. 1–7, 2018.
- [149] G. Wang *et al.*, "Seamless lateral graphene p–n junctions formed by selective in situ doping for high-performance photodetectors," *Nat. Commun.*, vol. 9, no. 1, pp. 1–9, 2018.
- [150] F. A. Chaves, D. Jiménez, J. E. Santos, P. Bøggild, and J. M. Caridad, "Electrostatics of metal-graphene interfaces: Sharp p–n junctions for electron-optical applications," *Nanoscale*, vol. 11, no. 21, pp. 10273–10281, 2019.
- [151] F. Giannazzo, G. Greco, F. Roccaforte, and S. Sonde, "Vertical Transistors Based on 2D Materials: Status and Prospects," *Crystals*, vol. 8, no. 2, p. 70, 2018.
- [152] O. Leenaerts, B. Partoens, and F. M. Peeters, "Adsorption of H₂O, NH₃, CO, NO₂, and NO on graphene: A first-principles study," *Phys. Rev. B*, vol. 77, no. 12, p. 125416, 2008.
- [153] Y. Miyahara and P. Grutter, "Force-gradient sensitive Kelvin probe force microscopy by dissipative electrostatic force modulation," *Appl. Phys. Lett.*, vol. 110, no. 16, 2017.

- [154] X. Wang and H. Dai, "Etching and narrowing of graphene from the edges," *Nat. Chem.*, vol. 2, no. 8, pp. 661–665, 2010.
- [155] S. Pisana *et al.*, "Breakdown of the adiabatic Born-Oppenheimer approximation in graphene," *Nat. Mater.*, vol. 6, no. 3, pp. 198–201, 2007.
- [156] M. Lazzeri, S. Piscanec, F. Mauri, A. C. Ferrari, and J. Robertson, "Phonon linewidths and electron-phonon coupling in graphite and nanotubes," *Phys. Rev. B - Condens. Matter Mater. Phys.*, vol. 73, no. 15, pp. 1–6, 2006.
- [157] M. B. B. S. Larsen, D. M. A. Mackenzie, J. M. Caridad, P. Bøggild, and T. J. Booth, "Transfer induced compressive strain in graphene: Evidence from Raman spectroscopic mapping," *Microelectron. Eng.*, vol. 121, pp. 113–117, 2014.